1984ApJS...55..211H

THE ASTROPHYSICAL JOURNAL SUPPLEMENT SERIES, 55:211–246, 1984 June
© 1984. The American Astronomical Society. All rights reserved. Printed in U.S.A.

A NUMERICAL STUDY OF NONSPHERICAL BLACK HOLE ACCRETION. II. FINITE DIFFERENCING AND CODE CALIBRATION

JOHN F. HAWLEY AND LARRY L. SMARR[1]
Astronomy Department, University of Illinois

AND

JAMES R. WILSON
Lawrence Livermore National Laboratory
Received 1983 June 20; accepted 1983 December 9

ABSTRACT

We describe in detail our two-dimensional, axisymmetric computer code for calculating fully relativistic ideal gas hydrodynamics around a Kerr black hole. This code is being used to study fully dynamic inviscid fluid accretion onto black holes, as well as the evolution and development of nonlinear instabilities in pressure-supported accretion disks. The numerical techniques are developed and discussed. A variety of alternate differencing schemes are compared on an analytic test bed. Some discussion is devoted to general issues in finite differencing. The working code is calibrated using analytically solvable accretion problems, including the radial accretion of dust and of fluid with pressure (Bondi accretion). Two-dimensional test problems include the spiraling infall of low angular momentum fluid, the formation of a pressure-supported torus, and the stable evolution of a torus.

Subject headings: black holes — hydrodynamics — relativity — stars: accretion

I. INTRODUCTION

Our previous paper (Hawley, Smarr, and Wilson 1984, hereafter Paper I) began the procedure of completely documenting the general relativistic hydrodynamics code that we have developed. Paper I described the differential equations to be studied and some of the goals of this work. A test bed of analytic solutions was developed to allow comparison of various finite difference schemes and code calibration. This paper represents the next step in documentation: development, analysis, and testing of the finite difference equations themselves. We include descriptions and tests involving both the finite difference scheme used at present and several comparable schemes. In addition to providing information about a particular hydrodynamics code, these results can serve as a useful reference for other researchers developing their own codes. By compiling both the analytic solutions for several test problems (Paper I) and the actual finite difference results for several schemes, future workers will be able to reproduce these tests and use this work for an immediate comparison.

This paper is divided into two main sections. In the first, the finite difference schemes and our specific accretion code are described. Several separate schemes have been tried; the relative suitability of each is discussed. In the second section the results of many of the code test problems are given, often for several schemes, facilitating the comparison between the different approaches. Emphasis will be placed upon tests involving the scheme we will be using.

The hydrodynamic calculations are performed in a fixed gravitational field; for accretion problems this field is represented by the Kerr metric $g^{\mu\nu}$ expressed in Boyer-Lindquist coordinates. The metric defines the lapse function $\alpha = (-g^{tt})^{-1/2}$, the shift vector $\beta^i = g^{ti}$, and the three-metric $\gamma^{ij} = g^{ij}$. The dynamic matter is described by the ideal fluid stress-energy tensor $T^{\mu\nu} = (\rho + \rho\varepsilon + P)U^\mu U^\nu + Pg^{\mu\nu}$, where ρ is the baryon density, P is the pressure, and ε the specific internal energy.

Before beginning our discussion we remind the reader of the equations of general relativistic hydrodynamics as they are applied in our code. First, there is the equation of baryon conservation:

$$\partial_t D + \frac{1}{\sqrt{\gamma}}\partial_i\left(\sqrt{\gamma}\, DV^i\right) = 0, \tag{1}$$

where $D = W\rho$, $V^i = U^i/U^t$, γ is determinant of the three-metric, and $W = (1 - V_iV^i)^{-1/2}$ is the redshift factor equal to $U^t\alpha$, where α is the lapse function. Momentum conservation is written

$$\partial_t S_j + \frac{1}{\sqrt{\gamma}}\partial_i\left(S_jV^i\sqrt{\gamma}\right) + \alpha\partial_j P + \frac{1}{2}\left(\partial_j g^{\mu\nu}\right)\frac{S_\mu S_\nu}{S^t} = 0, \tag{2}$$

where $S_\nu = \rho hWU_\nu$, with relativistic enthalpy $h = 1 + \varepsilon + P/\rho$. Finally, we write the equation of energy conservation:

$$\partial_t E + \frac{1}{\sqrt{\gamma}}\partial_i\left(\sqrt{\gamma}\, V^iE\right) + P\partial_t W + \frac{P}{\sqrt{\gamma}}\partial_i\left(\sqrt{\gamma}\, V^iW\right) = 0, \tag{3}$$

where $E = \rho\epsilon W$. In these equations $j = r, \theta, \phi$; $i = r, \theta$; and μ and $\nu = r, \theta, \phi, t$. The equation of state is that for an ideal gas, $P = \rho\epsilon(\Gamma - 1) = (E/W)(\Gamma - 1)$.

[1]Alfred P. Sloan Fellow.

© American Astronomical Society • Provided by the NASA Astrophysics Data System

1984ApJS...55..211H

II. FINITE DIFFERENCING

a) *General Aspects*

We begin by describing some general features used in this code before proceeding to the specifics of the differencing schemes. The code uses Eulerian hydrodynamics with a fixed grid; in earlier work (Wilson 1972) cylindrical (R, Z) coordinates were used. We switched to spherical coordinates because of certain problems associated with a cylindrical grid. First, because of the geometry of the Kerr metric, it is desirable to have a finer grid near the hole; this prevents the proper distance between radial grid points from becoming too large. In cylindrical coordinates this is accomplished by increasing the grid density for small values of R or Z. The drawback is that this leads to long, thin zones at large radius along the axis or the equator and corresponding numerical errors. Second, the hole itself is spherical, although one might argue that the equations of an accretion disk may be best expressed in cylindrical coordinates. Given these considerations we have selected spherical coordinates (r, θ) for this new code. Angular zones can be specified at regular intervals or with increasing density in a desired region, e.g., near the equator for a disk model. Radial zones are closely spaced near the hole, then spaced further and further apart at large r; in this way the zones remain roughly square at all radii. We note that our code is written to be nearly covariant. The chosen coordinates enter the hydrodynamic equations through the metric terms. By changing metric terms and a few other details such as the way the grid is set up and spaced, it is possible to switch from one coordinate system to another without altering the hydrodynamic difference equations. As an example, the shock tube tests were run on a rectangular, flat space grid by substituting the Minkowski for the Kerr metric and changing the grid spacing.

The chosen grid divides the computational region into finite difference zones. The variables of the equations are centered at different locations in a given zone. Scalars (and all even-rank tensors) are located at the center of the zone; vectors (and all odd-rank tensors) are located at zone boundaries. Since vectors are formed out of differences of scalars (derivatives), it is natural to place a vector in a centered location between the differenced scalars. Such a finite difference has a formal second-order accuracy as opposed to the first-order accuracy of a forward or backward difference. The "staggered grid" is also well suited for differencing of the transport equations (discussed below). An example of the grid and variable locations is given in Figure 1.

Note that we give the vectors and the scalars the same index j (as opposed to using $j+1/2$ notation). This does not indicate the same spatial location. There are in fact two grids indicated by either an a for zone boundaries $(ra, \theta a)$, or a b for zone centers $(rb, \theta b)$ (see Fig. 1). This should not cause confusion so long as one keeps the variable locations in mind and recalls that the zone boundary j or k is located at a smaller radius or angle than zone center j or k $(ra_j < rb_j$, $\theta a_k < \theta b_k)$. Associated with each grid location is a spatial difference, e.g., $\Delta rb_j = rb_{j+1} - rb_j$.

The next consideration arises from the fact that we have chosen to use time-explicit differencing: the time step is

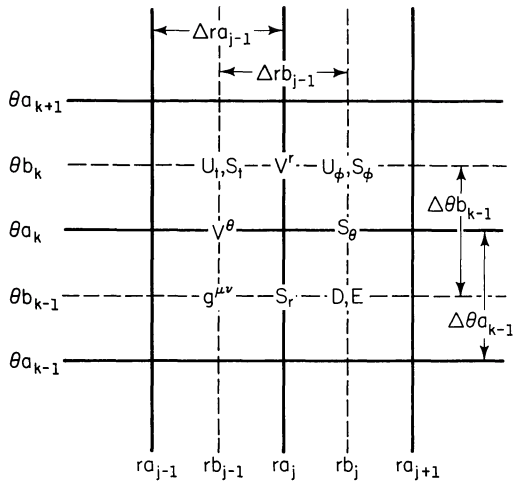


FIG. 1.—The finite difference grid used with our code. Zone centers occur on the (b) grid, i.e. $(rb_j, \theta b_k)$, and zone boundaries are on the (a) grid. Sample variable locations are shown.

limited by the Courant-Friedrichs-Lewy condition (hereafter CFL; see Courant, Friedrichs, and Lewy 1967). This condition is the very fundamental statement that a scheme cannot be convergent if the domain of dependence of a point in the finite difference equation does not include all the points in the domain of dependence of the differential equation. Given a point x_j at time level n and a spatial separation Δx, we must choose a time step Δt sufficiently small so that when the next time level $(n+1)$ is laid down, the points which are determined in part by variables located at x_j (e.g., $x_j + \Delta x$, x_j, and $x_j - \Delta x$ at time $n+1$) must extend over a spacelike slice which includes all space in the forward-facing sonic cone from point x_j (see Fig. 2).

The CFL condition is a necessary condition for convergence and stability in an explicit finite difference scheme; it is not sufficient, particularly in multidimensional systems with variable sound speeds. The CFL condition for a Newtonian system can be expressed in the form

$$\Delta t \leq \frac{\Delta x}{(|V| + V_s)} = \frac{\Delta x}{V_c}, \tag{4}$$

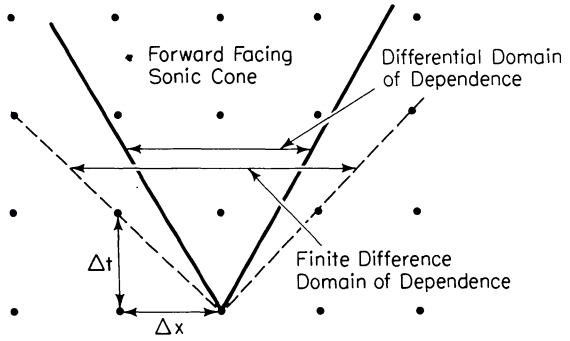


FIG. 2.—CFL condition is satisfied by choosing a grid size and time step so that the finite difference domain of dependence includes the entire differential domain of dependence, here given by the forward-facing sonic cone.

© American Astronomical Society • Provided by the NASA Astrophysics Data System

1984ApJS...55..211H

where V_s is the local sound speed and we define V_c as the CFL limit speed.

A similar condition could be used for the general relativistic flows in our code; replace the Newtonian with the relativistic sound speed and use relativistic addition of velocities to obtain the CFL velocity V_c. At each point in the corotating frame ($U_\phi = 0$) trace out the forward characteristics of the fluid equations and choose the most restrictive case to limit the time step. This is a nontrivial task in general, since the act of tracing out the characteristics while taking into account the time and space variations in sound speed amounts to solving the fluid equations by the method of characteristics. Even if simplifications are made, such as ignoring local changes in sound speed, it is necessary to reevaluate the time step at frequent time intervals. We choose instead to set the CFL velocity to the speed of light c. For a given metric, trace out light cones at all points and find the largest Δt permitted by applying the condition

$$\Delta t^2 \leq -\left(g_{\theta\theta}\Delta\theta^2 + g_{rr}\Delta r^2\right)/g_{tt} \tag{5}$$

to the smallest Δr and $\Delta\theta$ in the grid. In general, some multiple or fraction of the maximum permissible time step is used; a smaller Δt reduces numerical diffusion and is desirable so long as the increased running time does not become prohibitive. The requirements of a specific problem and the computer limitations decide the issue.

Other "problem specific" issues are the boundary conditions; a few general rules hold. The angular boundary conditions are taken care of by the requirement of axisymmetry for calculations involving the complete half plane from 0 to π. If desired, equatorial reflection symmetry may be used to calculate the quarter plane from 0 to $\pi/2$. In the radial dimension there is a physical inner boundary (the horizon) and an artificial outer boundary. The horizon is located just inside zone boundary $j = 2$, and the outer boundary is located at $j = JM$. The horizon may appear to be a problem since several variables and the coordinates themselves become singular there; in fact, the Kerr geometry actually simplifies matters. While the proper velocity approaches c at the horizon, the coordinate velocity V^i approaches zero as a result of time dilation (e.g., see Paper I, Fig. 6). The flow in the near-hole region is usually inward, further impeding the outward propagation of any noise introduced by a finite difference inner boundary condition. In practice, the outflow of fluid density, energy, or momentum from the innermost zone is explicitly prohibited by setting the flux through boundary $j = 3$ equal to zero if the velocity there is outwardly directed. For inwardly directed flow, several methods have been used to update the value at the innermost zone. One such method was to assume inward geodesic motion to obtain a velocity and calculate the flux through the $j = 2$ boundary and into the hole; alternately, we have simply allowed fluid to pile up in the zone nearest the horizon by setting the flux to zero at the $j = 2$ boundary. We have performed a variety of tests of the inner boundary condition using the problems described later in this paper and have found that the influence of the inner boundary rarely extends beyond the nearest neighbor zone and that the differences between boundary conditions are not significant as long as the information outflow from the innermost zone is explicitly held to a minimum.

The outer boundary condition affects and often determines the flow in the entire grid. Each new problem requires its own outer boundary condition, and the results obtained must be evaluated with this condition in mind. Some boundary conditions that have been used include: (1) fixed inflow of fluid with a specific density, energy, and momentum; (2) no inflow with outflow permitted; and (3) inflow and outflow permitted and determined by the fluid flux through the inward neighboring zone. Each type of boundary condition is set up by specifying the flux through zone boundary $j = JM$. Further discussion of boundary conditions will be reserved for the sections dealing with specific models and results.

Given a grid, time step, and boundary conditions, the partial differential equations (PDEs) are studied by the repeated evaluation of the system of finite difference equations (FDEs) which represent the PDEs. In our explicit, Eulerian scheme this involves the use of "operator splitting" (Wilson 1978) in which the FDEs are broken into parts and each part is evaluated separately in turn. For example, given a system

$$\partial_t A = L(A), \tag{6}$$

where L is an operator ($L = L_1 + L_2 + L_3 + \cdots$). We rewrite equation (6) as

$$\begin{aligned} A^1 &= A^0 + \Delta t L_1(A^0), \\ A^2 &= A^1 + \Delta t L_2(A^1), \\ A^3 &= \ldots . \end{aligned} \tag{7}$$

In each step we have expressed the time derivative as $(A^{n+1} - A^n)/\Delta t$ and then operated in sequence with the separate parts of L using the latest value of A for each update. In particular, we divide the equations into the following sequence of components: transport terms, accelerations due to pressure and gravity, evaluation of the velocity field, change in energy due to $P\,dV$ work, and viscous heating from compression (shock dissipation). Other evaluation sequences have been tried without significant change, although one could imagine situations in which this might not be so. For example, it is possible that by consistently doing differencing in one direction first and then the other, some nonphysical drift could occur; e.g., a spherical flow might not remain spherical. The use of an operator-split explicit scheme introduces a certain degree of asymmetry into the calculation. In the current version of our code the calculation of a certain component, i.e., a transport term, proceeds first in the radial direction from small to large radius, then steps through in the angular direction from 0 to π (or $\pi/2$ for problems in which equatorial reflection symmetry is used). If desired, it is possible to alternate sweep directions and even to average the results of two alternate sweeps. Some analysis of the two-dimensional split is performed by Strang (1968). Numerical experiments provide the best check. The actual differencing of these various terms is discussed below and divided into two sections: the "Lagrangian" terms and the "transport" terms, which arise solely in the context of Eulerian hydrodynamics.

© American Astronomical Society • Provided by the NASA Astrophysics Data System

1984ApJS...55..211H

b) Differencing of Lagrangian Terms

We begin by discussing the differencing of the most straightforward of the terms in the equations, the Lagrangian terms, so-called because they deal with the comoving acceleration and heating of a given element of fluid. The transport of that fluid element through the grid is what makes a code Eulerian, and these terms will be dealt with below.

Consider first the acceleration due to pressure gradients and three-metric gradient (gravitational and centrifugal acceleration). Written in their operator-split form these terms are

$$\partial_t S_j = -\alpha \partial_j P - \tfrac{1}{2}\left(\partial_j g^{\mu\nu}\right) S_\mu S_\nu / S^t. \tag{8}$$

The pressure gradient term is quite simple. Momentum S_j is located (Fig. 1) at zone boundaries ($j = r, \theta$; S_ϕ is at zone centers), while pressure is at the center. Thus, for the pressure gradient term write

$$S_{r_j}^{n+1} = S_{r_j}^n - \Delta t \bar{\alpha}_j (\Gamma - 1)\left[(E/W)_j - (E/W)_{j-1}\right]^n / \Delta r b_j. \tag{9}$$

A similar equation is written for S_θ:

$$S_{\theta_k}^{n+1} = S_{\theta_k}^n - \Delta t \bar{\alpha}_k (\Gamma - 1)\left[(E/W)_k - (E/W)_{k-1}\right]^n / \Delta \theta b_k. \tag{10}$$

These equations are exemplary of the notation to be used in describing the FDEs. The superscript n refers to time level, and the subscript j refers to the radial location. The term $\bar{\alpha}_j$ means a spatial average of α centered at ra_j; e.g., $\bar{\alpha}_j = 1/2(\alpha_j + \alpha_{j-1})$. The subscript k refers to the θ direction.

Note that the lapse function must be averaged to obtain a value at a boundary position. Since the lapse function is a fixed metric function, it could be explicitly calculated (along with the other metric terms $g^{\mu\nu}$) and stored at all points on the grid; the limitation is the computer core space. In general, however, the use of a staggered grid involves averaging of field variables. Often it is adequate to use an arithmetic average; in some cases a more sophisticated approach is required because of a rapid change in the gradient of the averaged function. A geometric average may prove useful; sometimes it is possible to divide a function by the singular portion and average the result. Multiplying by the singular factor in the centered location then completes the averaging. Such a procedure is particularly useful near the horizon where certain terms become singular as a result of the geometry.

The calculation of the metric acceleration terms is also rather straightforward and handled in a similar fashion. Given S_r, S_θ, and S_ϕ, we first obtain S_t and S^t through the normalization of the four-momentum using the equation

$$g^{\mu\nu} S_\mu S_\nu + (D + \Gamma E)^2 = 0. \tag{11}$$

The metric terms are then differenced in the same manner as the pressure, and the complete difference equation is assembled for both S_r and S_θ. Note that in the S_r equation both S_θ and S_ϕ must be properly centered through averaging, while for the S_θ equation, S_r and S_ϕ must be averaged. A typical term is the update of S_r:

$$S_{r_j}^{n+1} = S_{r_j}^n - \frac{\Delta t}{\Delta r b_{j-1}} \frac{1}{\bar{S}_j^t}\Big[S_{r_j}^2 \left(g_j^{rr} - g_{j-1}^{rr}\right) + \bar{S}_{\theta_j}^2 \left(g_j^{\theta\theta} - g_{j-1}^{\theta\theta}\right) + \bar{S}_{\phi_j}^2 \left(g_j^{\phi\phi} - g_{j-1}^{\phi\phi}\right) + \bar{S}_{t_j}^2 \left(g_j^{tt} - g_{j-1}^{tt}\right) + 2\bar{S}_{\phi_j}\bar{S}_{t_j}\left(g_j^{t\phi} - g_{j-1}^{t\phi}\right)\Big]. \tag{12}$$

Having completed the Lagrangian acceleration terms, we now calculate the Lagrangian heating terms. Consider the equation of $P\,dV$ work:

$$\partial_t E = -P\partial_t W - \frac{P}{\sqrt{\gamma}} \partial_i \left(W\sqrt{\gamma}\, V^i\right). \tag{13}$$

Inserting the equation of state, this becomes

$$\partial_t E = -(\Gamma - 1)\frac{E}{W}\partial_t W - (\Gamma - 1)\frac{E}{W\sqrt{\gamma}} \partial_i \left(W\sqrt{\gamma}\, V^i\right). \tag{14}$$

Note that energy is found on both sides of the equation; we can use this to our advantage to aid the time centering of these terms. The two portions of this equation are both differenced (separately) by writing them in the form

$$\frac{\partial_t E}{E} = -H, \tag{15}$$

where H will be either $[(\Gamma - 1)/(W\sqrt{\gamma})]\partial_i(\sqrt{\gamma}\, WV^i)$ or $[(\Gamma - 1)/W]\partial_t W$. The spatial H is differenced in the usual manner and centered at rb_j.

$$H = \frac{\Gamma - 1}{(\sqrt{\gamma}\, W)_j}\Big\{\Big[\left(\overline{W\sqrt{\gamma}}\right)_{j+1} V_{j+1}^r - \left(\overline{W\sqrt{\gamma}}\right)_j V_j^r\Big]\Big/\Delta r a_j + \Big[\left(\overline{W\sqrt{\gamma}}\right)_{k+1} V_{k+1}^\theta - \left(\overline{W\sqrt{\gamma}}\right)_k V_k^\theta\Big]\Big/\Delta\theta a_k\Big\}. \tag{16}$$

Next comes the time derivative of W. A time-explicit differencing scheme often has trouble with time derivatives of variables on the right-hand side of evolution equations—they are difficult to center properly in time, particularly since they are often functions of the variable on the left-hand side which is being evolved. Such a term can be properly handled only in a time-implicit formalism (see, e.g., Norman and Winkler 1983). However, we are able to get around this problem here by using the trick of bringing E over to the left and then integrating the equation. The second term in H is obtained with a time average and a difference of W using values of W before and after velocity renormalization:

$$H = \frac{\Gamma - 1}{\overline{W}^{n+1/2}}(W^{n+1} - W^n)/\Delta t. \tag{17}$$

© American Astronomical Society • Provided by the NASA Astrophysics Data System

1984ApJS...55..211H

Having calculated the appropriate H, the energy equation is integrated:

$$\int \frac{dE}{E} = \int -H\,dt; \qquad E(t+\Delta t) = E(t)\,e^{-H\Delta t} \quad (18)$$

The remaining Lagrangian term is the viscosity. In the stress energy tensor the artificial viscosity Q enters exactly like a bulk viscosity and consequently appears in the evolution equation wherever isotropic pressure does. The form of the viscosity is the same as that developed by May and White (1967) for relativistic hydrodynamics. In particular,

$$Q = K(D + \Gamma E)(\Delta V^i)^2 \qquad \text{for } \Delta V^i < 0,$$
$$= 0 \qquad \text{for } \Delta V^i > 0, \quad (19)$$

with K a constant and $\Delta V^i \equiv V^{i+1} - V^i$. Thus, Q is nonzero only in regions of local fluid compression. (The compressibility of a fluid is defined as $\theta \equiv \nabla^i V_i$). The viscosity term in the momentum evolution equation (eq. [2]) is updated in exactly the same fashion as the pressure gradient term (eqs. [9]–[10]) described above. A new scheme must be used for the energy equation since artificial viscosity Q is not solely a function of energy E. A variety of approaches has been tried with mixed results, and further discussion is postponed until the section below on relativistic shocks.

c) *Eulerian Transport Differencing*

i) *Control Volume Approach*

This section deals exclusively with the transport terms in the density, energy, and momentum evolution equations. The density equation will serve as the archetype for this discussion. Also, for simplicity we will limit the present discussion to a one-dimensional, flat space example. There will be little loss of generality; to return to the fully relativistic, two-dimensional case, simply reintroduce the geometry through inclusion of the metric term $\sqrt{\gamma}$ and perform the differencing in both dimensions through operator splitting. This simplicity is the advantage of this formulation of the fully relativistic hydrodynamics equations—one can directly apply numerical skills developed in studying Newtonian hydrodynamics.

Unlike Lagrangian terms which deal with changes occurring in a given element of fluid, transport terms involve changes in the state of the fluid at a specific volume in space. These changes are governed by the amount of density, energy, and momentum entering or leaving that volume per unit time. For a finite difference scheme, replace the differential equation

$$\partial_t D + \partial_x(DV) = 0 \quad (20)$$

by a properly zone-centered difference equation:

$$D_j^{n+1} = D_j^n - \frac{\Delta t}{\Delta x a_j}(\text{flux}_{j+1} - \text{flux}_j), \quad (21)$$

where $(\text{flux})_{j+1}$ represents the flux through the zone boundary at $j+1$, a flux determined by density and velocity (and geometry). Note that for two-dimensional hydrodynamics this process is repeated by differencing the flux in and out of a zone volume through the $k+1$ and k zone boundaries.

To avoid numerical difficulties in near-vacuum regions in the grid, a minimum value of density and energy is required at each point. These variables can therefore never become zero or negative. In practice this "floor" value is fixed at a level many orders of magnitude (e.g., 10) below the smallest significant value of density or energy. As such it has no effect on the dynamics of the physical problem being calculated, and yet its use prevents a number of fatal problems which can arise if, for example, the density becomes zero or the energy negative.

The manner in which one chooses a value for the flux terms determines the scheme and its accuracy. This is the "control volume" approach to the fluid transport equations in which zones are treated as bins filled with a quantity of physical fluid which is moved about by the velocity field. The control volume approach emphasizes the physics involved rather than relying upon a formal mathematical approximation which often does not retain the macroscopic physical basis from which the original fluid equations were derived. For example, our transport equation (eq. [21]) is globally conservative, a feature formal approximations often lack. A summation over all grid points demonstrates that the total mass in the grid remains constant except for what is introduced or removed at the boundaries. Global conservation, however, should not be confused with local conservation. That is, one can have several density profiles whose total summed mass is the same. For instance, all Eulerian numerical schemes entail a certain amount of numerical diffusion which causes gradients in a function to be smoothed out over time. Thus, a physical feature such as a contact discontinuity in density will not be maintained indefinitely. Other problems can arise from the artificial separation of energy and angular momentum from density. This can happen if there is a steep gradient in specific energy or angular momentum; the numerical errors in the separate transport equations do not balance. See Norman, Wilson, and Barton (1980) for an excellent discussion of this problem in the context of the two-dimensional collapse of a rotating protostar.

We can judge the magnitude of error in an explicit scheme by the degree to which it damps out features that are resolved in only a few grid points. In so analyzing the schemes discussed here we will eschew the use of detailed analysis, preferring instead to express things qualitatively in terms of the physical fluid. In this way it is hoped that the schemes will be more intuitively understandable. Those readers who would like additional details are referred to the cited literature. (See, e.g., Smarr 1978 for an introduction to issues and terminology in finite differencing; a complete textbook treatment of the subject can be found in Roache 1972.)

ii) *First-Order Upwind Transport*

Begin by considering the simplest of transport schemes, the first-order "upwind" or "donor cell" scheme. In this scheme a flux is obtained by first determining the direction of the velocity at the boundary of a zone. The flux is then set equal to that velocity times the density at the centered location

© American Astronomical Society • Provided by the NASA Astrophysics Data System

1984ApJS...55..211H

upstream or upwind from that boundary point. Specifically,

$$\text{flux}_j = (V_j)(D_{j-1}) \quad \text{for } V_j > 0,$$
$$= (V_j)(D_j) \quad \text{for } V_j < 0. \tag{22}$$

Consider the flux out of a zone across boundary j ($V_j > 0$). To obtain a flux, we implicitly define a continuous function $D_{j-1}(x)$ over the whole zone (see Fig. 3). In the upwind scheme this function is set equal to the centered finite difference function value D_{j-1}, and the density is assumed to have a constant value throughout the whole zone. In a time step Δt we move out of the zone the fluid volume $\Delta t(V_j)(D_{j-1/2})$. The advantage of the upwind scheme is that it is very stable and very simple. There is a cost for these features, however; consider the propagation of a steep density gradient through space and described by some unknown analytic function $d(x)$. If we replace this continuous function with a series of functions $D_{j-1}(x)$, it is clear that the calculated flux through a zone boundary will always exceed the analytic flux when fluid flows from a region of higher density to lower; when the slope has the opposite sign, the flux will always be too small (Fig. 3). This is true for all stable schemes which are "upwind weighted," and it is the physical reason for the aforementioned numerical diffusion. The situation is worse when a scheme behaves in the opposite manner and enhances a gradient; some zones will empty, while others grow without bound. Such a scheme is unstable.

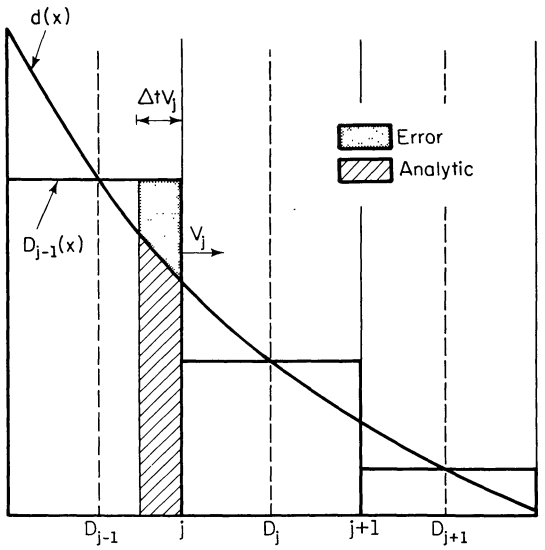


FIG. 3.—Finite-difference advection of the (unknown) analytic function $d(x)$ is accomplished by defining a distribution $D_j(x)$ in each bin (here a constant equal to the centered value D_j) and moving that distribution the distance $\Delta t V_j$. Error is the amount by which the scheme (here the "upwind" scheme) overestimates the volume of fluid advected out of the zone.

iii) *Wilson Transport*

If diffusion error results from the choice made for the transported density, is it possible to choose a better representation of the "actual" density distribution in the zone and hence reduce the numerical error? As a first attempt, consider the averaging scheme of Wilson (1978; hereafter the Wilson scheme). Obtain a linear density function centered on the zone boundary at j by taking an average of the densities at $j-1$ and j and extrapolating back into the upwind zone a distance $V_j\Delta t$ using the slope $(D_j - D_{j-1})/\Delta x b_j$, where $\Delta x b_j$ is defined in the same manner as $\Delta r b_j$ earlier. Specifically,

$$\text{flux}_j = V_j\left[\tfrac{1}{2}(D_{j-1} + D_j) - V_j\Delta t(D_j - D_{j-1})/\Delta x b_j\right]. \tag{23}$$

We expect that this formulation will yield a more accurate value of the flux from one zone to another, and this is often the case. However, this scheme can become unstable in certain situations; the physical reason is seen by considering flow in a region of steep gradient in D. For such a situation it is possible to imagine a case in which the volume of fluid transported out of a zone exceeds the total in the zone.

This evacuation of the zone can be avoided by mixing the upwind scheme with the new scheme in such a way that the upwind flux (F_1) is used in regions of steep density gradients and the extrapolated flux (F_2) is used in regions of mild gradient. The two fluxes are weighted accordingly with the weighting factor

$$\text{WT} = |D_j - D_{j-1}|/(D_j + D_{j-1}), \tag{24}$$

so that

$$\text{flux}_j = (\text{WT})F_1 + (1 - \text{WT})F_2. \tag{25}$$

This is the stable formulation of the Wilson scheme.

iv) *Monotonic Transport*

The development of the Wilson scheme involves using information available in neighboring zones to estimate the structure of the fluid distribution in a zone, allowing a higher order calculation of the flux into and out of that zone. Can we keep this feature and yet avoid the instability inherent in the Wilson scheme? The monotonic transport scheme ("mono scheme") of Bram van Leer (van Leer 1974, 1977*a*, *b*, 1979; Winkler 1981; Woodward 1983) is such a scheme. It is derived by considering the analytic transport equation

$$\partial_t d + a\partial_x d = 0. \tag{26}$$

For simplicity a constant transport velocity (a) has been assumed.

Given an initial value distribution $d(x)$, establish a finite difference grid, with D_j being zone averages of that initial value function. Rewrite the transport equation in integral form:

$$\int_{x_j}^{x_{j+1}} d(t,x)\,dx\Big|_{t_n}^{t_{n+1}} + \int_{t_n}^{t_{n+1}} ad(t,x)\,dt\Big|_{x_j}^{x_{j+1}} = 0. \tag{27}$$

This is equivalent to

$$\left(D_{j+1/2}^{n+1} - D_{j+1/2}^{n}\right)\Delta x + \left(\langle ad\rangle_{j+1} - \langle ad\rangle_j\right)\Delta t = 0, \tag{28}$$

where $\langle ad\rangle_j$ is a time average, which has the role of the flux

© American Astronomical Society • Provided by the NASA Astrophysics Data System

1984ApJS...55..211H

through boundary j. For clarity we will temporarily use the $j-1/2$ notation to refer to centered locations while deriving the mono scheme. Now concentrate on the calculation of that flux at j. By setting

$$\langle ad\rangle_j = aD_{j-1/2} \quad \text{for } a \geq 0, \tag{29}$$
$$= aD_{j+1/2} \quad \text{for } a < 0,$$

we reobtain the usual first-order upward differencing. Now we improve the accuracy of the scheme by improving the approximation used. Let

$$\langle ad\rangle_j = \tfrac{1}{2}a\left[D(t_{n+1}, x_j) + D(t_n, x_j)\right], \tag{30}$$

where the function $D(t_{n+1}, x)$ is approximately equal to $D(t_n, x)$ advected over a distance $a\Delta t = \sigma\Delta x$, where $\sigma = a\Delta t/\Delta x$ (assume $a > 0$). Thus, we can write

$$D(t_{n+1}, x_j) = D(t_n, x_j - \sigma\Delta x). \tag{31}$$

Hence, we are averaging the function $D(t, x)$ at $x = x_j$ at the beginning of the time step and at the end after advection. Now move back to the zone center location by replacing $D(t_n, x_j)$ with $D(t_n, x_{j-1/2} + 1/2\Delta x)$:

$$\langle ad\rangle_j = \tfrac{1}{2}a\left[D\left(t_n, x_{j-1/2} + \tfrac{1}{2}\Delta x - \sigma\Delta x\right) + D\left(t_n, x_{j-1/2} + \tfrac{1}{2}\Delta x\right)\right]. \tag{32}$$

Perform a Taylor expansion on $D(t_n, x_{j-1/2} + 1/2\Delta x - \sigma\Delta x)$ to obtain

$$D_{j-1/2} + \left(\tfrac{1}{2}\Delta x - \sigma\Delta x\right)\Delta_{j-1/2}D/\Delta x \tag{33}$$

using the gradient of D centered at $j-1/2$, $\Delta_{j-1/2}D/\Delta x$. Substituting these expansions into equation (32) yields

$$\begin{aligned}\langle ad\rangle_j &= \tfrac{1}{2}a\left[D_{j-1/2} + \left(\tfrac{1}{2}\Delta x - \sigma\Delta x\right)\Delta_{((j-1/2)/\Delta x)}D/\Delta x + D_{j-1/2} + \left(\tfrac{1}{2}\Delta x\right)\Delta_{((j-1/2)/\Delta x)}D/\Delta x\right] \\ &= \tfrac{1}{2}a\left[2D_{j-1/2} + (\Delta x - \sigma\Delta x)\Delta_{((j-1/2)/\Delta x)}D/\Delta x\right] \\ &= a\left[D_{j-1/2} + \tfrac{1}{2}(1-\sigma)\Delta_{j-1/2}D\right].\end{aligned} \tag{34}$$

The accuracy of this scheme can vary depending upon how we choose to define the gradient of $D(t, x)$, $\Delta_{j-1/2}D$. Several schemes using different definitions for $\Delta_{j-1/2}D$ are given by van Leer. In any case, the final difference equation is

$$D^{n+1}_{j+1/2} = D^n_{j+1/2} - \sigma\left[D_{j+1/2} - D_{j-1/2} + \tfrac{1}{2}(1-\sigma) \times \left(\Delta_{j+1/2}D - \Delta_{j-1/2}D\right)\right]. \tag{35}$$

The real advantage in this scheme is realized when the condition of monotonicity is used in the definition of $\Delta_{j-1/2}D$.

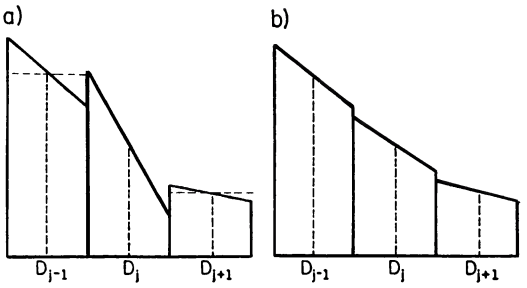


FIG. 4.—This figure shows three finite difference zones and the distributions $D(t, x)$ being used to represent the (unknown) analytic density distribution. In (a) the function $D(t, x)$ is nonmonotonic at the zone boundaries. In (b) monotonicity has been restored by altering the slope $\Delta D/\Delta x$.

We require that a distribution $D(t, x)$ which locally increases or decreases monotonically before advection must maintain that quality after advection. This means that the function $D(t, x)$ implicitly defined in zone $j-1/2$ by $D_{j-1/2}$ and $\Delta_{j-1/2}D$, i.e., the function advected by equation (33), must have values between those spanned by the neighboring functions $D(t, x)$ in zones $j-3/2$ and $j+1/2$. That is, the value of $D(t, x)$ at a zone boundary must fall between the zone average values $D_{j-3/2}$ and $D_{j-1/2}$. Figure 4 shows two distributions, one in which $D(t, x)$ is nonmonotonic at the zone boundary and one in which it is. From this figure it is clear that the choice made for the gradient $\Delta_{j-1/2}D$ makes all the difference in determining whether or not a distribution is monotonic or nonmonotonic. In the case of a local maximum or minimum in $D(t, x)$, the slope $\Delta_{j-1/2}D$ is set equal to zero through the zone in which the extremum occurs.

What is required is a definition of $\Delta_{j-1/2}D$ which insures that the requirements of monotonicity are met. van Leer finds that the following definition for the slope satisfies this criterion:

$$\Delta_{j-1/2}D = \frac{2(D_{j-1/2} - D_{j-3/2})(D_{j+1/2} - D_{j-1/2})}{D_{j+1/2} - D_{j-3/2}}$$
$$\text{if } (D_{j-1/2} - D_{j-3/2})(D_{j+1/2} - D_{j-1/2}) > 0; \tag{36}$$
$$\Delta_{j-1/2}D = 0 \text{ otherwise.}$$

Note that we set $\Delta_{j-1/2}D$ equal to zero if all three gradients do not have the same sign (nonmonotonic), i.e., we use the first-order upwind scheme in such situations. This geometric average of slopes insures the enforcement of the condition of monotonicity and prevents the evacuation of zones and the onset of unstable zone to zone oscillations.

v) *Other Schemes*

The use of a monotonicity condition is not restricted to the scheme derived above (which we nevertheless refer to as the mono scheme). Another such scheme is Barton's scheme (Barton 1981; Centrella and Wilson 1984). This scheme chooses between a variety of possible densities so as to locally select the "highest order" average which is consistent with the

© American Astronomical Society • Provided by the NASA Astrophysics Data System

1984ApJS...55..211H

requirement of monotonicity. Make the following definitions:

D_{-1} Density in upwind zone
D_{-2} Density two zones upwind
D_x $D_{-1}+1/2(\Delta ra/\Delta rb)(D_{-1}-D_{-2})$
D_{+1} Density in downwind zone
D_{avg} $1/2(D_{-1}+D_{+1})$

The transported density is

$$\overline{D} = \max\left[D_{-1}, \min(D_x, D_{\text{avg}})\right] \quad \text{if } D_{-1} < D_{+1},$$

$$= \min\left[D_{-1}, \max(D_x, D_{\text{avg}})\right] \quad \text{if } D_{-1} > D_{+1}. \quad (37)$$

Other definitions can also be used. For example, we have tried this scheme with D_x replaced by the mono formula (eqs. [34], [36]). In fact, any scheme could be inserted for D_x.

One final scheme is considered. This is Norman's consistent advection (CA) scheme (Norman, Wilson, and Barton 1980; Norman 1982). The relevant feature is a procedure better to insure local conservation of specific energy and angular momentum; this approach may be employed with any of the above schemes. Specifically, the transport of both momentum and energy is tied to the transport of density, thus assuring that the dissipation error introduced by the numerical scheme is applied equally to all the transported quantities. Density is transported in the usual way, and the density flux is regarded as the physical fluid volume transported in that time step. Fluxes of energy and momentum are formed by obtaining a specific energy and momentum flux (flux per baryon) and multiplying by the physical flux (flux of baryons). In this way the artificial change in specific energy and momentum due to finite difference errors is avoided.

vi) *Linear Stability Analysis*

Having outlined several possible transport schemes, we now turn to their analysis and comparison. While the proof of any numerical scheme lies in the numerical experiments, certain insights can be gained by doing some analytic work before plunging into a series of code tests. In particular, we can examine the degree to which numerical diffusion operates in a scheme, i.e., the amount of "implicit viscosity" which tends to homogenize an initial distribution on a grid. The way to approach this problem analytically is through the von Neumann analysis (Richtmyer and Morton 1967).

Consider a prototype one-dimensional hyperbolic equation:

$$\partial_t w + a\,\partial_x w = 0, \quad (38)$$

where a is the transport velocity. Represent this equation by a finite difference equation; e.g., consider the simple upwind scheme and let $a > 0$:

$$\frac{w_j^{n+1} - w_j^n}{\Delta t} + \frac{a}{\Delta x}\left(w_{j-1}^n - w_j^n\right). \quad (39)$$

Rewrite the function w_j^n as a finite Fourier series with Fourier wavelengths ranging from the length of the entire grid to $2\Delta x$ (the smallest resolvable):

$$w_j^n = \hat{W}^n \sum e^{ik(j\Delta x)} \quad (40)$$

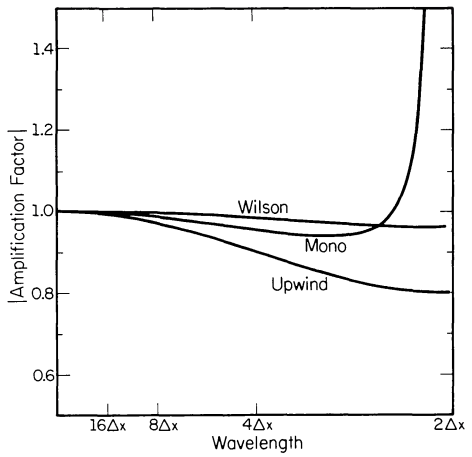


FIG. 5.—Amplification factors ($|\lambda|$) with $\sigma = 0.1$ for the upwind, Wilson and mono schemes.

and perform algebraic manipulations to obtain the form

$$\hat{W}^{n+1} = \lambda \hat{W}^n, \quad (41)$$

where λ is a complex function (the "amplification factor") depending upon $a\Delta t/\Delta x \equiv \sigma$ and $e^{nik\Delta x}$. When $|\lambda| < 1$, a given wavelength will not grow unbounded as time advances ("stability"). For example, the upwind scheme gives

$$|\lambda| = \{1 + 2\sigma(1-\sigma)[\cos(k\Delta x) - 1]\}^{1/2}. \quad (42)$$

This is plotted in Figure 5 for $\sigma = 0.1$. For the upwind scheme, $\lambda < 1$ for all $|\sigma| < 1$. Recall that $|\sigma| < 1$ is the CFL time step limitation. Note, however, that λ is considerably less than 1 for short wavelengths (as the wavelength approaches $2\Delta x$). This implies that such wavelengths will be damped out in the numerical solution, and, as a consequence, steep features which are resolved by short wavelengths will be rapidly smoothed out. Thus, the upwind scheme is a highly diffusive scheme.

Similar curves are drawn for the second-order part of the Wilson scheme and for the mono scheme (Fig. 5). It is seen that without the weighted mixture of the first-order scheme, $|\lambda| < 1$ for all wavelengths in the Wilson scheme, and $|\lambda|_{\text{Wilson}} > |\lambda|_{\text{upwind}}$. This is the desirable feature of the Wilson formula: it is less diffusive. However, the short wavelengths turn out to be unstable in regions of steep gradients. This is because the implicitly defined distribution $D(t, x)$ used in the second-order portion of the Wilson scheme can sometimes yield a value of transported density which exceeds the total density available in the zone, causing the evacuation of that zone and resulting instability (consider eq. [23] when $V_j > 0$ and $D_j \gg D_{j-1}$). Such evacuation of zones cannot occur when the first-order upwind scheme is used since the maximum mass which can be transported out of a zone is the total mass in the zone (i.e., D_{j-1} times the volume of the zone). The stable Wilson scheme (eq. [25]) mixes in a weighted amount of the upwind flux, thus maintaining stability. This will tend, however, to lower the net value of $|\lambda|$.

© American Astronomical Society • Provided by the NASA Astrophysics Data System

1984ApJS...55..211H

The mono scheme has a $|\lambda|$ factor which becomes large for short wavelengths, but this does not occur for any resolvable finite difference wavelength except $2\Delta x$; i.e., $|\lambda| < 1$ for wavelengths $3\Delta x$ or longer. The condition of monotonicity expressly prohibits such a wavelength, however, since it is manifestly nonmonotonic from zone to zone. Under these circumstances $\Delta_{j-1/2} D$ is set equal to zero, and the amplification factor $|\lambda|$ is the one associated with the upwind scheme. Thus, the $2\Delta x$ waves are damped, not magnified, and zone-to-zone oscillations are prevented. Through the use of the mono scheme we expect a very low level of diffusiveness. This analysis, while limited in scope, will help in interpreting the results of the numerical tests to follow.

d) *Velocity Renormalization*

For each time step a new velocity field must be calculated from the momentum terms S_j. This is done through normalization of the four-momentum and division by the total inertia term $(D + \Gamma E) = \rho h W$ (eq. [11]). The normalization occurs at zone centers, and the velocities are reaveraged to their proper zone boundary sites. This is done after the calculation of transport terms and before doing the Lagrangian terms.

Note that since the momentum terms are scattered about at various locations and must be averaged to the zone center where the inertia resides, we can in some circumstances be faced with a delicate problem. In particular, if the momentum and inertia are changing rapidly from zone to zone, unless one is careful, the four-velocity obtained by averaging the momentum to the zone center and dividing by the inertia may bear little relation to the actual four-velocity field because of averaging errors. To avoid this problem, it is sometimes better to obtain a velocity U_i first by dividing the momentum by an averaged inertia. These velocities are then averaged to the center where the normalization is performed. This assumes that the velocity field and inertia are less steep functions than the momentum; this is often the case. Geometric averages can also be used when needed. This problem remains as one more item to keep in mind when evolving a particular model.

III. CODE TESTING

a) *Nonrelativistic Riemann Shock Tubes*

The equations of general relativistic hydrodynamics have been laid out and studied analytically in Paper I. We have presented a number of prescriptions for solving those equations numerically; what remains is the synthesis of the analytic and the numerical in the realm of the code test.

There are three general physical effects to consider in shocks. These are the formation, the propagation, and the intersection of shock discontinuities. We may further subdivide these into cases in which the shock is present in initial discontinuous data ("impulsive" shocks) and those in which shocks arise from the gradual steepening of an initially smooth pressure profile ("acoustic" shocks). The characteristics describing the shock propagation may be straight or curved in spacetime, and they may or may not intersect. All of these physical effects provide good code tests and have been performed by Norman and Winkler (1983) and Woodward (1983).

As an example, we perform the quintessential test, the Riemann shock tube. We consider the shock tube used by Sod (1978) in his comparison of finite difference schemes. The problem is a nonintersecting impulsive shock involving only straight line propagation of the characteristics. This test case is described in Paper I, equations (42)–(47). The Sod shock tube is a Newtonian problem, but it is run using the complete coding including the relativistic terms; the Minkowski metric is used in place of Kerr. The finite difference domain is divided into 100 zones with $\Delta x = 1$. The peak fluid velocity in this problem is $V = 2.93 \times 10^{-3}$ ($c = 1$), and the maximum sound speed is $V_s = 3.74 \times 10^{-3}$; these two maxima do not occur in the same region of flow, but we will use them to obtain an upper limit on the Courant number. It is far too restrictive to use the speed of light c as the CFL limit speed (eq. [4]). Instead we choose a time step size $\Delta t = 25$ (i.e., light travels 25 zones in time Δt); this yields a Courant number

$$(V + V_s)\frac{\Delta t}{\Delta x} \lesssim 0.17 \tag{43}$$

small enough so that no time step instabilities are expected. The artificial viscosity constant K (see eq. [10]) is set equal to 2.0. The initial conditions of this problem are a gas with $\Gamma = 1.4$ at rest, with pressure, density, and specific internal energy $P_l = 1$, $\rho_l = 10^5$, and $\varepsilon_l = 2.5 \times 10^{-5}$ to the left of $x = 35.5$ and $P_r = 0.1$, $\rho_r = 0.125 \times 10^5$, $\varepsilon_r = 2 \times 10^{-5}$ to the right. This problem is described in detail in Paper I (see Fig. 3). Each of the transport schemes described above in § II is run on this problem to time $t = 5000$, at which point the results are compared graphically with the analytic values; numerical comparisons are made in Table 1.

TABLE 1

NUMERICAL RESULTS OF RIEMANN SHOCK TUBE TEST[a]

Scheme	V	ρ_l	ρ_r	ε_l	ε_r	P
Analytic	2.93×10^{-3}	0.426×10^5	0.266×10^5	1.78×10^{-5}	2.85×10^{-5}	0.303
Upwind[b] ...	2.92	...	...	1.79	2.80	0.299
Wilson.....	2.92	0.423	0.262	1.79	2.84	0.299
Barton.....	2.93	0.422	0.264	1.77	2.84	0.299
Mono.....	2.93	0.422	0.265	1.77	2.84	0.300
CA	2.93	0.420	0.264	1.77	2.84	0.299

[a] For various finite difference schemes using 100 zones. The values given are for the region between the rarefaction and the shock, both left and right of the contact discontinuity, and were obtained through averaging across the region of interest.

[b] No unambiguous value for ρ_l and ρ_r; ε_l and ε_r are the local minimum values.

© American Astronomical Society • Provided by the NASA Astrophysics Data System

1984ApJS...55..211H

In addition to the 100 zone test we also ran this same shock tube problem on a 200 zone grid, $\Delta x = 0.5$, $\Delta t = 12.5$. By comparing 100 and 200 zone runs for a given scheme we can immediately gauge the rate of convergence toward the analytic solution and obtain a better feel for the discretization errors involved in a given scheme.

Figure 6 shows the results for the simple first-order upwind or "donor cell" scheme. The extreme diffusiveness (implicit numerical viscosity) of this scheme is evident in each of the plots. The sharp corners in the analytic functions are gently rounded in the numerical results and spread over several zones. The density plot shows quite clearly the effect of this numerical diffusion. The upwind scheme has completely failed to resolve the contact discontinuity. The specific internal energy in the postshock region is too low by a significant amount, and the shock itself is not well resolved. The 200 zone run (Fig. 7) shows that these problems are only slightly alleviated by increasing the number of zones. Even with very fine zoning, the characteristic rounding out of function corners is apparent, and the contact discontinuity remains poorly resolved. The increase in zone number has not helped the specific internal energy; it remains too low, suggesting that this is not an error arising from discretization and that it will remain as $\Delta x \to 0$. It is important to distinguish between such sources of error.

The Wilson scheme is expected to be less diffusive, and, as Figure 8 shows, there is indeed less apparent diffusion in the numerical solution. A new phenomenon has appeared, however, the preshock and precontact oscillation. This "ringing" is a common feature in schemes of higher order. We are seeing the effect of the latent instability near regions of steep gradients; the spatial resolution of steep gradients requires short wavelength components in the solutions—wavelengths which have very little diffusion when computed by the higher order portion of the Wilson scheme, i.e., F_2 in equation (25). The mixing in of the damping first-order upwind scheme prevents these oscillations from growing without bound, but there is nothing to prevent their formation.

This prediscontinuity oscillation does not go away in finer zoned run (Fig. 9); the oscillations simply occur in shorter and shorter wavelengths. This ringing increases in amplitude as the solution approaches the discontinuity. The average zone-to-zone values obtained are more accurate than those obtained using first-order upwind alone; as expected from the von Neumann analysis, we find that the Wilson scheme is much less diffusive overall.

Barton's scheme attempts to obtain the increased accuracy of Wilson's scheme without allowing zone-to-zone oscillations to develop. This is achieved through the use of a local condition of monotonicity. Results for Barton's scheme are shown in Figure 10. We obtain good results without too much apparent numerical diffusion. The contact discontinuity has finally been unambiguously resolved.

The 200 zone run (Fig. 11) looks very good. The sharp corners in the analytic function are better resolved, as are the discontinuities. Here one feels that the use of a finer grid has purchased a better resolved solution, not better resolved errors.

Figure 12 shows the results for the mono scheme. These plots are quite similar to the Barton scheme results. The corners in the rarefaction wave functions are slightly sharper. The primary feature is the overshoot observed in the numerical function in regions where the analytic function goes from some nonzero slope to zero slope discontinuously in the first derivative (e.g., note the small peak at the end of the rarefaction wave on the velocity plot). Norman and Winkler (1983) have shown, using their highly developed implicit one-dimensional code, that such overshoots are in fact the solution to the finite difference equation using an artificial viscosity as $\Delta x \to 0$. Such an overshoot therefore is the signature of low-diffusive accuracy.

As for the Barton scheme, the 200 zone run looks excellent (Fig. 13). The main difference between the mono and the Barton results is the continued presence of the overshoot on the mono case.

We consider one last scheme in Figure 14. This is the mono scheme using Norman's "consistent advection" (CA) approach. The results of this calculation show that the CA scheme is slightly more diffusive than the mono scheme alone. This is likely due to the fact that pressure and density are the fundamental variables in the shock tube, not density and specific internal energy. Since the mono scheme evolves pressure and density, it is slightly better suited to this problem. The CA scheme should be employed when the significant dynamic variables are the specific internal energy or the specific angular momentum and sharply different gradients are expected in the separate density, energy, and total angular momentum functions. The use of the CA scheme will help insure local conservation of specific momentum and energy, yielding a more accurate dynamical evolution (Norman, Wilson, and Barton 1980). The 200 zone run (Fig. 15) for the CA scheme very closely resembles the 200 zone mono result.

An important lesson in Eulerian hydrodynamics is illustrated by these runs. The different schemes tested here were obtained through *minor code changes in the transport terms*; the differences in numerical results are *dramatic*. This points out that algorithm development is as important as increasing hardware computer speed or memory size. It also shows why code tests against analytic solutions are necessary for code calibration. A run using the mono scheme will obtain a better solution than the upwind scheme even if the number of zones in the upwind problem is increased several times. Since the cost of a one-dimensional run increases by a factor of 4 for each halving of the grid size, there is essentially no justification for using the upwind scheme when easily programmed, higher order schemes such as the mono scheme are available. On two-dimensional codes, where a factor of 2 decrease in grid size costs a factor of 8 in execution time, such algorithm development becomes essential. For nonrelativistic hydrodynamics these difference schemes can be even further refined; see, e.g., Woodward and Colella (1981, 1982*a*, *b*) and Woodward (1983) on the use of Riemann solvers to obtain shock jumps. This procedure allows the resolution of a shock in only one grid zone. These methods, however, have not yet been extended to general relativistic hydrodynamics.

We next test the mono scheme in a stronger shock as assessed by the pressure jump across the shock. Instead of an initial pressure jump of 10 as in the Sod test problem, we use a jump of 10^7. For this problem the initial conditions are $\rho_l = 100$, $\varepsilon_l = 10^{-2}$, $P_l = 0.67$ to the left of $x = 35.5$ and $\rho_r = 1.0$,

© American Astronomical Society • Provided by the NASA Astrophysics Data System

1984ApJS...55..211H

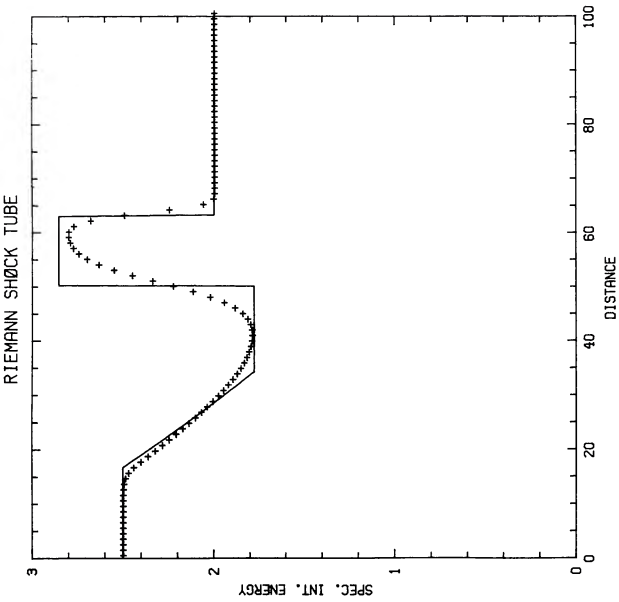


FIG. 6c

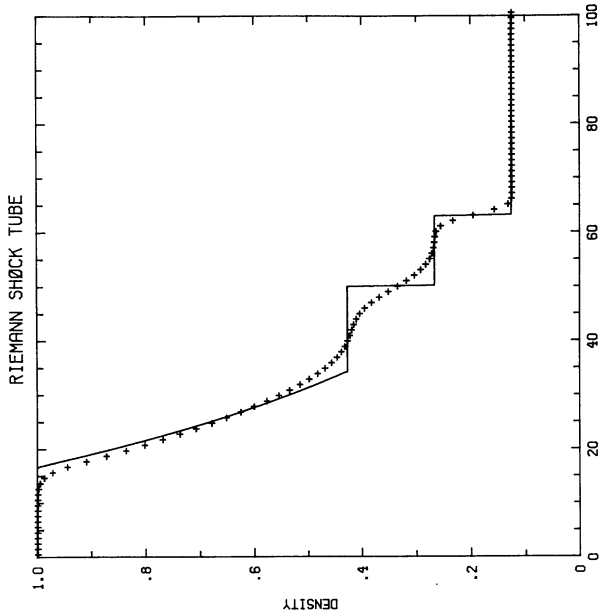


FIG. 6b

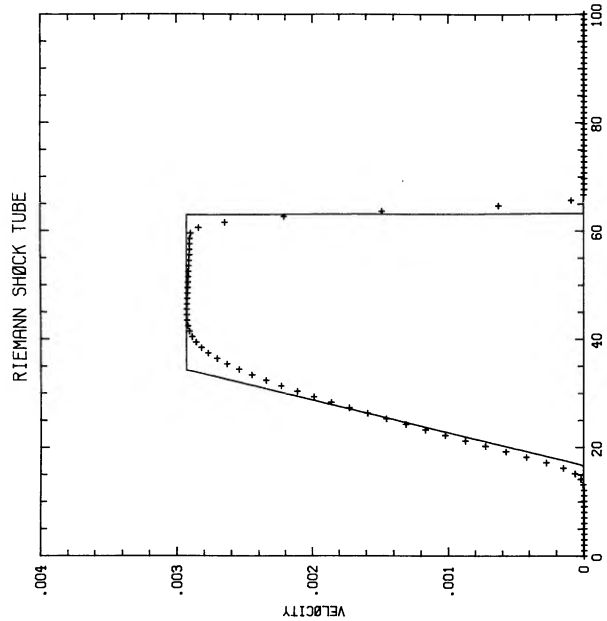


FIG. 6a

FIG. 6.—Results for the 100 zone Sod shock tube using the first-order upwind scheme.

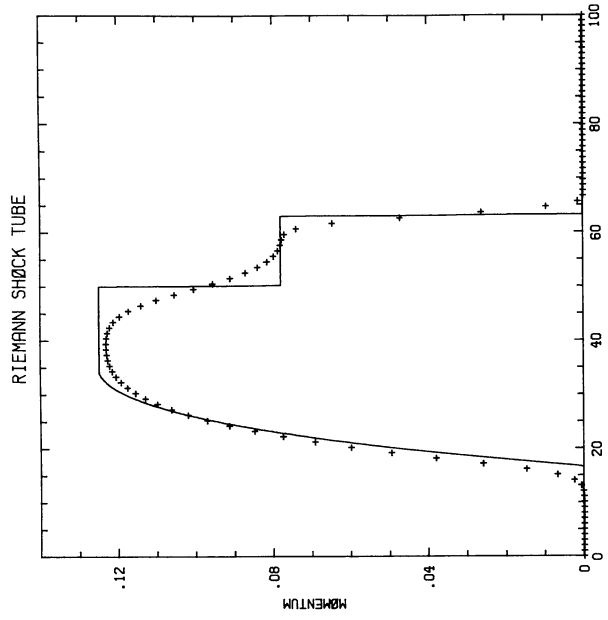


FIG. 6e

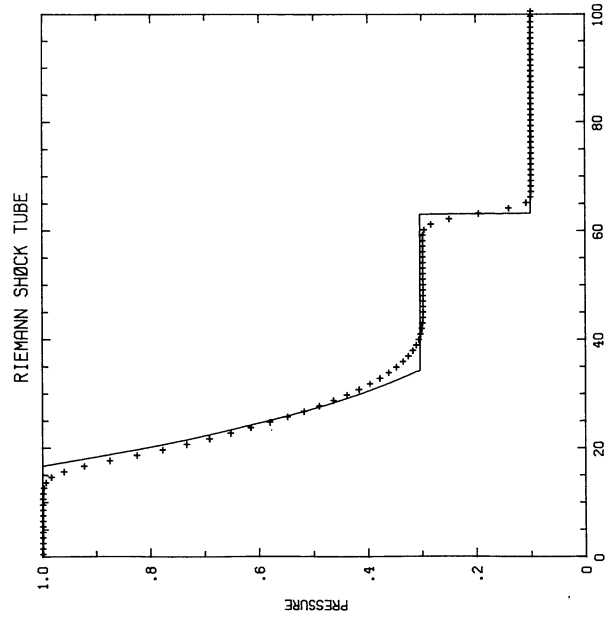


FIG. 6d

© American Astronomical Society • Provided by the NASA Astrophysics Data System

1984ApJS...55..211H

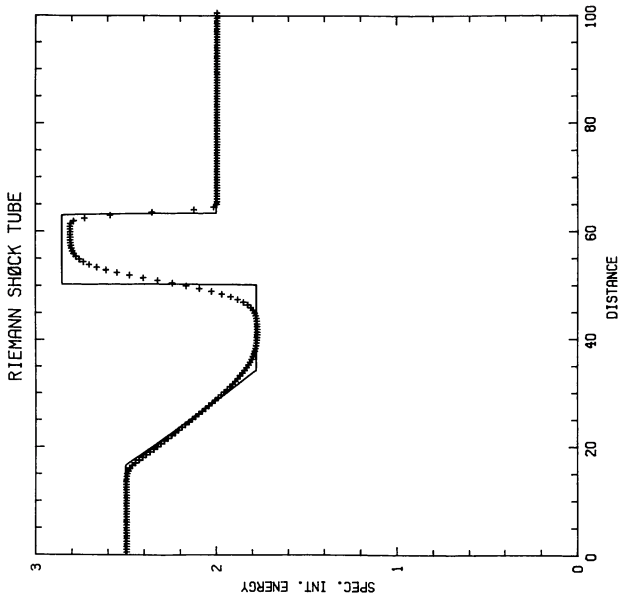


FIG. 7c

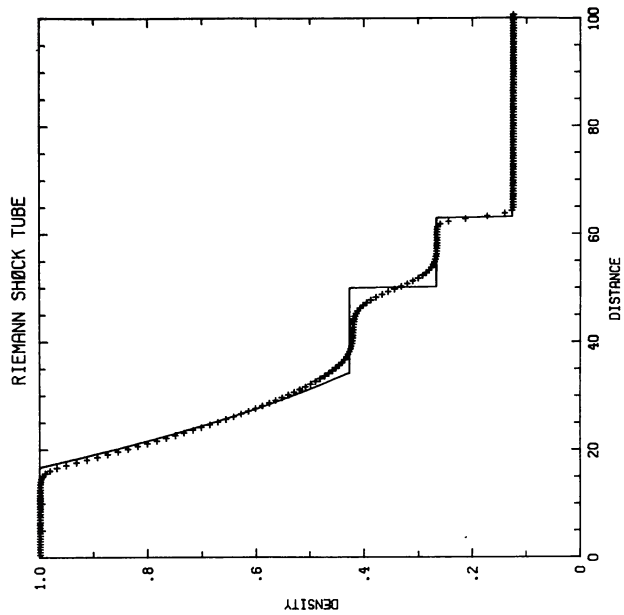


FIG. 7b

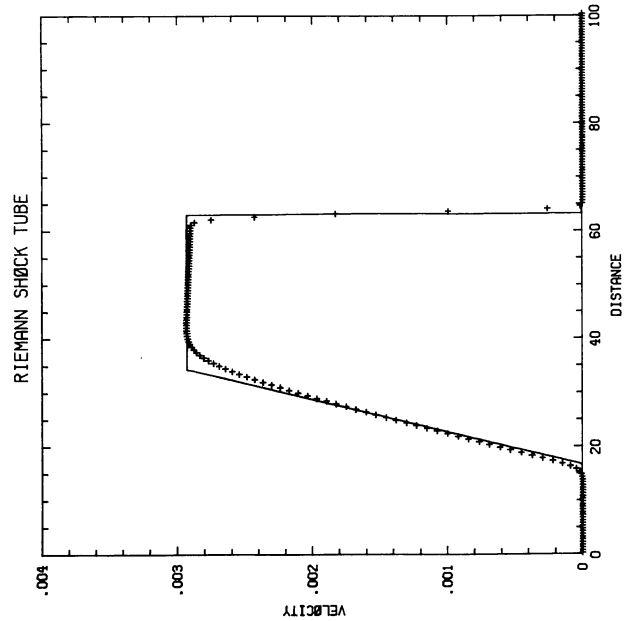


FIG. 7a

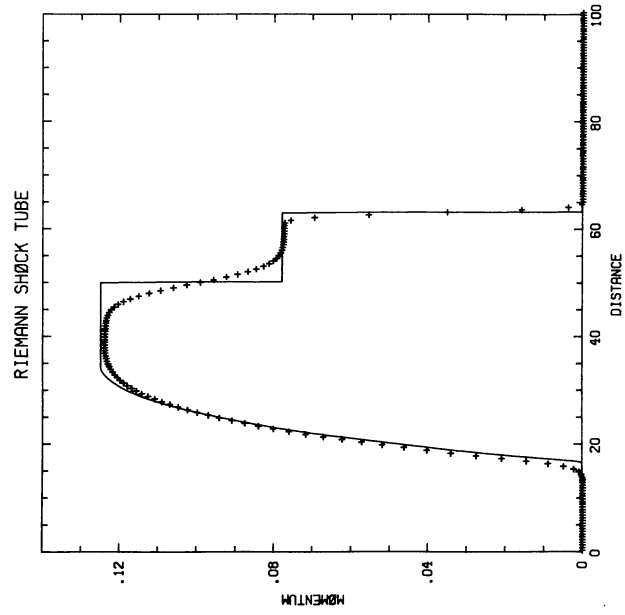


FIG. 7e

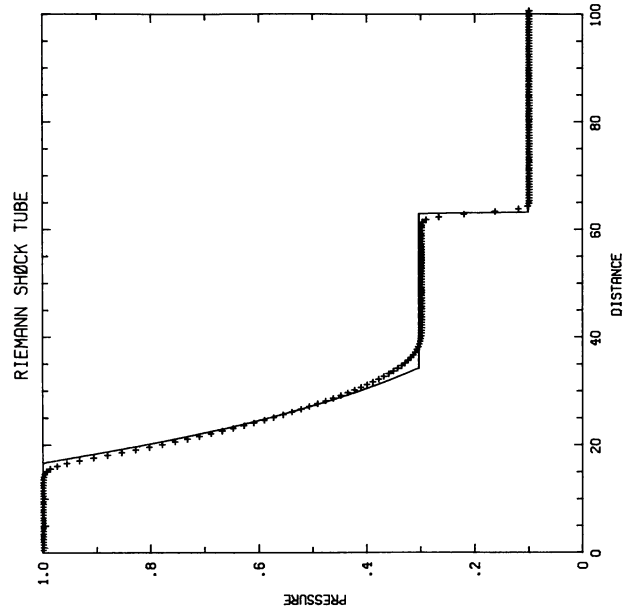


FIG. 7d

FIG. 7.—Results for the 200 zone Sod shock tube using the first-order upwind scheme.

© American Astronomical Society • Provided by the NASA Astrophysics Data System

1984ApJS...55..211H

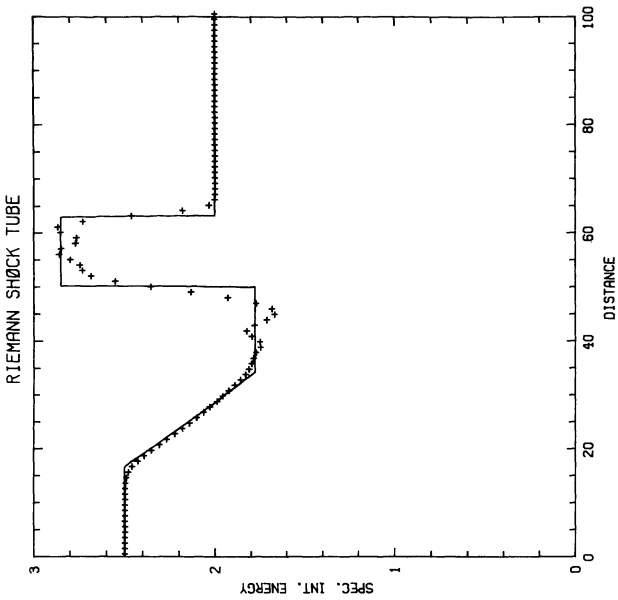


FIG. 8c

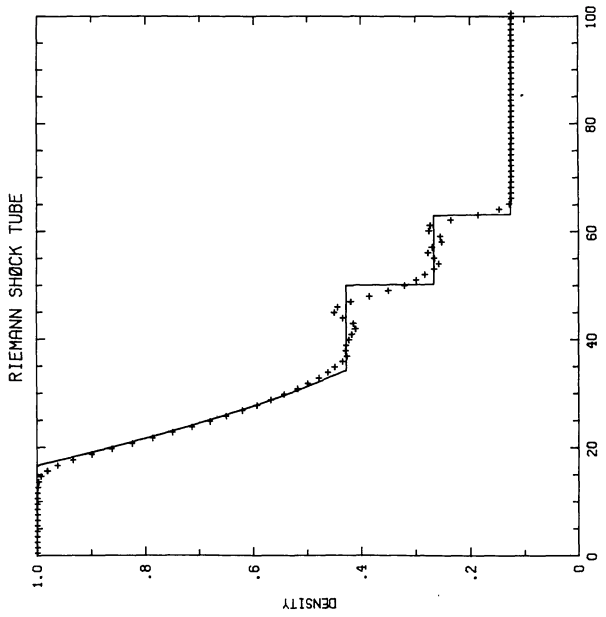


FIG. 8b

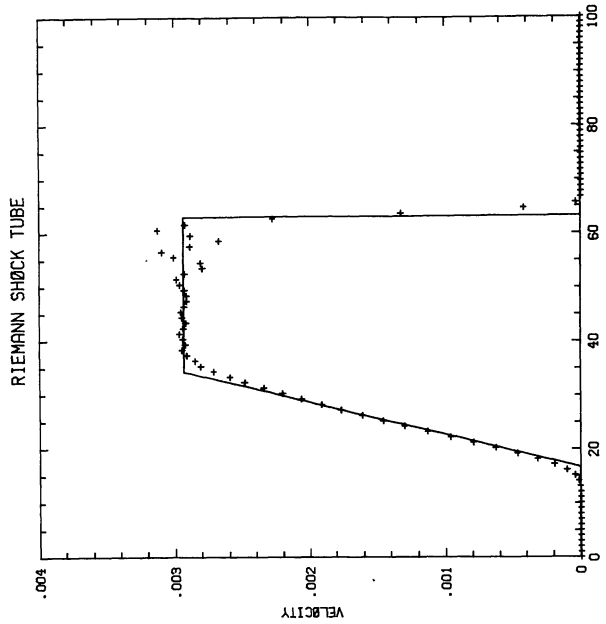


FIG. 8a

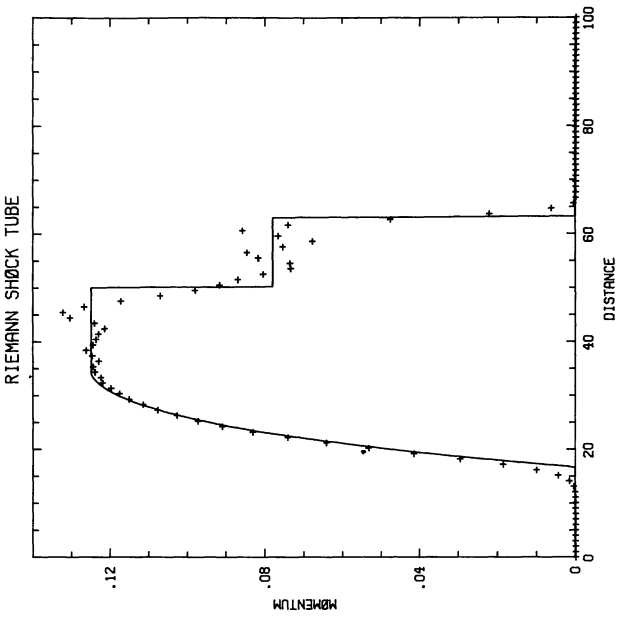


FIG. 8e

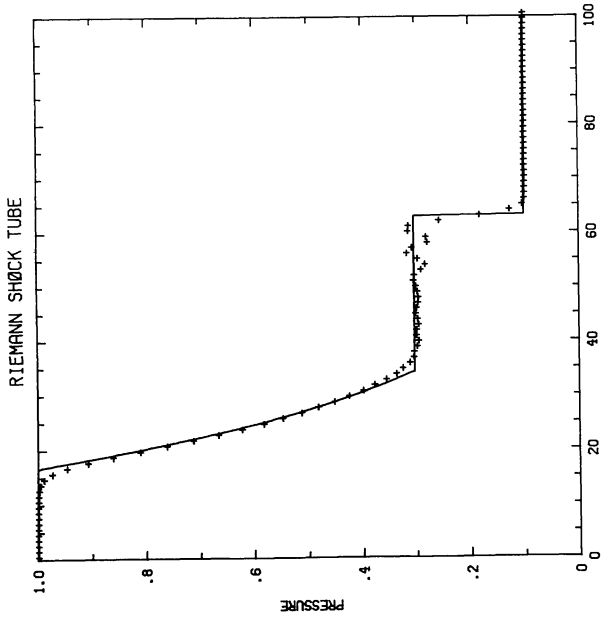


FIG. 8d

FIG. 8.—Results for the 100 zone Sod shock tube using the Wilson scheme.

© American Astronomical Society • Provided by the NASA Astrophysics Data System

1984ApJS...55..211H

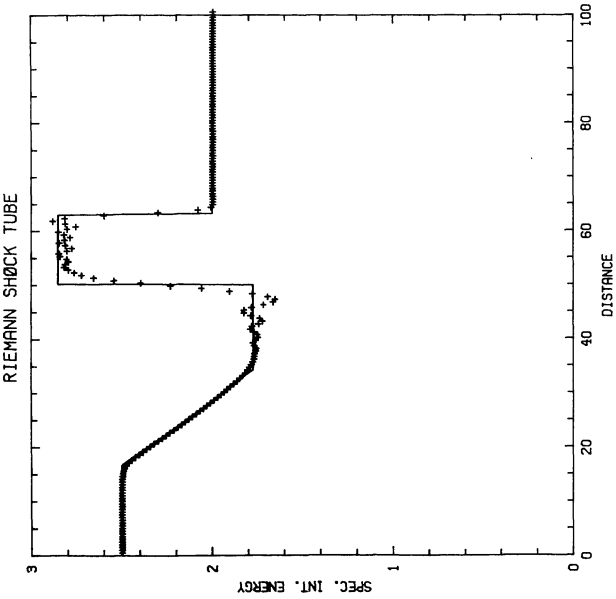


FIG. 9c

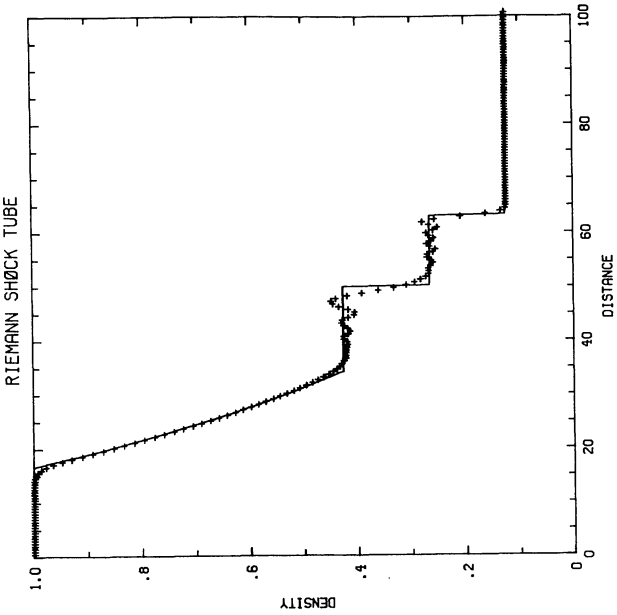


FIG. 9b

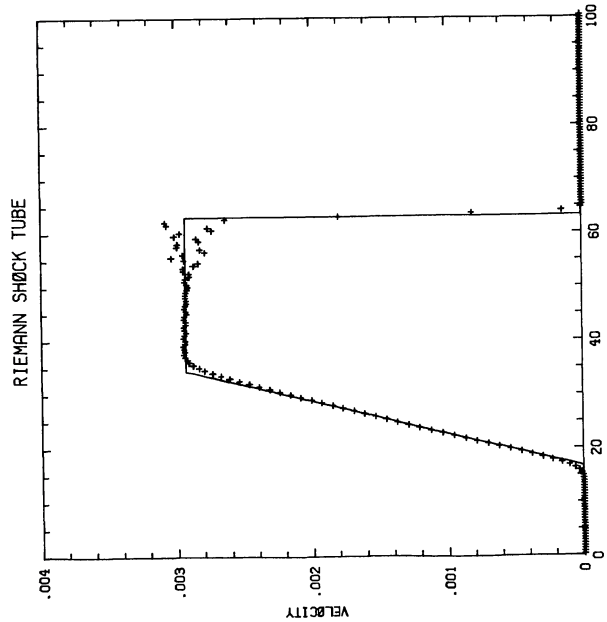


FIG. 9a

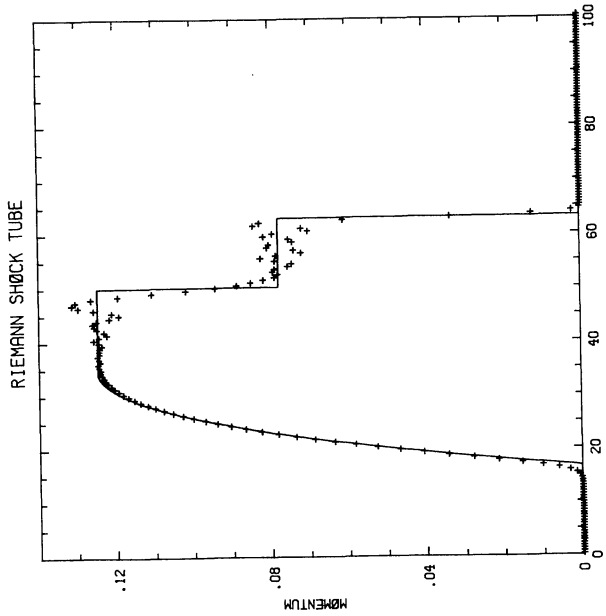


FIG. 9e

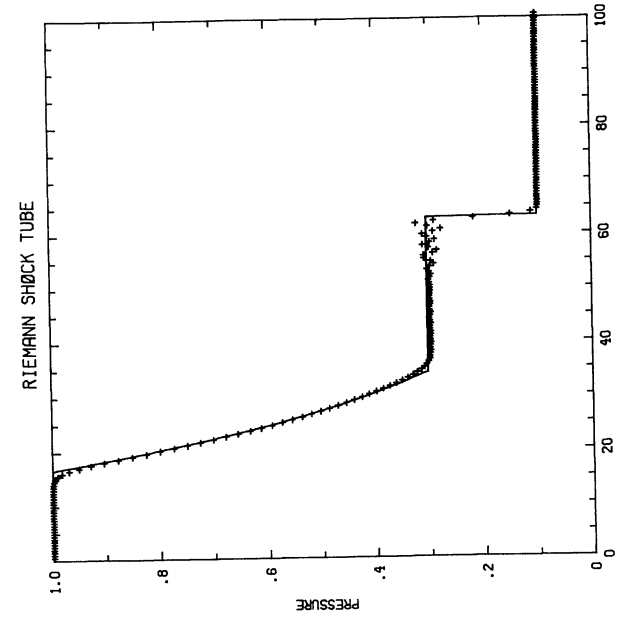


FIG. 9d

FIG. 9.—Results for the 200 zone Sod shock tube using the Wilson scheme.

© American Astronomical Society • Provided by the NASA Astrophysics Data System

1984ApJS...55..211H

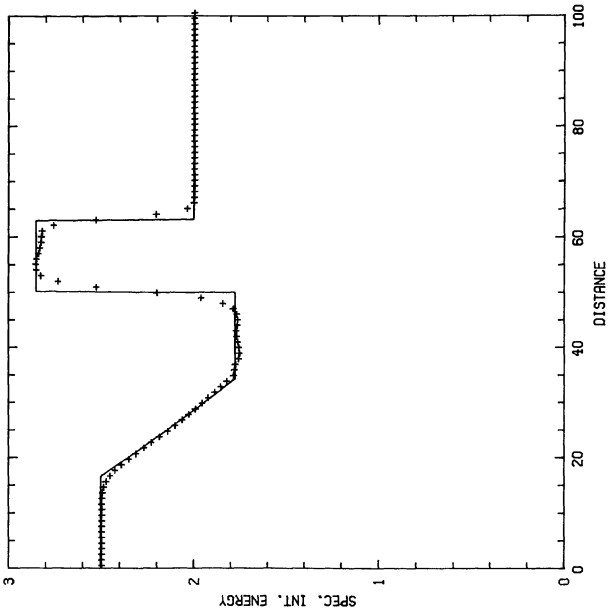


FIG. 10c

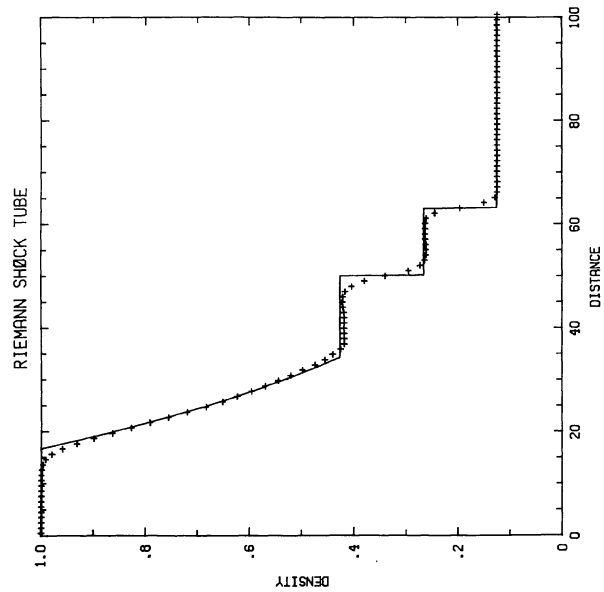


FIG. 10b

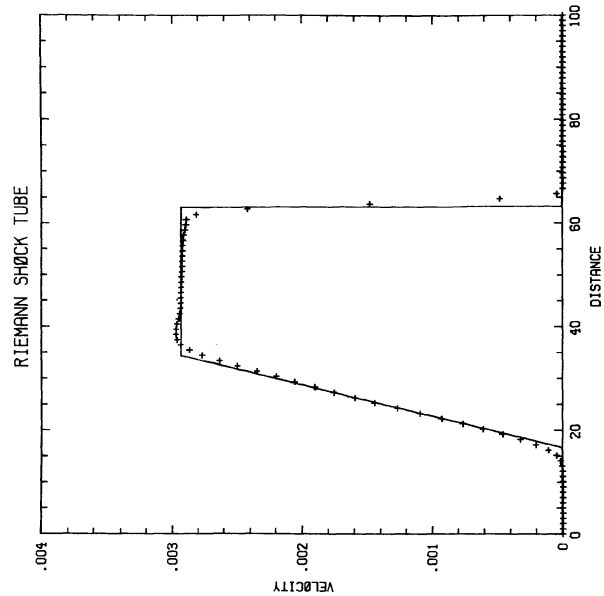


FIG. 10a

FIG. 10.—Results for the 100 zone Sod shock tube using Barton's scheme.

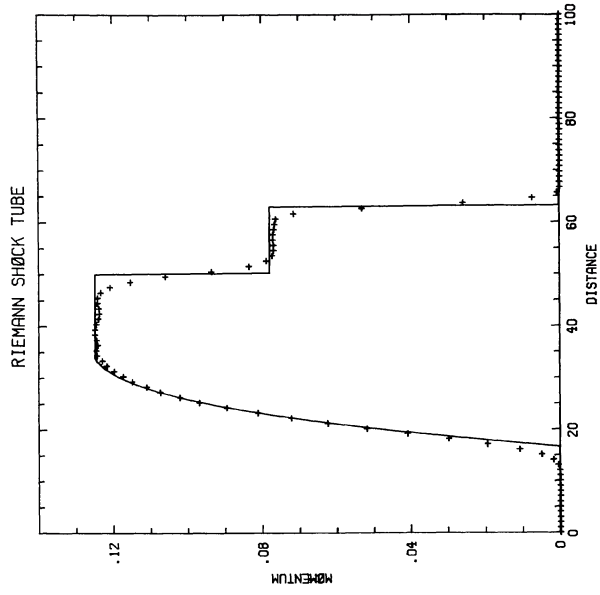


FIG. 10e

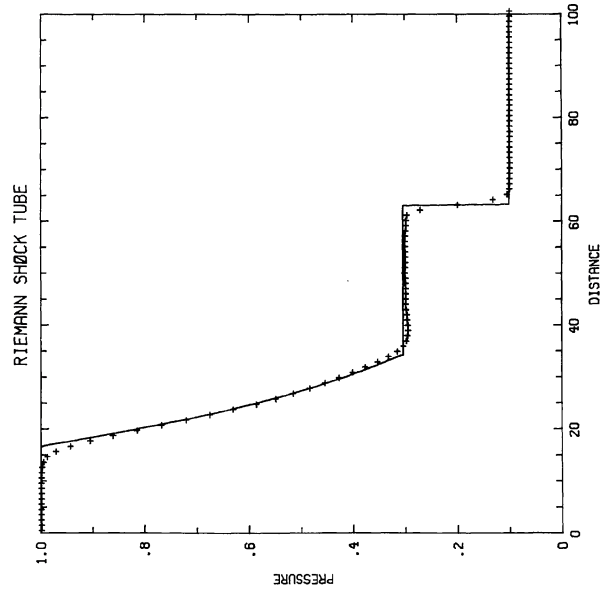


FIG. 10d

© American Astronomical Society • Provided by the NASA Astrophysics Data System

1984ApJS...55..211H

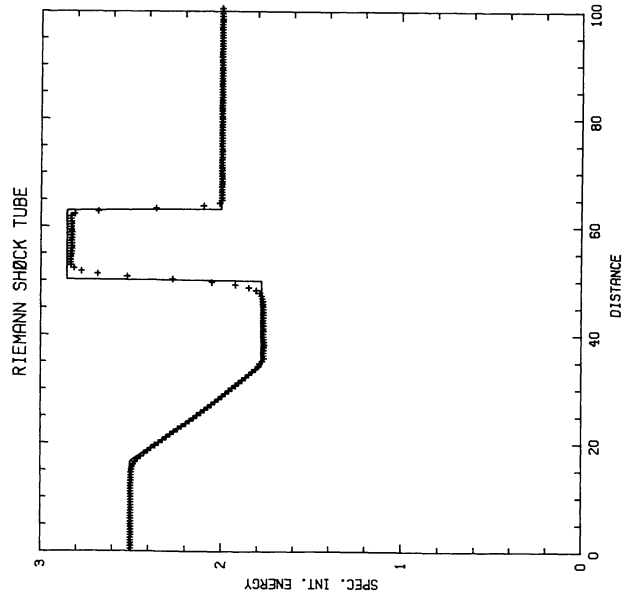


FIG. 11*c*

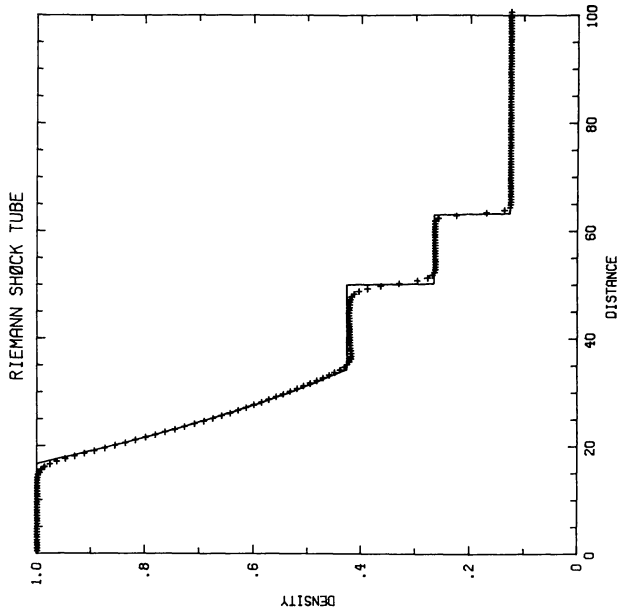


FIG. 11*b*

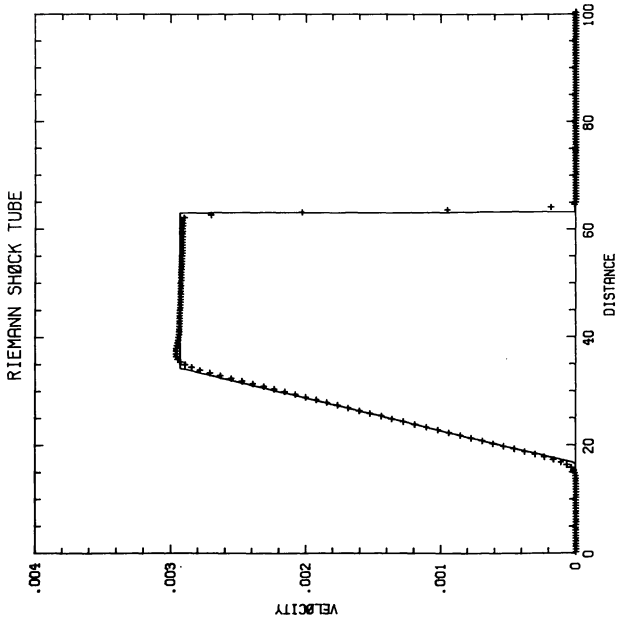


FIG. 11*a*

FIG. 11.—Results for the 200 zone Sod shock tube using Barton's scheme.

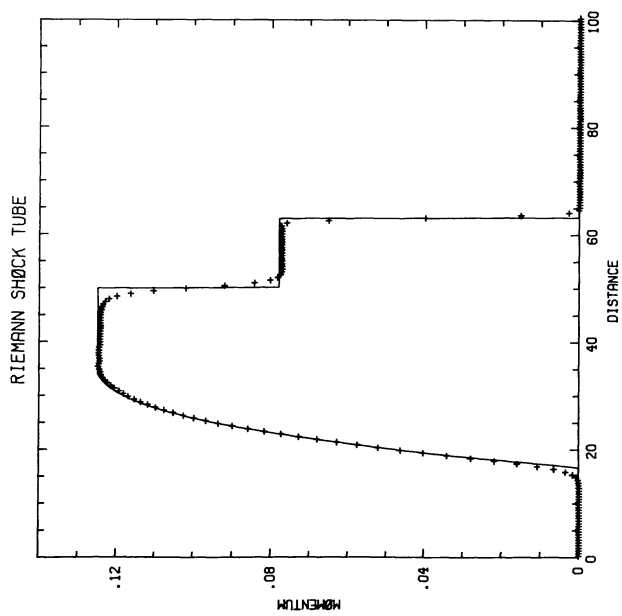


FIG. 11*e*

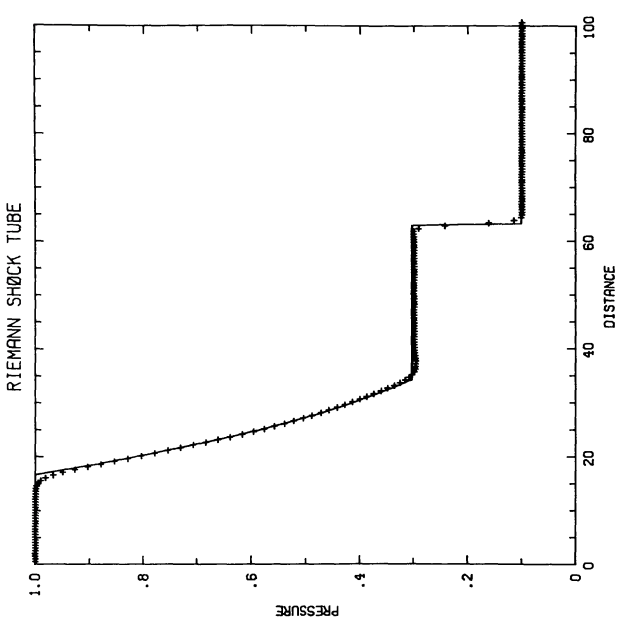


FIG. 11*d*

© American Astronomical Society • Provided by the NASA Astrophysics Data System

1984ApJS...55..211H

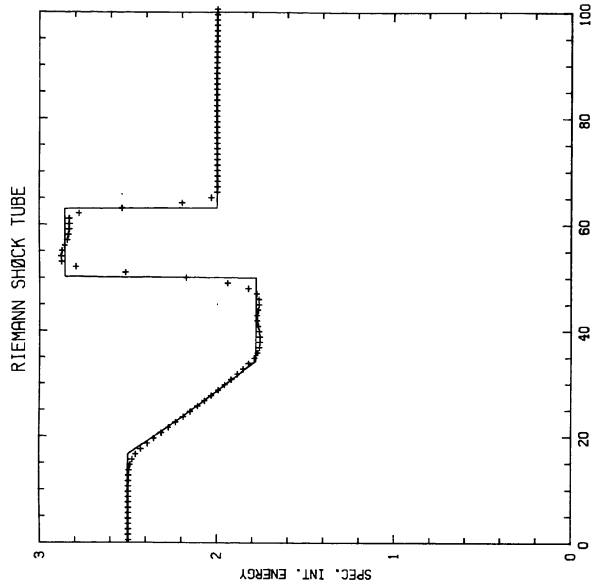


FIG. 12c

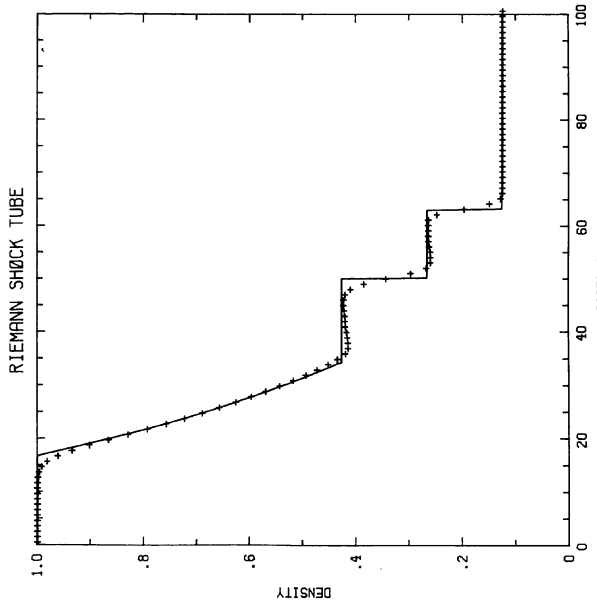


FIG. 12b

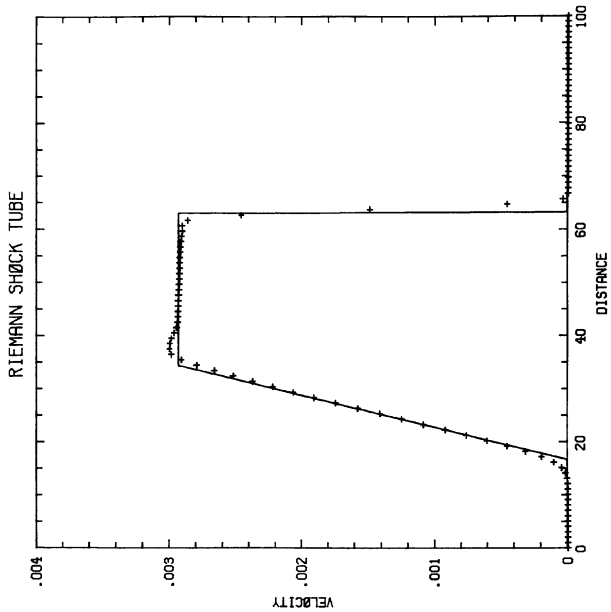


FIG. 12a

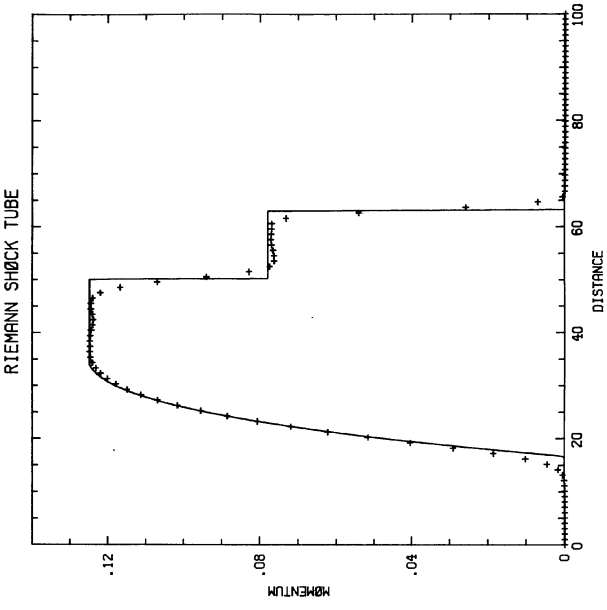


FIG. 12e

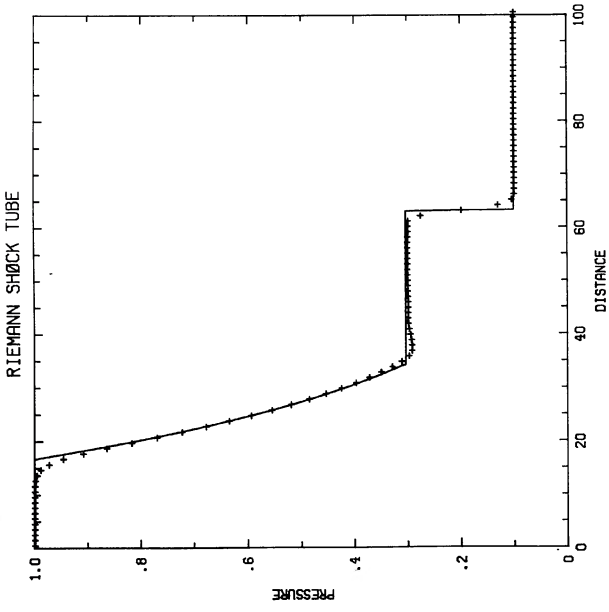


FIG. 12d

FIG. 12.—Results for the 100 zone Sod shock tube using the mono scheme.

© American Astronomical Society • Provided by the NASA Astrophysics Data System

1984ApJS...55..211H

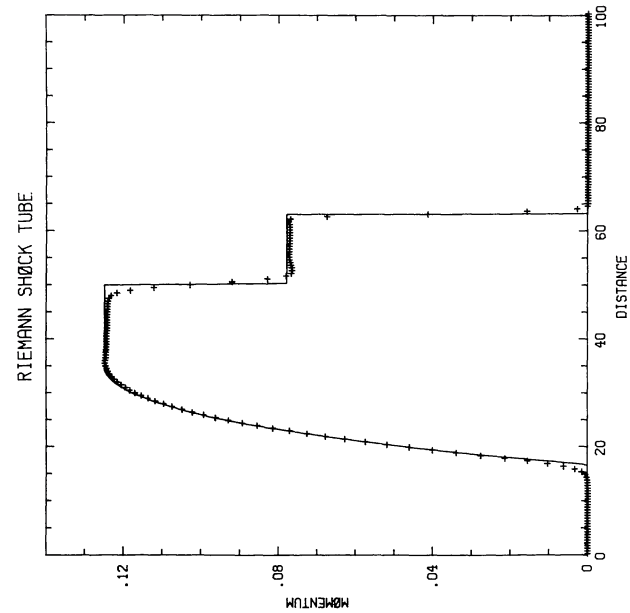


FIG. 13*c*

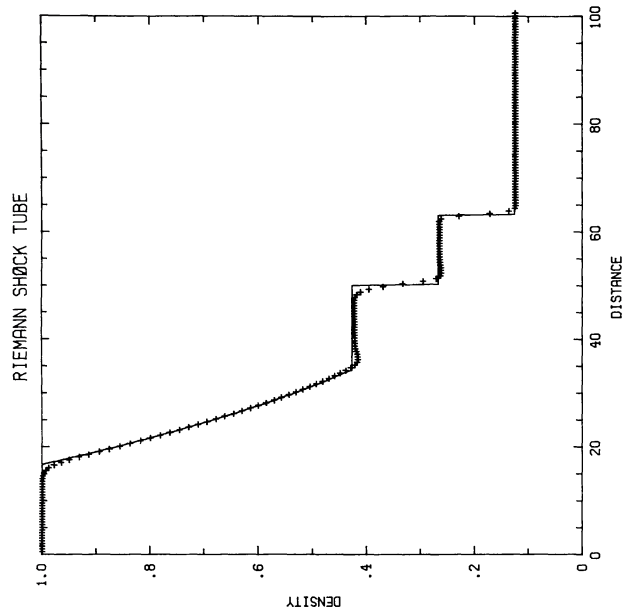


FIG. 13*b*

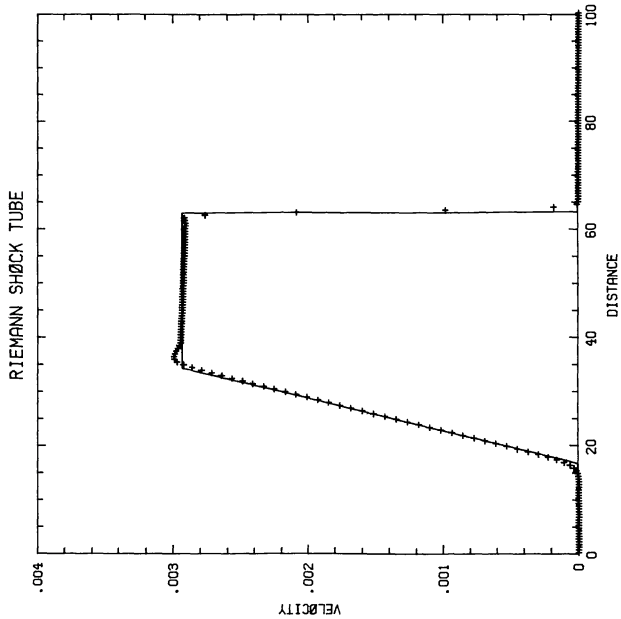


FIG. 13*a*

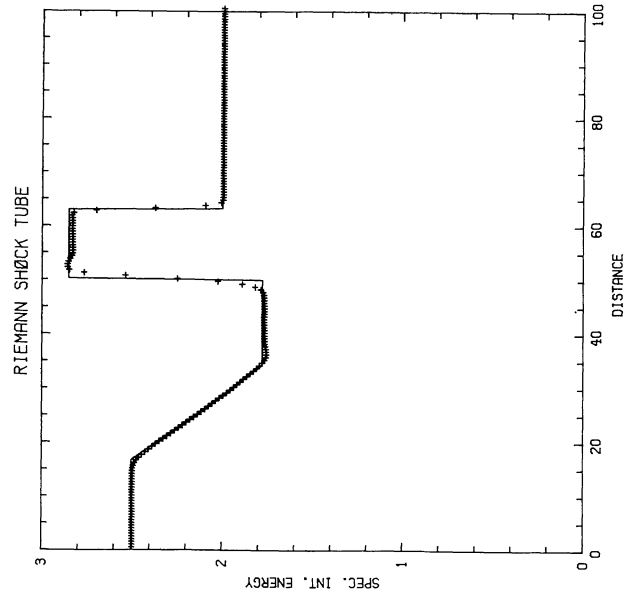


FIG. 13*e*

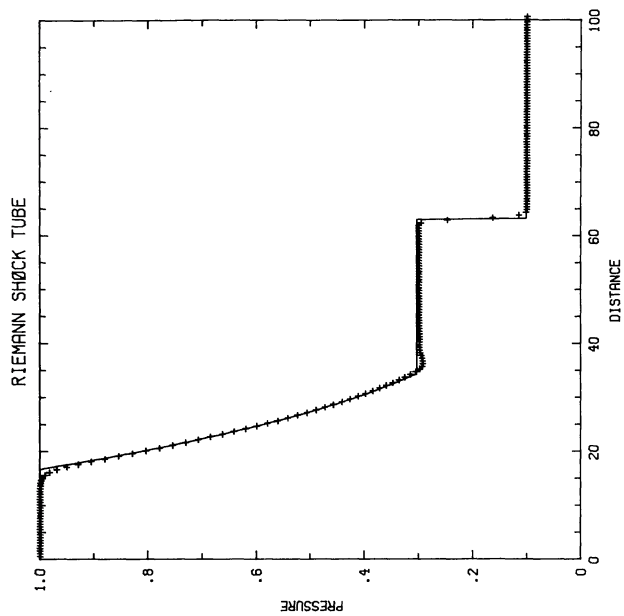


FIG. 13*d*

FIG. 13.—Results for the 200 zone Sod shock tube using the mono scheme.

© American Astronomical Society • Provided by the NASA Astrophysics Data System

1984ApJS...55..211H

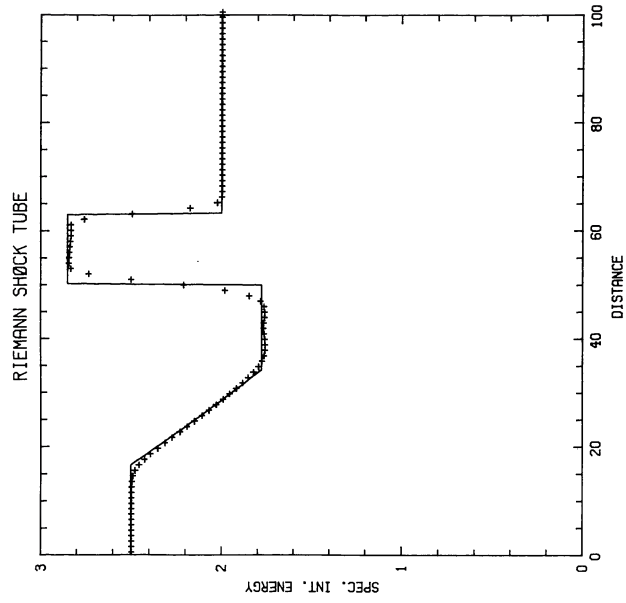


FIG. 14*c*

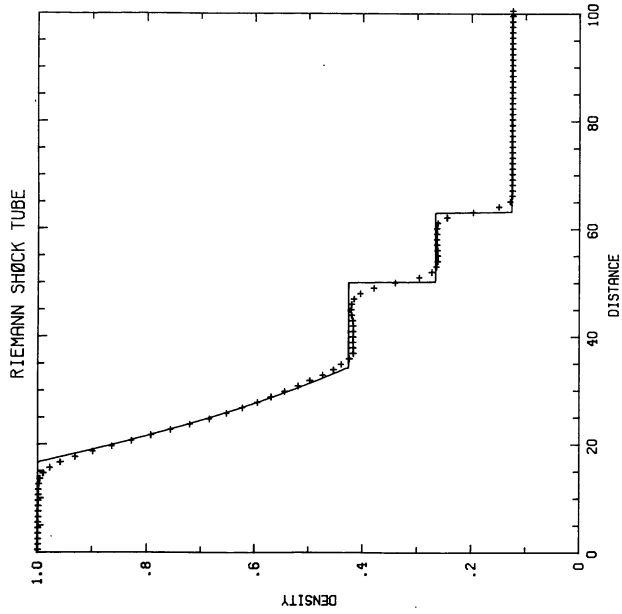


FIG. 14*b*

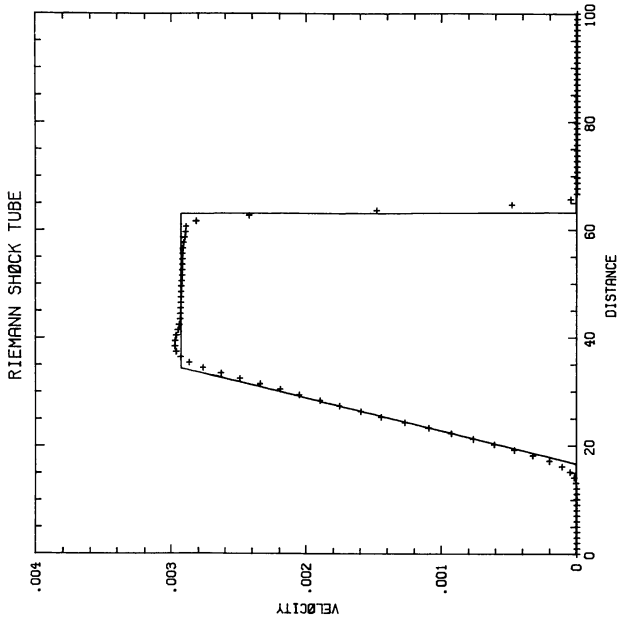


FIG. 14*a*

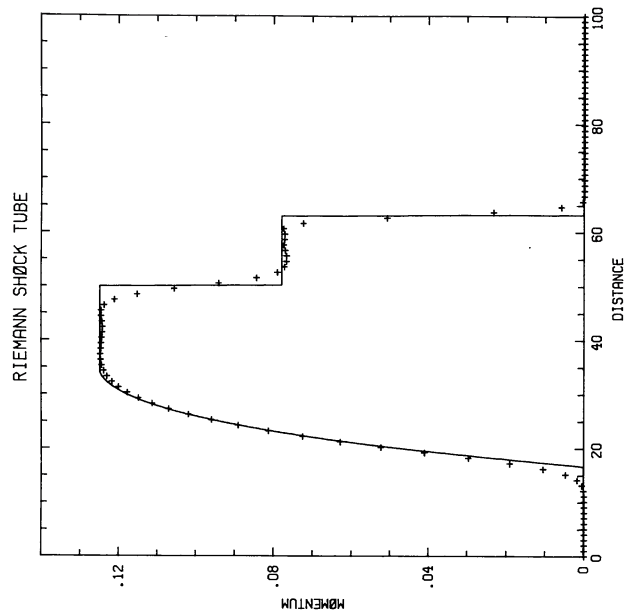


FIG. 14*e*

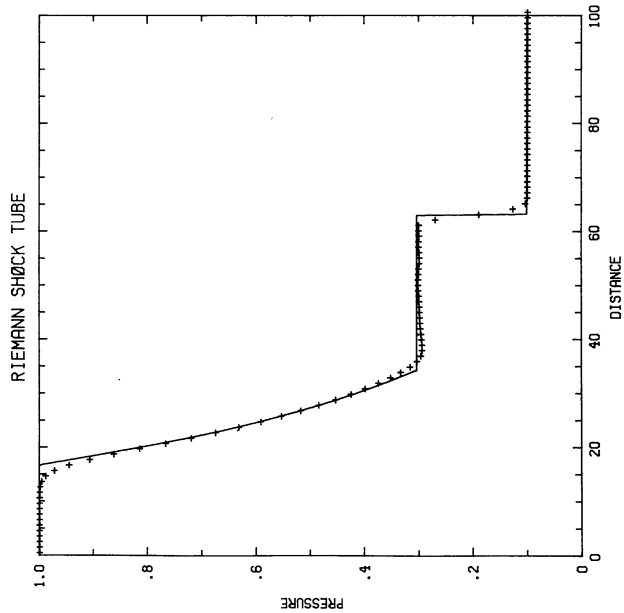


FIG. 14*d*

FIG. 14.—Results for the 100 zone Sod shock tube using consistent advection.

© American Astronomical Society • Provided by the NASA Astrophysics Data System

1984ApJS...55..211H

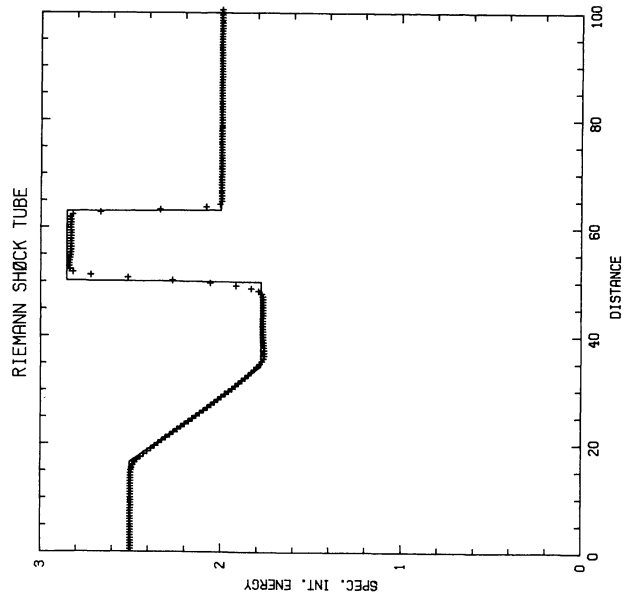


FIG. 15c

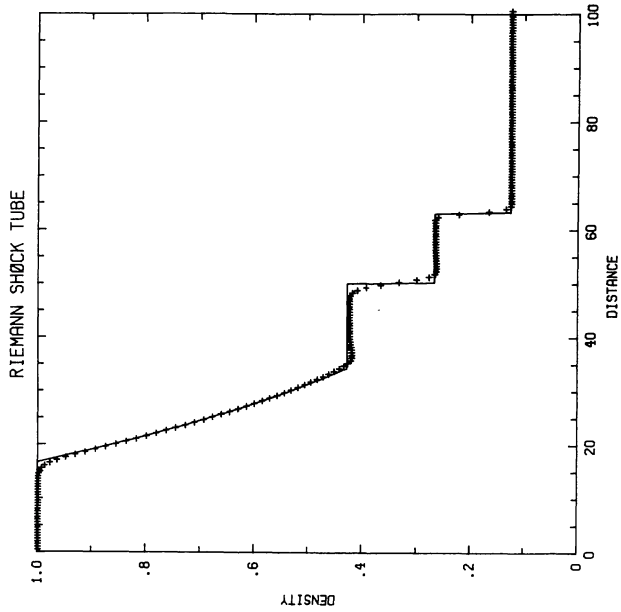


FIG. 15b

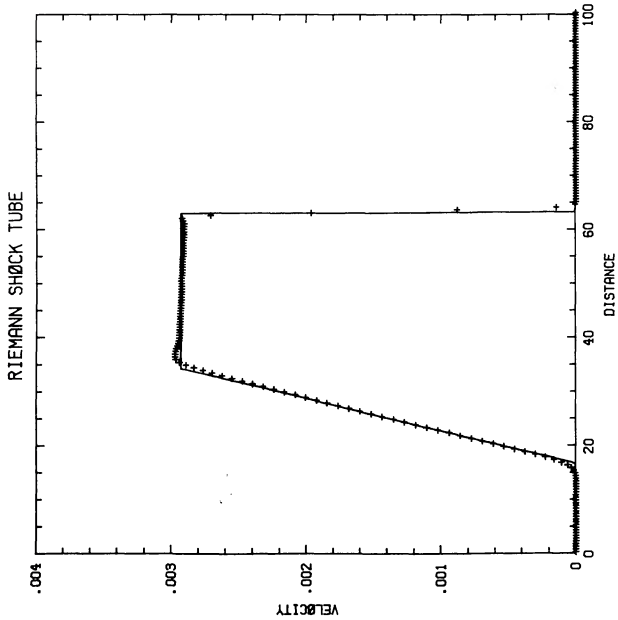


FIG. 15a

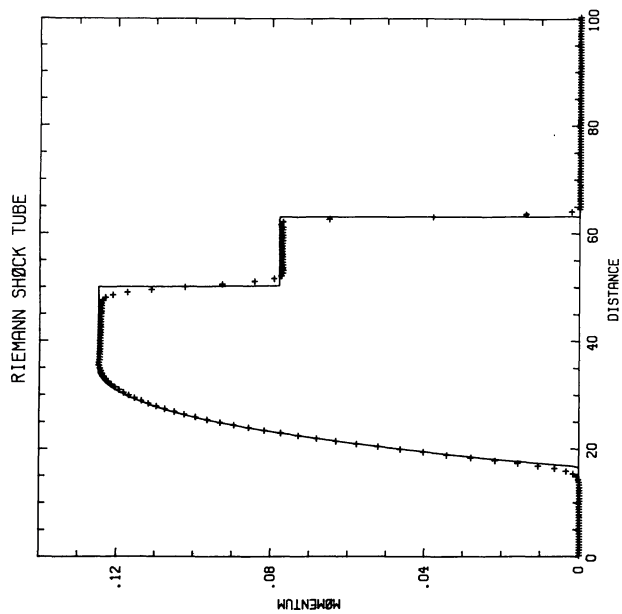


FIG. 15e

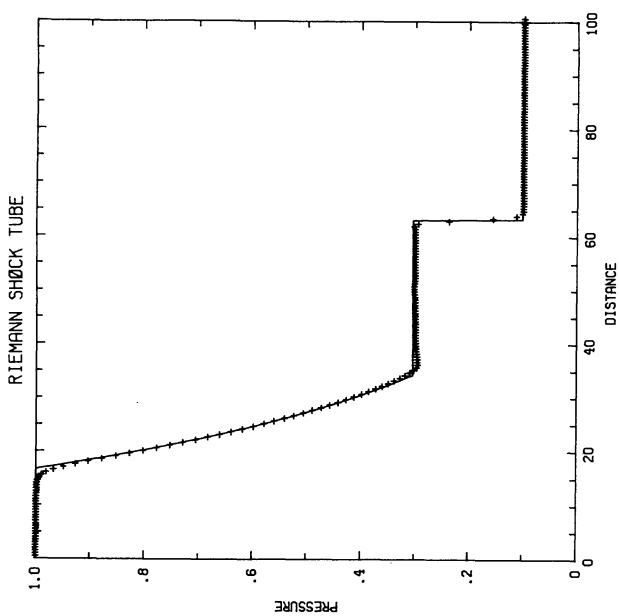


FIG. 15d

FIG. 15.—Results for the 200 zone Sod shock tube using consistent advection.

© American Astronomical Society • Provided by the NASA Astrophysics Data System

1984ApJS...55..211H

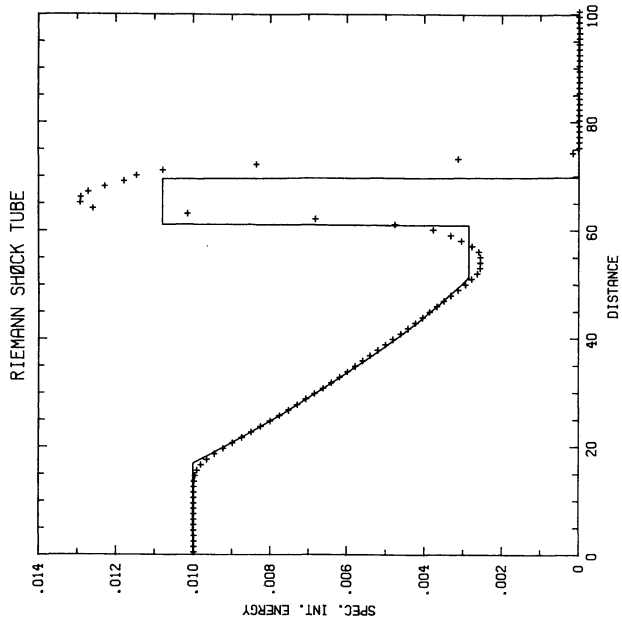


FIG. 16*c*

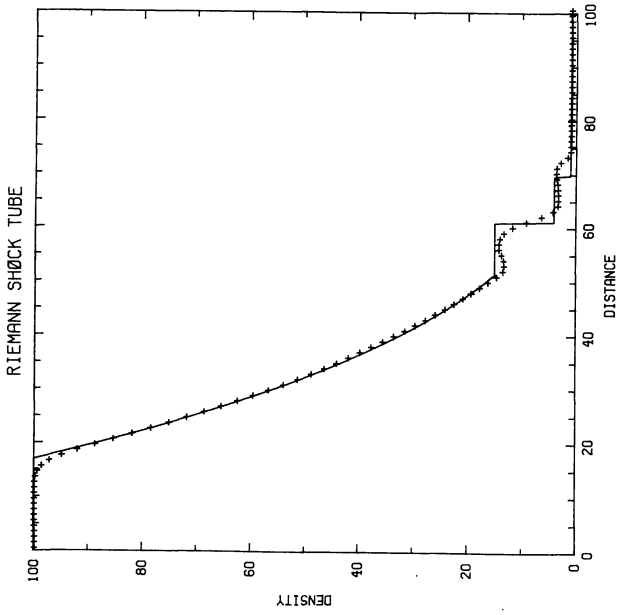


FIG. 16*b*

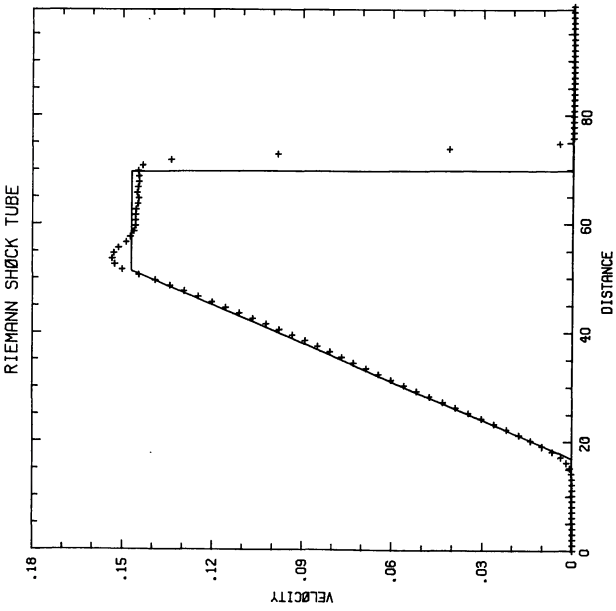


FIG. 16*a*

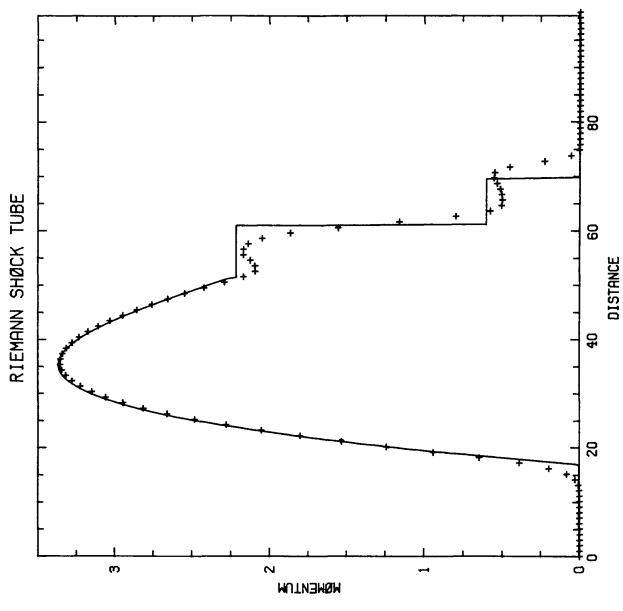


FIG. 16*e*

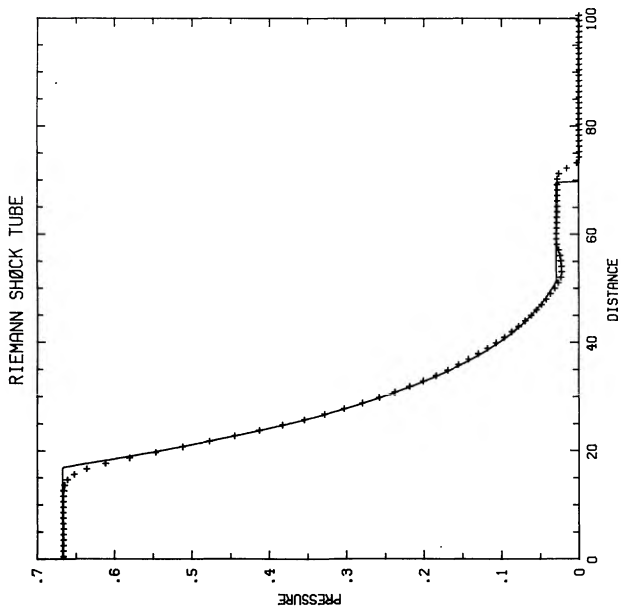


FIG. 16*d*

FIG. 16.—Strong shock tube results using 100 zones with the mono scheme.

© American Astronomical Society • Provided by the NASA Astrophysics Data System

1984ApJS...55..211H

TABLE 2

NUMERICAL RESULTS OF STRONG SHOCK TUBE TEST[a]

Scheme	V	ρ_l	ρ_r	ε_l	ε_r	P
Analytic	0.147	15.0	4.0	2.84×10^{-3}	1.08×10^{-2}	2.88×10^{-2}
100 zone mono[b] ...	0.145	13.7	3.64	2.53	1.26	2.84
500 zone mono	0.146	15.4	4.05	2.84	1.09	2.88

[a]Using the mono scheme in 100 zone and 500 zone runs.
[b]Average values; ε_l and ε_r are the local minimum and maximum values.

$\varepsilon_r = 10^{-7}$, $P_r = 0.67\times10^{-7}$ to the right. The equation of state gamma is 5/3. We begin by using a 100 zone grid with $\Delta x = 1$ and $\Delta t = 0.75$, values which yield a Courant number in approximately the same range as before. This problem is run to time $t = 230M$, and the results for mono transport are plotted in Figure 16; numerical values are listed in Table 2.

The overshoot noted in the previous test is even more apparent here and has become a significant effect on a length scale comparable with the physical features of the shock tube. A 500 zone run, however (Fig. 17), shows that these problems are due purely to discretization error; finer griding restores the accurate solution. This demonstrates the point that the number of zones needed to properly resolve a physical feature is a function of the change in magnitude of the dynamic variables over the region of interest. Here we have gone from a shock with a pressure jump $[P] = 3$ to $[P] = 4.3\times10^5$, where $[P]$ is the ratio of the pressure across the shock; this transition occurs over five zones in both cases. This test has shown that while the proper resolution of very strong features requires fine zoning, the mono scheme can still reveal the qualitative features of the dynamic flow on a much coarser grid.

While we will not display the results from using the other schemes, some comments will be made on their relative performance on the strong shock problem. The numerical diffusion of the upwind scheme is enough to completely lose the contact discontinuity; it becomes barely apparent in the 500 zone run. The ringing noted earlier remains in the Wilson scheme, seriously degrading the 100 zone run. In a 500 zone run the effect occurs in much shorter wavelengths and has much less dynamic effect; fairly good average values are obtained. The consistent advection scheme yields results quite similar to the mono scheme, except that the postcontact specific internal energy is undervalued by 7%.

In general, the results of the strong shock test reconfirm our earlier conclusion: the mono scheme dramatically outperforms the other nonmonotonic schemes. Barton's scheme yields comparable results, but it is slightly more complicated to code and requires more calculations per time step. Since the change in coding required to implement the mono scheme is slight, its use can be unconditionally recommended. While it appears best to not employ consistent advection in the shock tube problem, it is easy to include and must be considered when the important dynamic variables will be specific energy or specific angular momentum.

b) *Relativistic Shock Tests*

We continue testing the mono scheme with a more general and more difficult problem, the relativistic shock tube. Such a test provides the first opportunity to explore the special relativistic terms in the code. The tests described here are also performed by Centrella and Wilson (1984) for the Barton scheme. As before, two questions are at issue: the relativistic jump conditions and the propagation of a relativistic nonlinear rarefaction wave.

Before turning to specific results we first outline the way in which a shock discontinuity is handled numerically. In an actual physical shock, viscosity acts to convert bulk motion of the fluid into random motion of the fluid molecules. Left to its own devices, a numerical fluid will behave in the same way, except that, because a numerical "molecule" is a grid zone with thickness Δx, the results will be disastrous; unstable zone-to-zone oscillations are guaranteed. To overcome this problem of finite molecular size, an artificial viscosity Q is introduced to transfer energy from bulk kinetic to heat. Such a term enters the stress energy equation as a bulk viscosity times the convergence of the fluid four-velocity (see eq. [11], Paper I). Equation (19) above describes the numerical form for Q.

Given this analysis, it might be expected that Q should enter into the fluid equations in all places where one finds the isotropic pressure P. To test this idea, we consider those terms in equations (2) and (3) which are common to both the special relativistic and Newtonian equations. This yields the following additional finite difference terms:

Pressure gradient force:

$$S_j^{n+1} = S_j^n - \Delta t(Q_j - Q_{j-1})/\Delta r a_j.$$

Compressive heating:

$$E_j^{n+1} = E_j^n - \Delta t Q_j(V_{j+1} - V_j)/\Delta r b_j. \tag{44}$$

Recall that Q is nonzero only where there is local compression. Note that the full momentum equation (2) has the same Q terms in both the Newtonian and the special relativistic formulation. In the fully relativistic formulation of the energy equation, however, the compression heating term in equation 44,

$$Q\partial_i(V^i),$$

must be replaced by the relativistically correct form:

$$\frac{Q}{\sqrt{\gamma}}\partial_i(\sqrt{\gamma}\,V^iW) + Q\partial_t W. \tag{45}$$

In addition, we must add Q to the total inertia, i.e., $\rho + \rho\varepsilon + P + Q$. The space derivative term in equation (45) is differenced in a straightforward manner (see eq. [16]). Adding Q to the inertia also presents no problem, but the time derivative of W is difficult to center properly in a time-explicit formulation; W

© American Astronomical Society • Provided by the NASA Astrophysics Data System

1984ApJS...55..211H

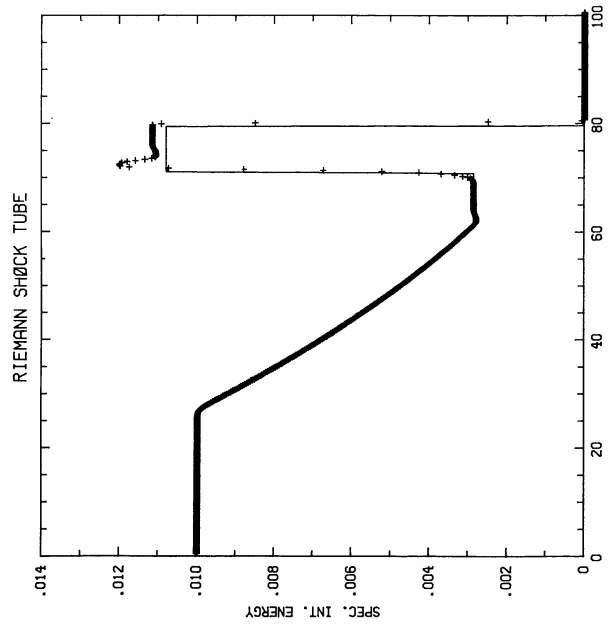


FIG. 17*c*

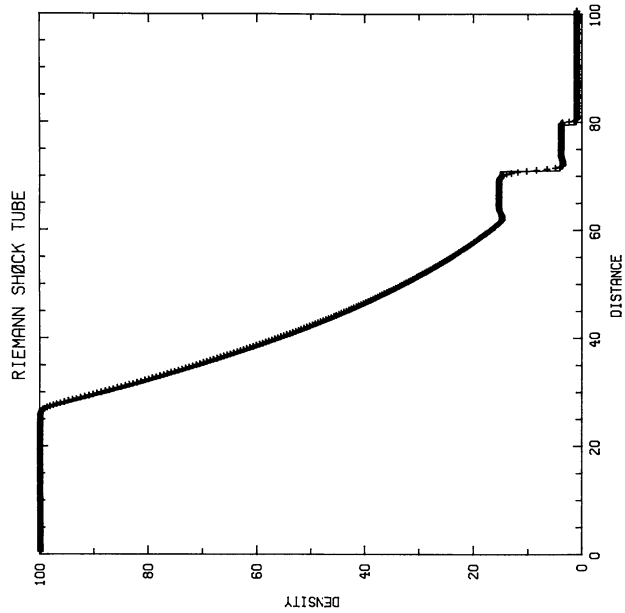


FIG. 17*b*

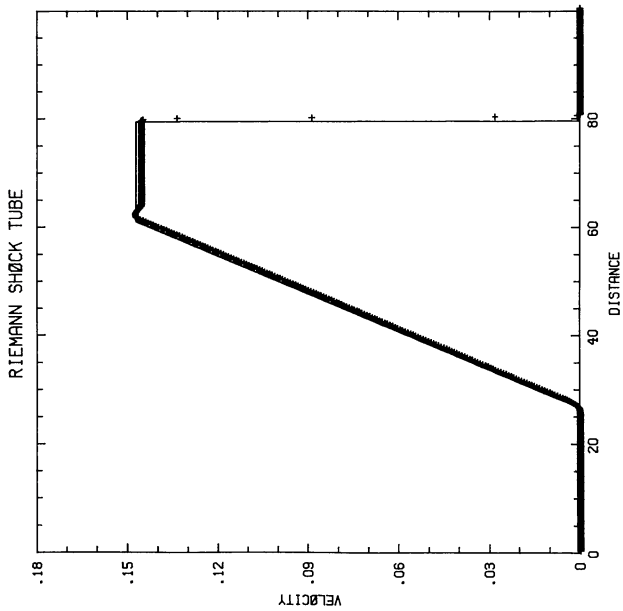


FIG. 17*a*

FIG. 17.—Strong shock tube results using 500 zones with the mono scheme.

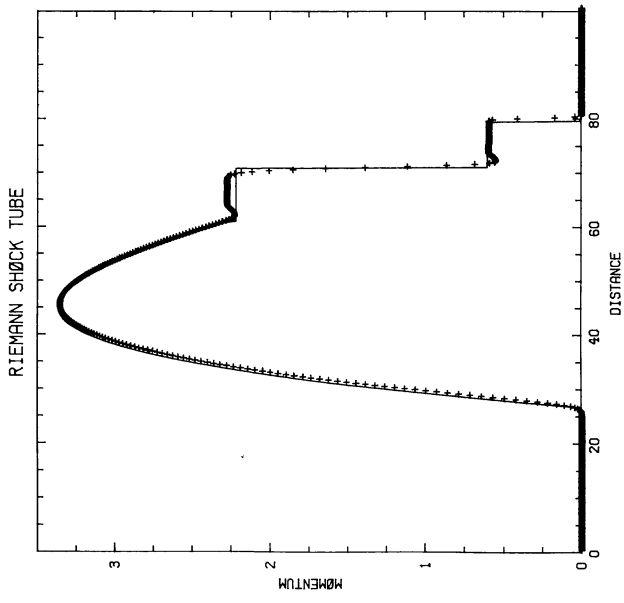


FIG. 17*e*

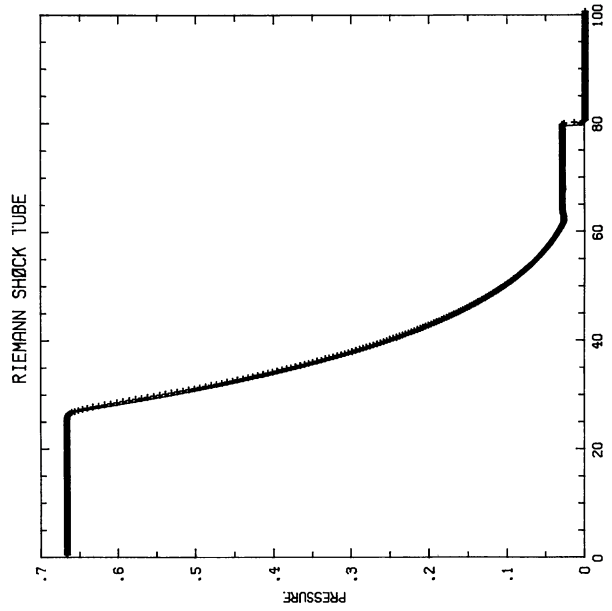


FIG. 17*d*

© American Astronomical Society • Provided by the NASA Astrophysics Data System

© American Astronomical Society • Provided by the NASA Astrophysics Data System

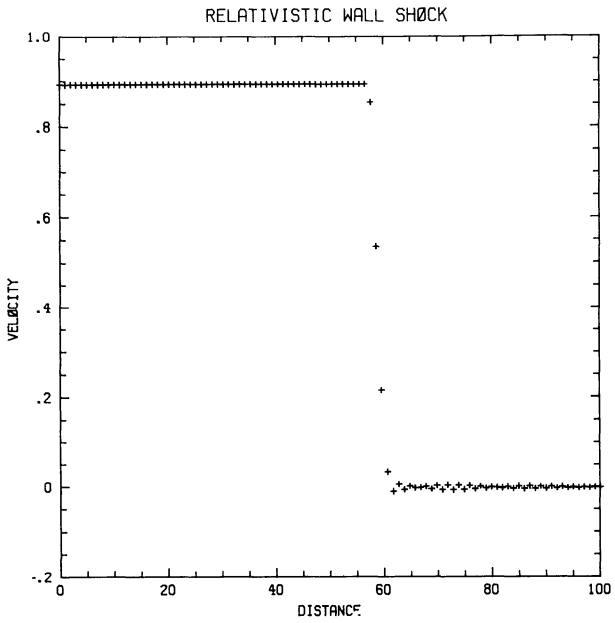


FIG. 18*a*

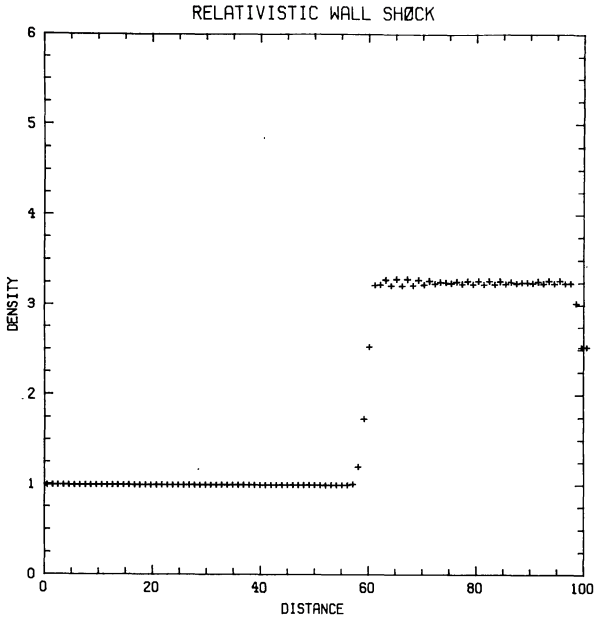


FIG. 18*b*

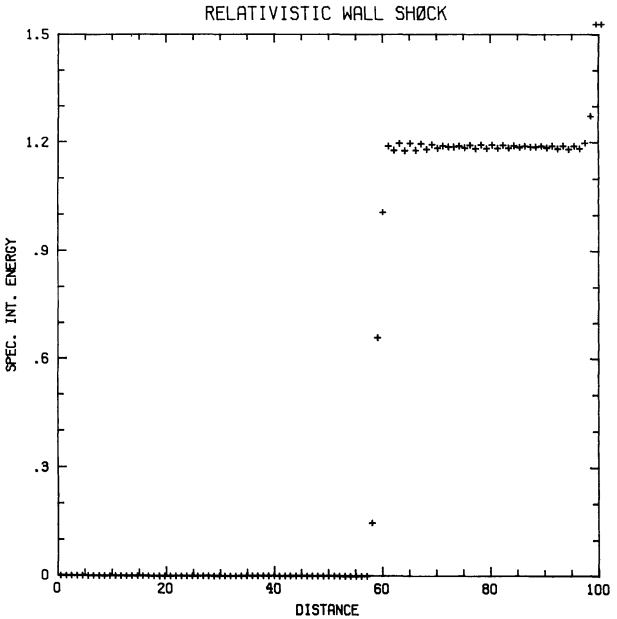


FIG. 18*c*

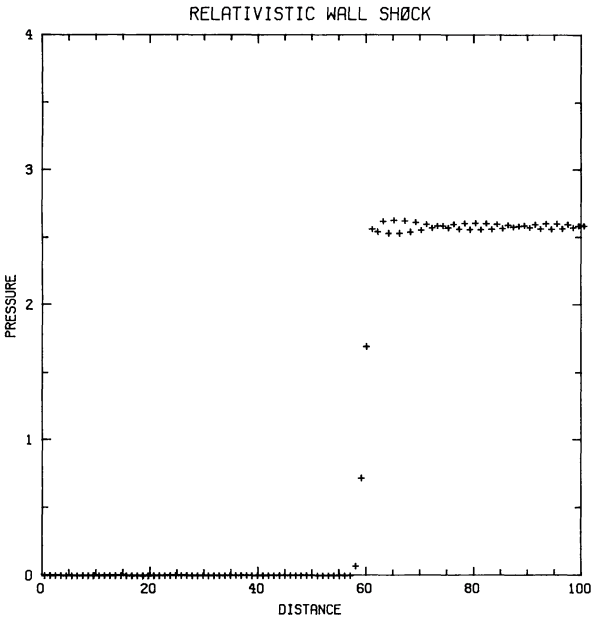


FIG. 18*d*

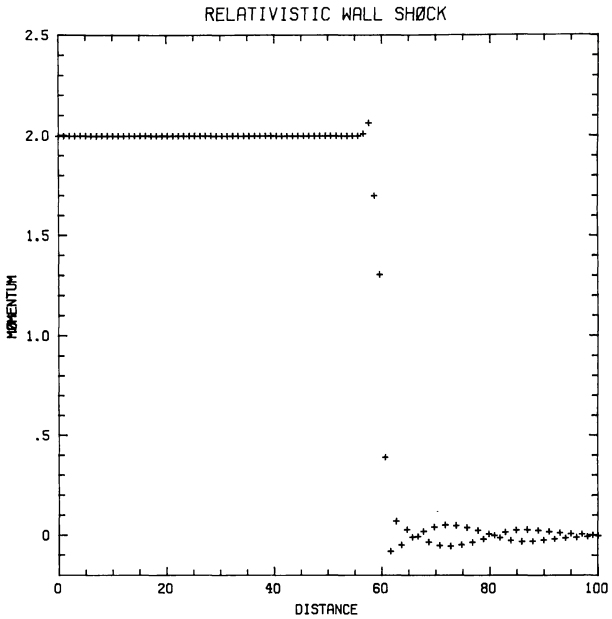


FIG. 18*e*

FIG. 18.—An example of the relativistic wall shock problem using the mono scheme with the term $Q/\sqrt{\gamma}\,\partial_t(\sqrt{\gamma}\,WV^i)$ and Q in the inertia included. In this example $\Gamma = 5/3$, $W = 2.24$, yielding a compression ratio of 7.1. Thus, analytically we expect $\rho_2 = 3.17$ ($D_1 = \rho_1 W = 1.0$) and $\varepsilon_2 = 1.24$. Note the (damped) postshock zone-to-zone oscillations and the "wall heating" phenomenon.

1984ApJS...55..211H

is itself a function of the evolution variables. Recall that this problem was avoided earlier, in the $P\partial_t W$ term, by bringing the factor of E on the right hand side, using $P = E(\Gamma - 1)$, over to the left and integrating the resulting equation (eq. [18]). This is no longer possible since Q (see eq. [19]) is not a simple function of E.

The extreme coupling of Q, W, and V^i and their importance in the determination of the dynamics of this problem make the calculation of extreme special relativistic shocks in a time *explicit* code very difficult. Norman and Winkler (1983) have obtained almost ideal results for extreme shocks using their completely implicit one-dimensional code with an adaptive mesh and including Q at every point in the equations. Evidently, all relativistic terms are of the same magnitude and must *all* be differenced self-consistently to get the correct answer. At this time the calculation of extreme relativistic shocks in a time-explicit formulation remains an unsolved problem. This difficulty need not be of too much concern in our applications as long as the changes in the relativistic gamma W do not become too large across shocks. We must recognize the limitations of our scheme to calculate accurately the specific values of energy and density across a relativistic shock.

To help gauge those limitations we first run tests using the relativistic wall shock problem described in Paper I (eqs. [59]–[60]; see also Fig. 5). The initial conditions for this problem are a stream of cold matter $D\ (=\rho W) = 1.0$ and $E = 10^{-7}$ moving into a wall (reflective boundary conditions) with some velocity V. Changing the fluid velocity allows us to vary the relativistic gamma W and tests the equation's ability to correctly calculate the jump conditions as a function of W.

A numerical example of a relativistic wall shock is shown in Figure 18. The example is for a $W = 2.24$ fluid using a 100 zone grid and the mono scheme including the term $Q/\sqrt{\gamma}\,\partial_i(\sqrt{\gamma}\,WV^i)$ and Q in the inertia. As we shall see, the results obtained for the compression ratio and pressure jump across a shock are sensitive to the choice of Q terms to include. However, certain qualitative features are common to all our wall shock tests, and they are illustrated by Figure 18. Note the spike at the wall in the specific internal energy plot. This is a phenomenon known as "wall heating." Norman and Winkler (1983) have shown that, like the overshoot in the Riemann shock tube, this feature is the actual solution for the finite difference equations as formulated with the wall boundary conditions.

Another prominent feature is the postshock zone-to-zone oscillation, best displayed in the momentum equation. This feature is the "ringing" of the numerical molecules, and it is gradually damped out behind the shock by the explicit viscosity.

Now test the hypothesis that Q must be included in additional terms to formulate correctly the problem relativistically. We begin by running several 100 zone wall shocks using the Newtonian Q formulation. These results are given in Table 3. As can be seen, the error in the compression is relatively large; the error in the $W = 1.01$ (Newtonian) case is comparable to the error in the 100 zone strong shock tube problem (Fig. 16). As W increases, however, so does the error. Is this due to the lack of the relativistic terms in the viscosity equation? We

TABLE 3

RELATIVISTIC WALL SHOCK RESULTS[a]

Γ	W	σ_{analytic}	σ_{code}	Error (%)
5/3 ...	1.01	4.03	4.26	6
4/3 ...	1.01	7.04	7.60	8
5/3 ...	1.35	4.88	5.30	9
4/3 ...	1.35	8.40	9.60	14
5/3 ...	1.80	6.0	6.54	9
4/3 ...	1.80	10.2	12.0	17

[a]For 100 zone runs with the mono scheme using the Newtonian form of the equations for Q, the artificial viscosity. Shown are the results for two equations of state gammas and one Newtonian and two relativistic gammas (W). The term σ is the compression ratio across the shock.

TABLE 4

RELATIVISTIC WALL SHOCK EXPERIMENT[a]

Q Terms	W	σ_{analytic}	σ_{code}	Error (%)
Newtonian $Q\partial_i V^i$	4.12	11.8	12.9	10
Replace with $\frac{Q}{\sqrt{\gamma}}\partial_i(W\sqrt{\gamma}\,V^i)$ ...	4.12	11.8	10.7	−9
Add Q in inertia.....	4.12	11.8	11.5	−3
Add $Q\partial_t W$ without Q in inertia	4.12	11.8	unstable	–
Add Q in inertia.....	4.12	11.8	unstable	–

[a]Using 100 zones and an extreme shock, with equation of state gamma equal to 5/3 and relativistic gamma $W = 4.12$. Various formulations of the energy equation are tried with artificial viscosity Q.

gradually add those additional terms including $Q\partial_t W$, obtained by a single backward time difference.

Table 4 shows the results for a test problem as the various Q terms are successively added. The results show that the $Q\partial_t W$ term as differenced here is unstable. The addition of the other terms helps, particularly the addition of Q in the inertia.

We continue testing with the relativistic form of the Riemann shock tube. The specific problem is described in Paper I (see § IV*b*, Fig. 4) and by Centrella and Wilson (1984); initial conditions are $D = 10$, $E = 20$ to the left of $x = 45$, $D = 1$, $E = 10^{-7}$ to the right. A 500 zone grid was used with $\Delta x = 0.2$ and $\Delta t = 0.1$. The problem was run to time $t = 50$. The analytic and code values are given in Table 5, and the results are plotted in Figure 19. The relativistic gamma W is equal to 1.38 in the preshock region. Note that this is only mildly relativistic.

The code used for Figure 19 included Q in the inertia and $Q\partial_i(\sqrt{\gamma}\,WV^i)$. This is the same form used to obtain Figure 18, the wall shock example. The plot shows that the form of the functions is quite good. The head of the rarefaction wave is at $x = 8$ as predicted analytically; the tail is located at $x = 53$ as

© American Astronomical Society • Provided by the NASA Astrophysics Data System

1984ApJS...55..211H

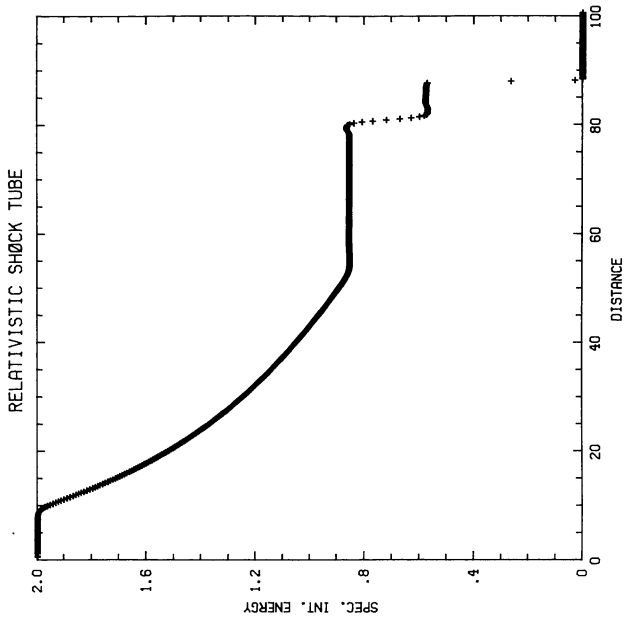


FIG. 19*c*

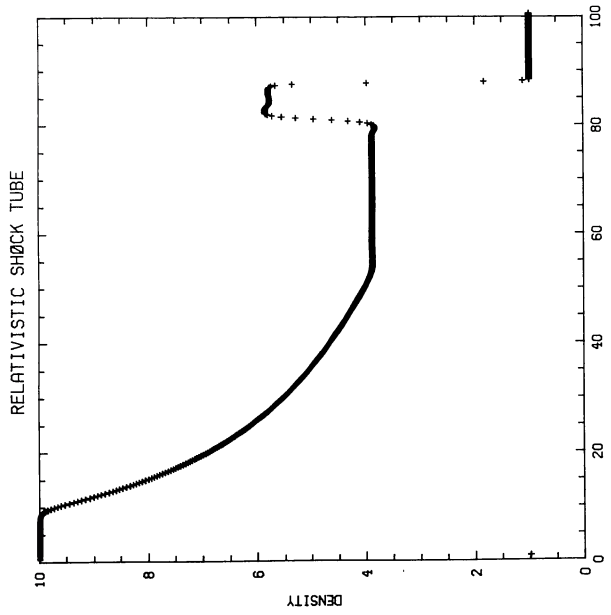


FIG. 19*b*

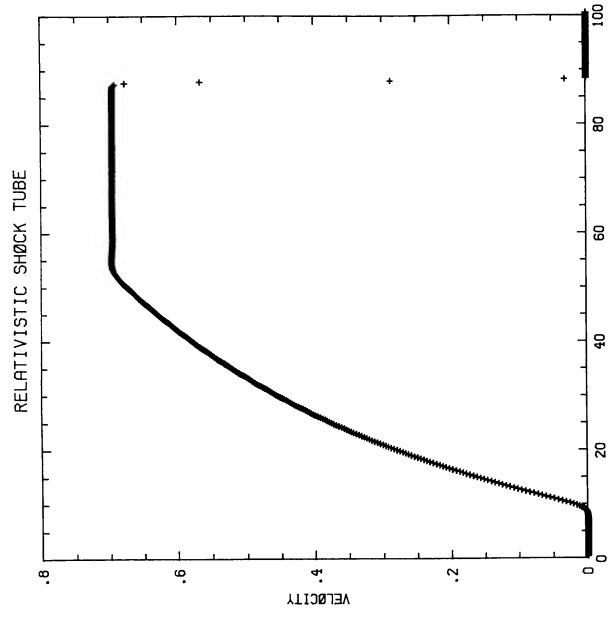


FIG. 19*a*

FIG. 19.—Results of a 500 zone relativistic shock tube ($W = 1.38$) using the mono scheme including the viscosity terms $Q/\sqrt{\gamma}\,\partial_i(\sqrt{\gamma}\,WV^i)$ and Q in the inertia.

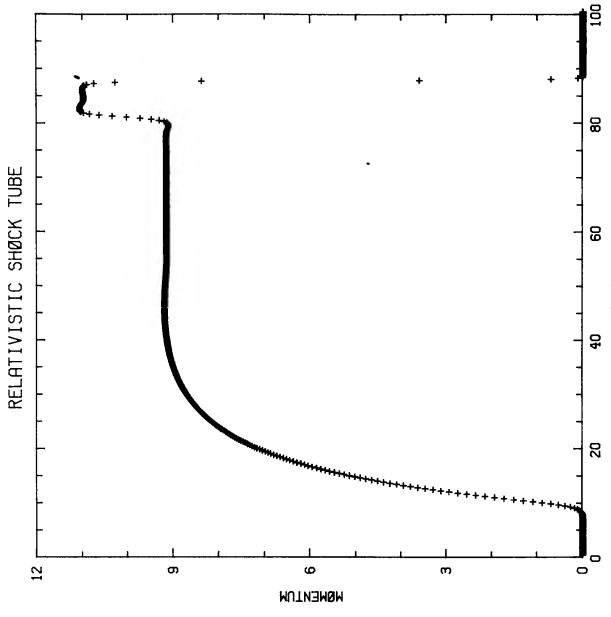


FIG. 19*e*

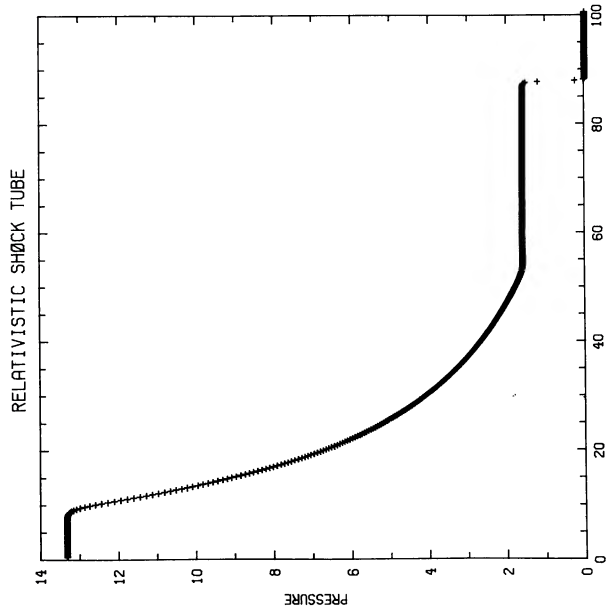


FIG. 19*d*

© American Astronomical Society • Provided by the NASA Astrophysics Data System

1984ApJS...55..211H

TABLE 5

NUMERICAL RESULTS FOR RELATIVE SHOCK TUBE[a]

Scheme	V	D_l	D_r	ε_l	ε_r	P
Analytic	0.690	3.55	6.85	0.806	0.418	1.38
Mono with $Q\partial_i(\sqrt{\gamma}WV^i)$ and Q in inertia	0.696	3.89	5.80	0.854	0.573	1.60
Mono with just $Q\partial_i V^i$	0.708	3.81	6.68	0.834	0.475	1.49

[a] $W = 1.38$; 500 zones.

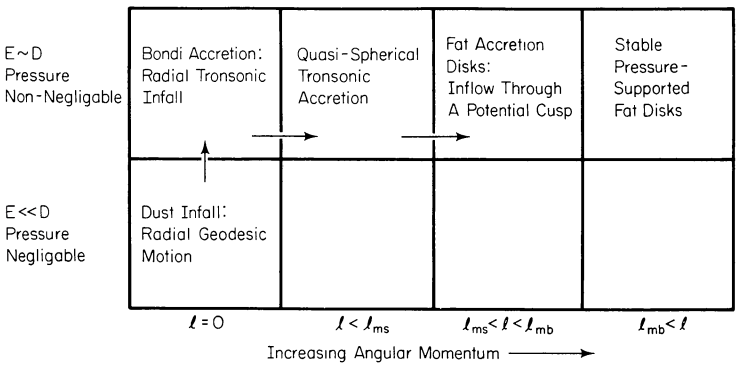


FIG. 20.—Regimes of code tests are shown; as energy and angular momentum become nonnegligible, new dynamics are introduced into the equations and tested.

opposed to $x = 57$. The shock is calculated to be at $x = 87.5$; analytically it is at $x = 86.3$. The largest error is in the values of density (15%) and energy (16%) in the postshock region of the flow.

Perhaps surprisingly, the results using the Newtonian viscosity formulation are better for every variable except the velocity. It would appear that, for mildly relativistic shocks, the errors introduced by the Newtonian formulation are no worse than those introduced by our "semirelativistic" formulation. The Newtonian form has at least a great simplicity and stability in explicit hydrodynamics. At present, implicit schemes seem to be required to obtain high accuracy in highly relativistic shock problems (see the analysis of Norman and Winkler 1983).

c) *Radial Accretion Tests*

We now take our numerical schemes and code and move into the realm of the problem we wish eventually to study: accretion onto black holes. The Kerr metric is reinstated and a spherical coordinate grid is established. For these test problems we keep the grid extremely coarse—this is a good policy in general since a coarse grid will quickly reveal sources of difficulty for less money.

As we proceed through these accretion test runs, we shall attempt to test different sections of the code by gradually adding new dynamical features in the flow. This is done by running a series of tests in which first the pressure is negligible and then significant. The angular momentum of the infalling fluid can be gradually increased as we allow centrifugal accelerations and full two-dimensional flow to become increasingly important. Such a testing sequence is outlined in Figure 20.

i) *Geodesic Infall*

We begin with the first group of accretion tests, the infall of dust. Dust consists of noninteracting test particles moving along geodesics. To model dust we require that the fluid pressure be negligible, i.e., $E/D \ll 1$. The dust is introduced at the outer boundary of the grid and allowed to find a steady-state solution. The strategy in this and all the accretion tests is quite simple. Analytic formulas yield exact values to all code variables; we use the analytic results to compare directly with the steady-state numerical results at each point in the flow. From this we are able to gain insight into how well various portions of the code perform, what effects boundary conditions may have, and, more pragmatically, if any terms in the coding are wrong.

We first consider the Wilson scheme. In this specific test a 25×10 grid is used (25 radial, 10 angular zones). The $j = 2$ zone boundary corresponds to the event horizon, and the $k = 2$ zone boundary is the spin axis of the hole. The zone $j = JM$ is defined as the outer radial boundary and $k = KM$ is the equator (here $JM = 25$ and $KM = 10$.) In the tests described here and below, equal angular zoning was used, with the upper right-hand quadrant divided into $KM - 2$ zones, the $k = 1$ and $k = KM$ zones being reserved for the angular reflection boundary conditions at the axis and equator.

For the dust problem, the outer boundary is set at $r = 18.1M$, and here all code variables are set to their analytic values (see Paper 1, eq. [67]). The variables in the remainder of the grid are set to a negligible value. A variety of inner boundary conditions were tried. In this case we assumed geodesic flow out of the zone next to the horizon (the $j = 2$ zone); inasmuch as this is the analytic flux, this approach worked quite well.

© American Astronomical Society • Provided by the NASA Astrophysics Data System

1984ApJS...55..211H

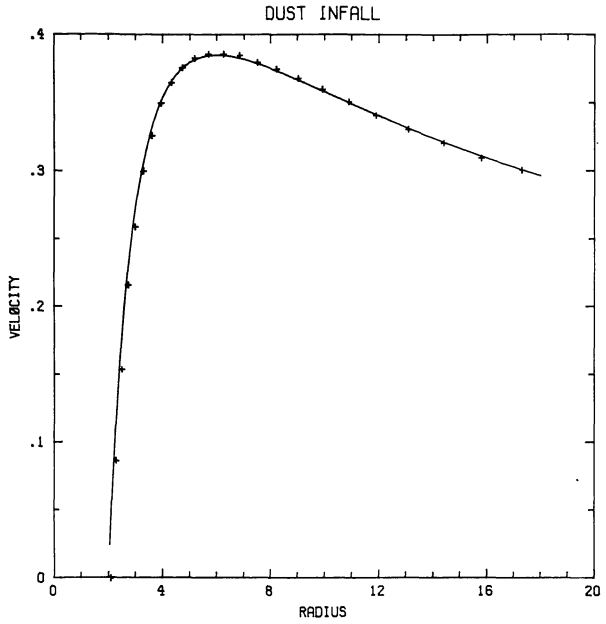


FIG. 21*a*

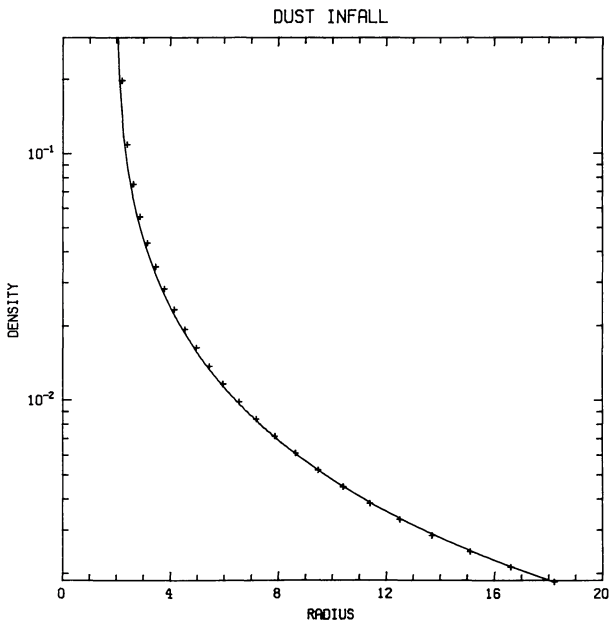


FIG. 21*b*

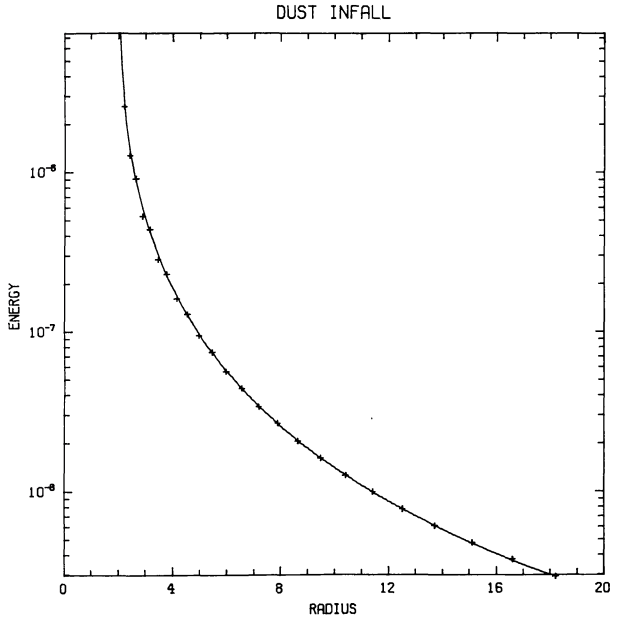


FIG. 21*c*

FIG. 21.—Results for the dust infall test using the Wilson scheme and 25 radial zones.

The evolution is begun as fluid enters the grid from the outer boundary, and falls toward the hole, gradually filling up the space around the hole. The calculation continues until a steady state is reached, in this case by time $t = 90M$, using a time step $\Delta t = 0.187M$ (480 time steps). All variables are then compared to their analytic values.

The results for the Wilson scheme are plotted in Figure 21. We find that V^r never deviates from the analytic free fall value by more than 1%. There is no angular dependence in this or in any other code variable (spherical coordinates—radial flow stays radial). Note that the values of D and E extend over two orders of magnitude in just a few grid zones. The plots of density D shows that the error is never more than 3%, and this occurs only near the horizon. The errors for energy do not increase monotonically as one nears the hole but oscillate between a few percent and as much as 30% or more in the $j = 3$ zone. This is due to the prominent sawtooth oscillation in the values of D and E along the analytic curve, which is again a symptom of the latent instability in the Wilson scheme in the presence of a steep gradient; the inclusion of the weighted upwind scheme prevents the values from growing without bound but does not prevent the development and maintainence of a certain degree of jaggedness in the solution.

This jaggedness goes away when the dust infall test is run with the mono scheme (Fig. 22). In this test the maximum error in V^r is 2%, larger than the Wilson case; in D it is 1%. The error in E is larger (up to 10%); it increases monotonically as r approaches the horizon. In the dust problem the relativistic gamma W goes from $W = 1.06$ at the outer boundary to 1.5 at $r = 3M$; inside of $3M$ W rises steeply. Since no shocks occur in the radial accretion tests, no difficulties can arise from the Q terms.

A Kerr hole ($a \neq 0$) dust infall test was also performed to verify that the coding with the complete Kerr metric terms is correct. Although dragging of inertial frames requires that $U^\Phi \neq 0$, the specific angular momentum of the dust is still conserved and remains a dynamically negligible value. Consequently, there are no new dynamic effects in the Kerr dust run.

ii) *Bondi Accretion*

The next step in testing is to add a new dynamic element by allowing the ratio E/D to be nonnegligible, thus making the pressure force a significant factor in determining the radial

© American Astronomical Society • Provided by the NASA Astrophysics Data System

1984ApJS...55..211H

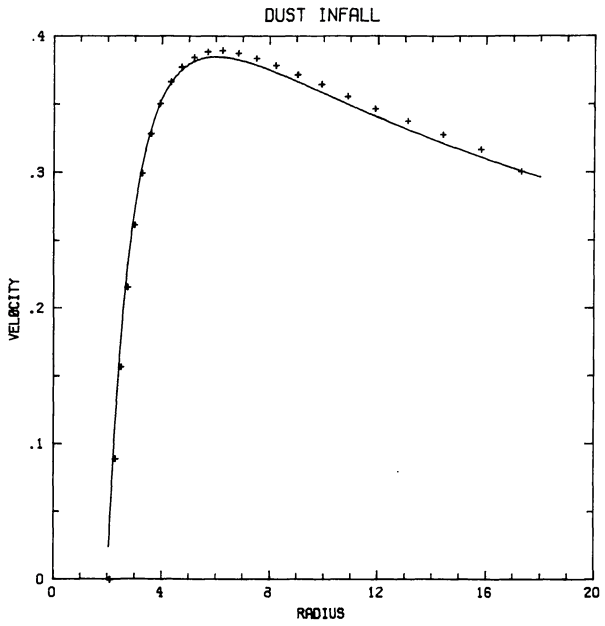


FIG. 22*a*

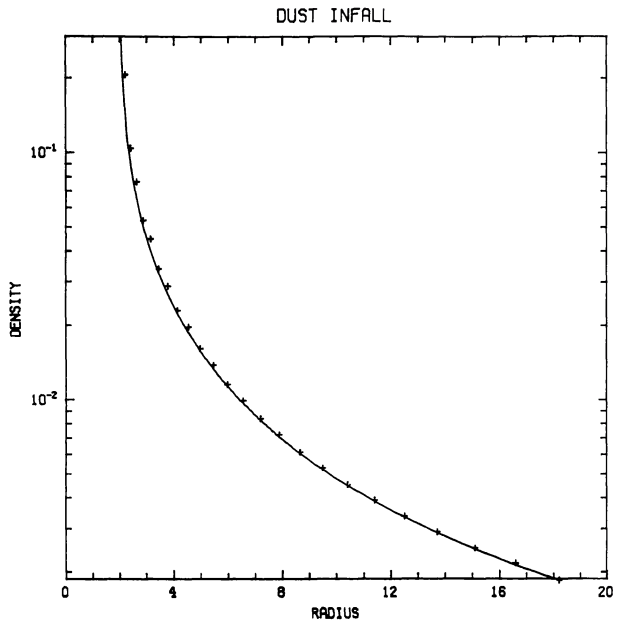


FIG. 22*b*

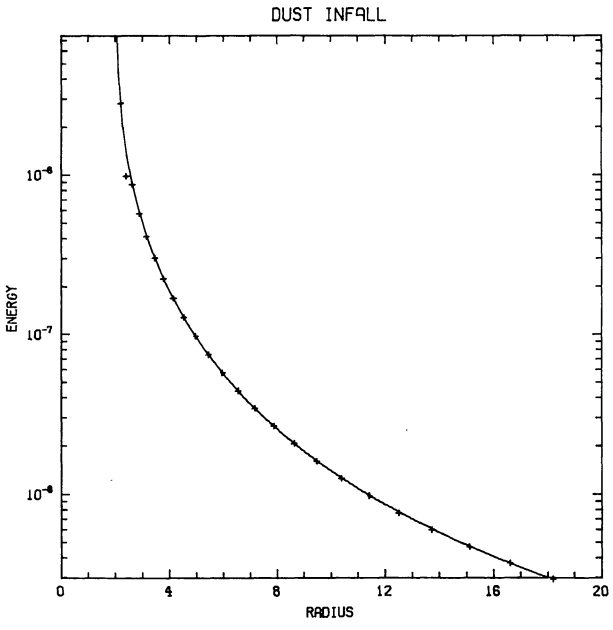


FIG. 22*c*

FIG. 22.—Results for the dust infall test using the mono scheme and 25 radial zones.

flow. The test problem is the general relativistic Bondi accretion of fluid with nonzero pressure (see Paper 1, eqs. [68]–[80]). This problem again tests only radial differencing, but now it involves all the hydrodynamic elements of the radial equations.

This test proceeded in exactly the same manner as the dust test. We begin by describing the results using the Wilson scheme. The same 25×10 grid is again used, with the dust values at the outer boundary replaced with the appropriate analytic Bondi accretion values as determined by the choice of critical point and equation of state gamma. A variety of test problems was run with $\Gamma = 4/3$ and $5/3$ and the critical radius set at $r_c = 6M$ or $8M$. We will discuss the results of a run with $r_c = 8M$ and $\Gamma = 5/3$. Figure 23 depicts the Wilson results for this run at a time $t = 360M$ when steady-state flow has been achieved.

As before, the results for the velocity are excellent, with the largest error less than 2%. Oscillations in D and E are again noted; they have, if anything, become more severe as the pressure begins to enter dynamically. The error in a given oscillation can be rather large: 10% for density and up to 23% for energy.

A demonstrative run was made using the upwind scheme. The results are plotted in Figure 24. The errors are relatively substantial in this run. At its peak, the velocity is overvalued by $\sim 10\%$. Near the horizon ($j = 3$), the density is overvalued by nearly a factor of 2, while the energy is overvalued by a large amount (3 times at $j = 4$ and 18 times at $j = 3$). The upwind scheme is clearly not calculating the proper conserved energy hU_t for the infalling fluid, particularly near the horizon where the functions are very steep.

The results for the mono run are depicted in Figure 25. The largest error in velocity is 2% at the peak of the function. Density has a maximum error of 3% in the zone next to the horizon. This is also where the energy error reaches a maximum of 16%; at $j = 4$ the energy error is 6% and at $j = 5$, 3%, dropping off to less than a percent by $j = 12$, $r = 5.4M$. There is no sign of zone-to-zone oscillation in any of the functions.

Much of the error appears to come from the outer boundary condition. Higher resolution runs with finer grids had comparable errors associated with small errors introduced by the way the fluid is sent onto the grid. Because the mono scheme is basically a three-point scheme, a special definition of the slope function Δ_j (in, e.g., eq. [34]) is required at the outer boundary. The inflow of fluid with the proper energy is more easily assured by removing the outer boundary to a region where the gradients in density, energy, and momentum are not so severe.

© American Astronomical Society • Provided by the NASA Astrophysics Data System

1984ApJS...55..211H

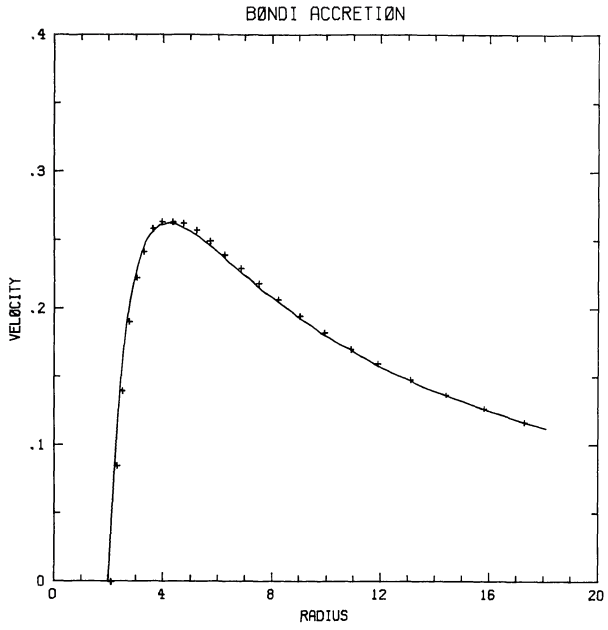


FIG. 23*a*

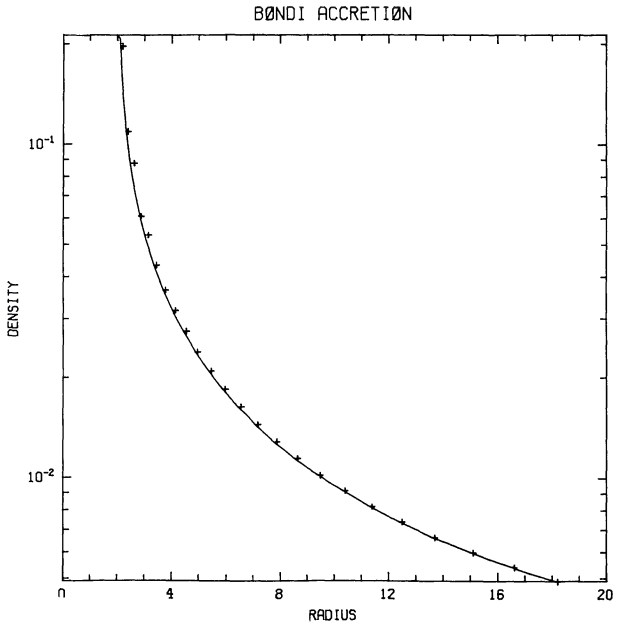


FIG. 23*b*

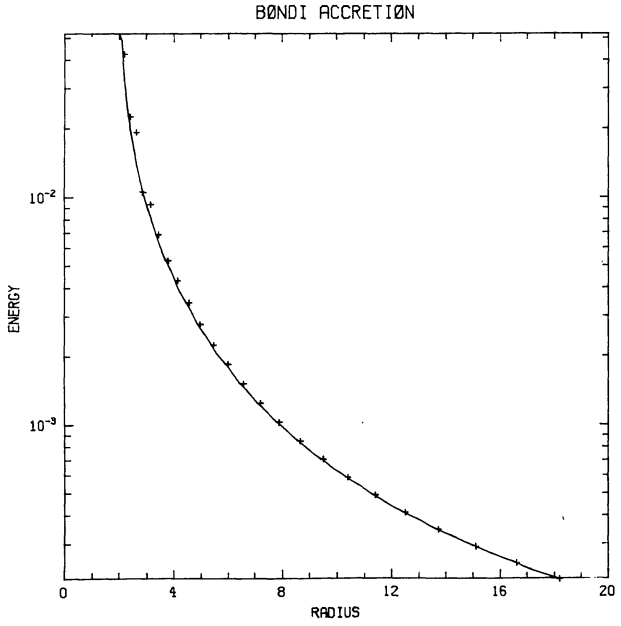


FIG. 23*c*

FIG. 23.—Results for the Bondi accretion test using the Wilson scheme and 25 radial zones.

The radial accretion tests show that the Wilson scheme can yield good results if one is willing to live with and average around the zone-to-zone oscillations which occur. The mono scheme produces better results with no oscillations but requires a bit more care in handling the outer boundary conditions to insure the inflow of material with the desired energy. The upwind scheme is included as an example of a scheme which is stable and which converges to an answer, but not a good answer.

d) Two-dimensional Flow Tests

We now allow the fluid angular momentum as well as the pressure to be nonnegligible, thus insuring new dynamical two-dimensional flows. The angular momentum provides centrifugal accelerations in the θ-direction, while the hot fluid provides a pressure gradient, thus allowing vertical structure above the equatorial plane. Throughout the code development work, our philosophy has been to test the code with known analytic steady-state solutions. In the radial testing, the code was required to evolve a set of initial conditions toward these known steady-state solutions. We were thus able to test the differencing scheme dynamically. This plan is more difficult to apply for two-dimensional flows since there are no simple analytic solutions for U^r and U^θ nonzero. However, there is a steady-state solution to the fluid equations which has a two-dimensional structure, although there is no r or θ velocity. This is the hot, pressure-supported fat disk in which centrifugal pressure and gravitational accelerations are in balance at each point in the disk (see § VI, Paper I).

For test problems we will evolve disk models and fluid flows parameterized by constant angular momentum $l = -U_\phi/U_t$. There are three critical regimes of l: $l < l_{\rm ms}$, less than that of the marginally stable orbit around the black hole; $l > l_{\rm mb}$, greater than the angular momentum of the marginally bound orbit, i.e., the minimum angular momentum which will still turn a particle falling from rest at infinity; and an intermediate angular momentum $l_{\rm ms} < l < l_{\rm mb}$. For more details on how an analytic disk is constructed and the relevant equations for disk structure, the reader is referred to Paper 1, equations (85)–(95), and cited references.

Some of the fat disks—those with high angular momentum $l > l_{\rm mb}$—will be steady state; the code should evolve such models onto themselves. Any observed changes will provide an estimate of the numerical diffusion inherent in the code. In other cases where dynamic evolution is required, U^r and U^θ

© American Astronomical Society • Provided by the NASA Astrophysics Data System

1984ApJS...55..211H

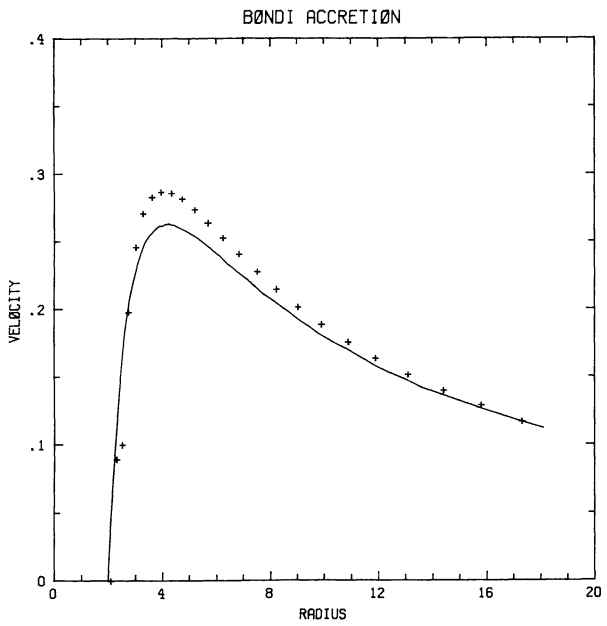


FIG. 24*a*

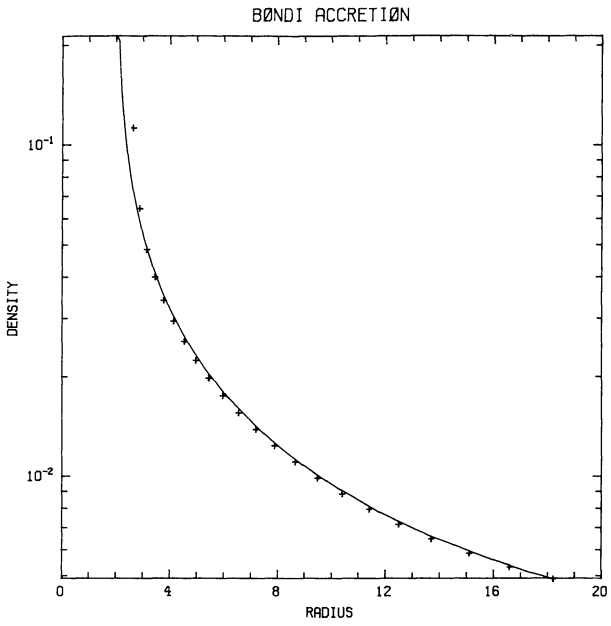


FIG. 24*b*

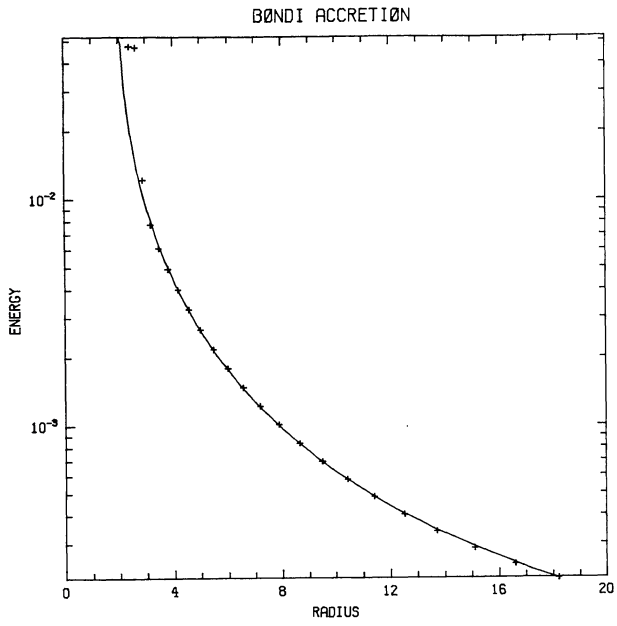


FIG. 24*c*

FIG. 24.—Results for the Bondi accretion test using the first-order upwind scheme and 25 radial zones.

may be on the same order as U^{Φ}. While the evolution from such models is not known in full analytic detail, certain flow patterns and features are expected. Observing the code evolution for such models provides an excellent check on the two-dimensional hydrodynamics. In addition, these cases have aspects of interest in their own right. For models with $l < l_{ms}$ there will be no turning points in the orbits of the fluid. Any fluid with such an angular momentum will spiral into the hole. We can also evolve models in which fluid with angular momentum $l_{ms} < l < l_{mb}$ is allowed to flow onto the grid. Given this l, one can use the analytic model to predict turning points in the fluid orbits and the location of the stable circular orbit where a pressure and density maximum should form. We cannot expect to reproduce an analytic model exactly since the analytic case is not physical (for $l < l_{mb}$); it is based upon the idea that the disk will be static with $U^r = U^{\theta} = 0$. These conditions cannot hold for fluid with $l < l_{mb}$ and initial binding energy $hU_t = -1$. In this case the analytic model is only a guideline which can be used to gauge the results from the fully dynamic calculation.

We will discuss three test cases, low-l infall, high-l stability, and intermediate-l disk formation. Each will be run with the fully developed monotonic code. The grid used for all these tests is a coarse 30 radial by 40 angular zone grid, with equal angular zoning and an outer radius of $r = 27.8M$. The entire half plane from $\theta = 0$ to π is evolved; here we do not use equatorial reflection symmetry. The outer boundary for the first two runs will be a zero inflow boundary. The third is run with a boundary condition which matches the fluid flux from zone JM to $JM-1$ with the flux from $JM-1$ to $JM-2$, either inward or outward. In all three cases the equation of state gamma is 4/3 and the adiabatic constant K ($P = K\rho^{\Gamma}$) is 0.01, the artificial viscosity constant is 2.0, and the time step parameter is set to 1.0 (CFL speed is c). A Schwarzschild hole will be used for all three tests.

In our first test we set $l = 3.0$ ($l < l_{ms}$) and fill the potentials around the hole with fluid using equation (95) in Paper 1. The initial conditions are shown in Figure 26. At the outer boundary on the equator the ratio E/D is 0.023; this ratio increases inward. The model is then evolved; since none of the fluid has sufficient angular momentum to remain in orbit about the hole, inward flow begins immediately with initial velocities directed perpendicularly to the equipotential surfaces which coincide with the surfaces of constant density. Thus, the flow proceeds locally down the steepest gradient. By time

© American Astronomical Society • Provided by the NASA Astrophysics Data System

1984ApJS...55..211H

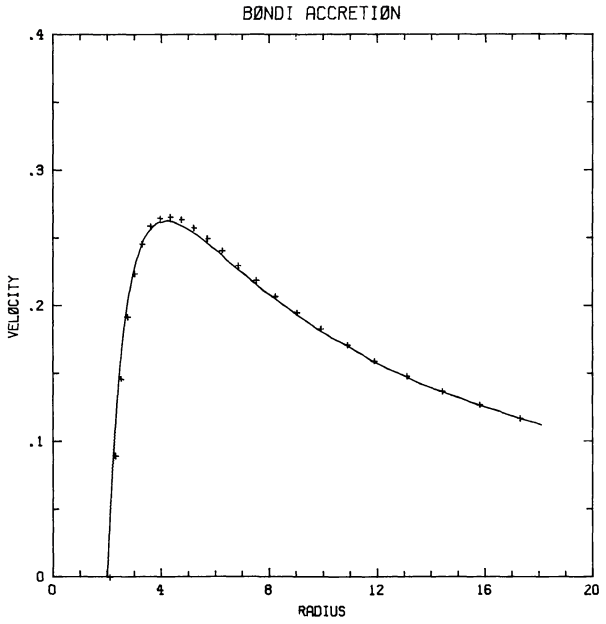


FIG. 25*a*

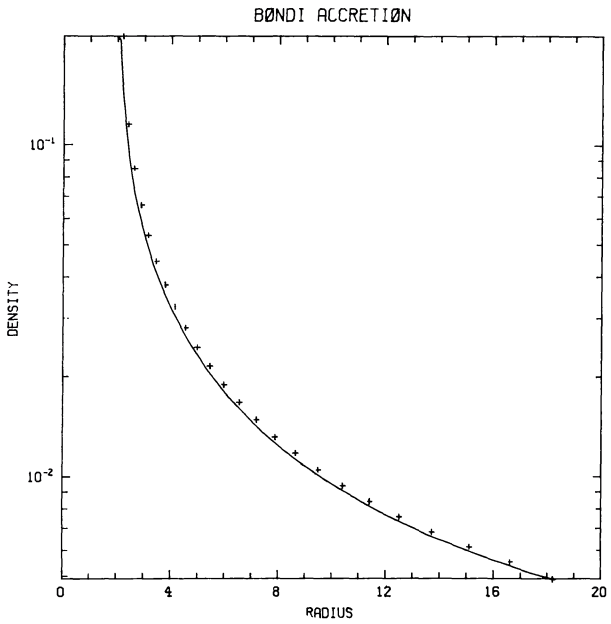


FIG. 25*b*

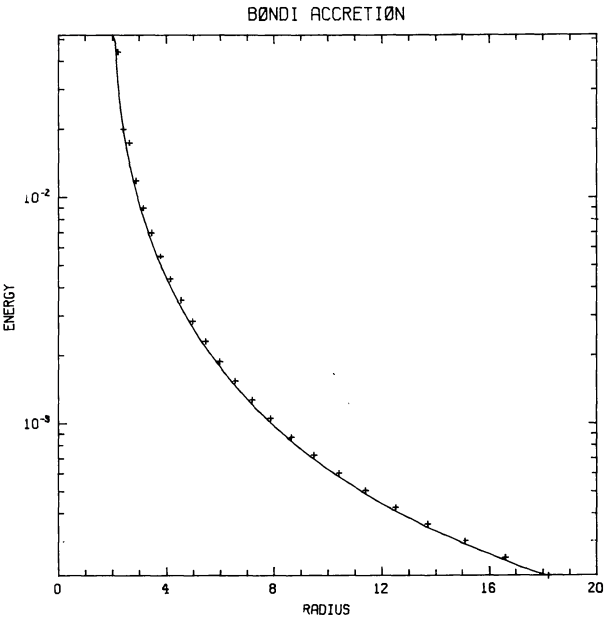


FIG. 25*c*

FIG. 25.—Results for the Bondi accretion test using the mono scheme and 25 radial zones.

$t = 1032M$ much of the fluid has drained into the hole. A typical orbital period, such as at $r = 6M$, is $90M$, so the fluid is clearly spiraling in on a dynamic time scale.

Nothing unusual turns up in this flow; it proceeds exactly as is qualitatively expected. Gravitational acceleration produces an almost laminar flow of fluid toward the hole, and the disk deflates. The height of the disk surface above the equator decreases steadily. The surfaces of constant density, once coincident with the equipotentials, become increasingly elongated radially, and the density drops rapidly in the disk. This flow is of some astrophysical interest since it provides a prototype for a nonspherical Bondi-like accretion flow in cases where angular momentum is not negligible, but is insufficient to prevent accretion and form disks.

Inasmuch as the initial conditions were equatorally symmetric and no physical dynamic stabilities develop which could break that symmetry, this model allows a check of the numerically introduced asymmetry. We find that the azimuthal velocity across the equator is two orders of magnitude less than the (small) value in the neighborhood zones. To three significant figures there is no variation in the values of density, energy, and angular momentum across the equator. Some asymmetry does develop toward the end of the calculation. The final state shows asymmetry of up to 6% in the "vacuum" values of density, energy, and angular momentum (five orders of magnitude below the initial values).

We next consider the case where $l = 4.5 > l_{\rm mb}$. None of the potential surfaces are open onto the hole, and we can construct an analytic pressure-supported disk which should remain stationary. Numerically this requires exact and repeated cancellation of three acceleration terms: gravitational, centrifugal, and pressure gradients. For $l = 4.5$ the pressure maximum occurs at $r = 15.3$ where $E/D = 0.024$. Such a model is set up in the grid and evolved. Figure 27 shows the initial conditions and the disk at time $t = 2150M$. It is evident that the code is able to maintain a steady-state disk on an orbital time scale—the orbital period for the circular orbit at $r = 15.3M$ is $\tau_{\rm orb} = 376M$.

Small oscillations are observed to occur in the disk, but, in general, it remains largely unchanged. The largest variation is a 3% increase in energy at the pressure maximum. No systematic trends were apparent in the small poloidal velocities which developed. Equatorial reflection symmetry was maintained by the evolution throughout the run to at least three significant figures.

© American Astronomical Society • Provided by the NASA Astrophysics Data System

1984ApJS...55..211H

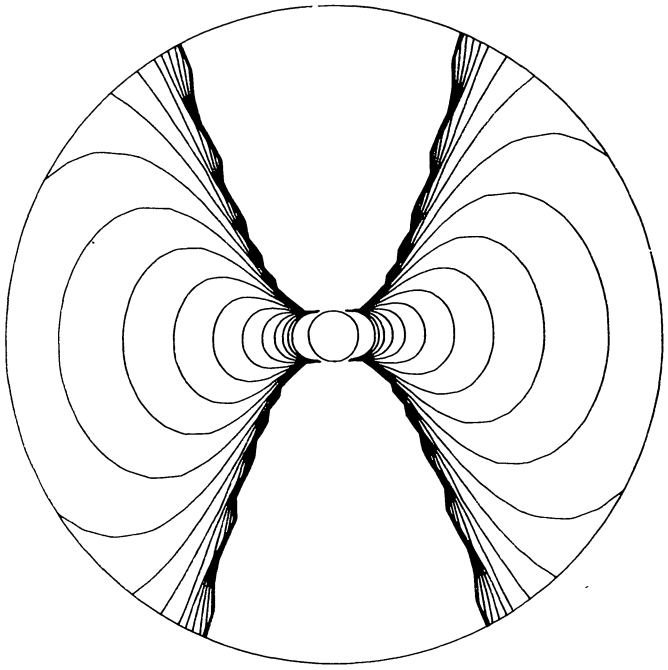


FIG. 26*a*

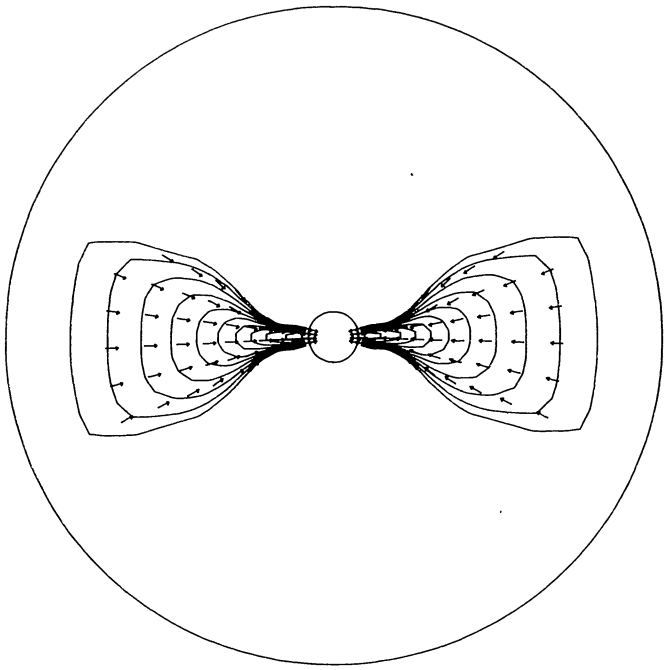


FIG. 26*b*

FIG. 26.—Inflow of low angular momentum fluid is depicted by these plots showing (*a*) initial ($t = 0M$) and (*b*) late ($t = 775M$) times of the $l = 3.0 < l_{ms}$ run. Contours are equally spaced in the logarithm of density from a minimum of 10^{-3} with intervals of log 2. The arrows depict direction of flow velocity but not magnitude and are present at every *other* point wherever the density exceeds one-half the value of the lowest (outermost) contour. We find that infall proceeds on a dynamic time scale. The disk deflates, and the fluid spirals smoothly into the hole.

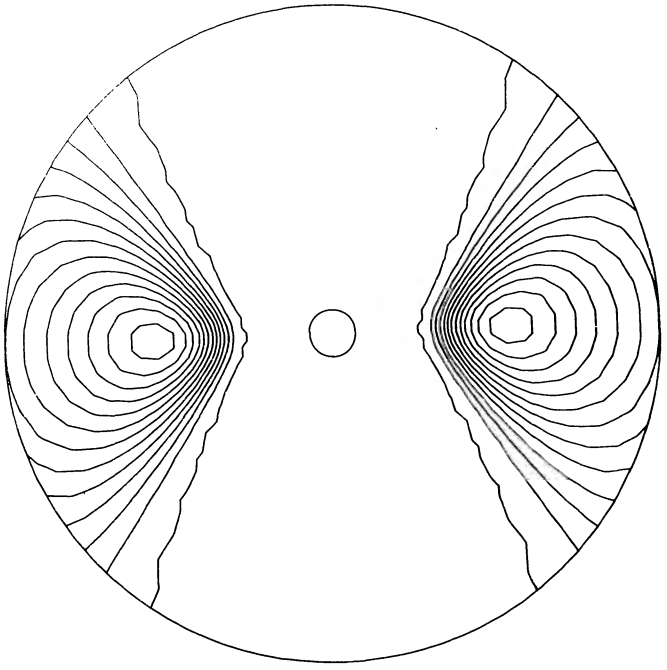


FIG. 27*a*

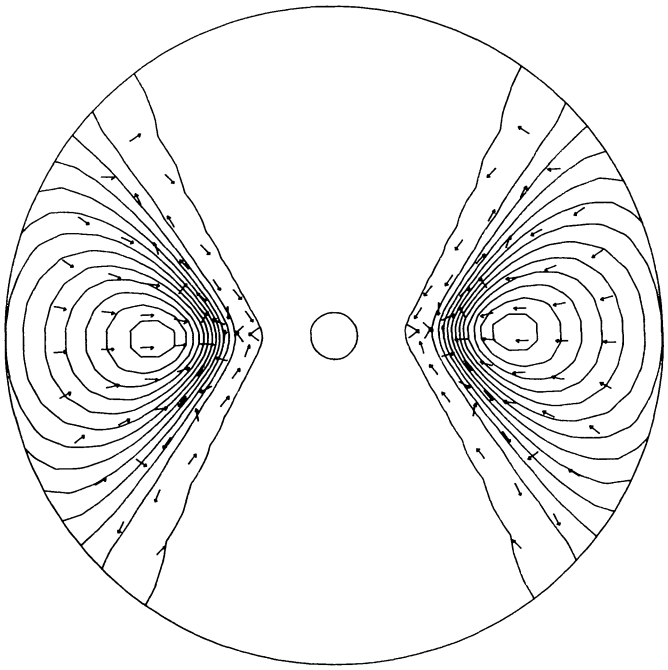


FIG. 27*b*

FIG. 27.—(*a*) Initial and (*b*) late-time ($t = 2150M$) disk models with $l = 4.5 l_{mb}$. Such disks are analytically predicted to remain stationary, and the code is able to reproduce this behavior. The density contours in this plot are linear from 0.001 to 0.48 with an interval of 0.04.

© American Astronomical Society • Provided by the NASA Astrophysics Data System

1984ApJS...55..211H

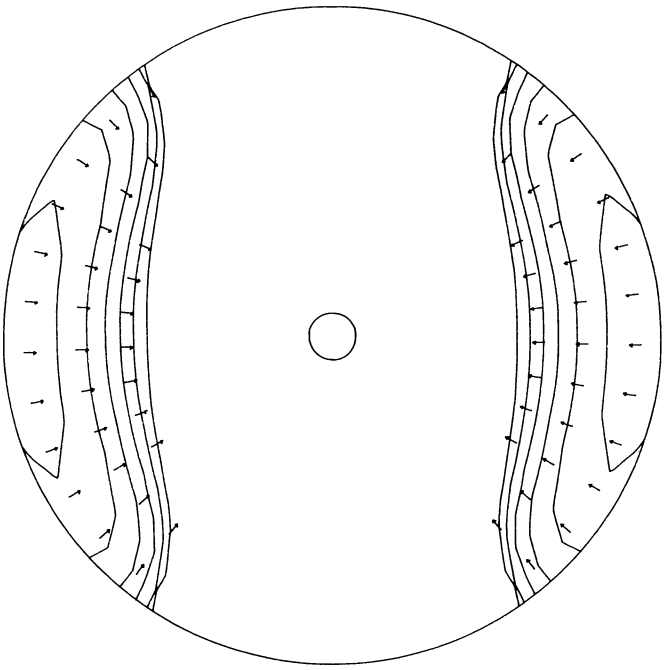


FIG. 28*a*

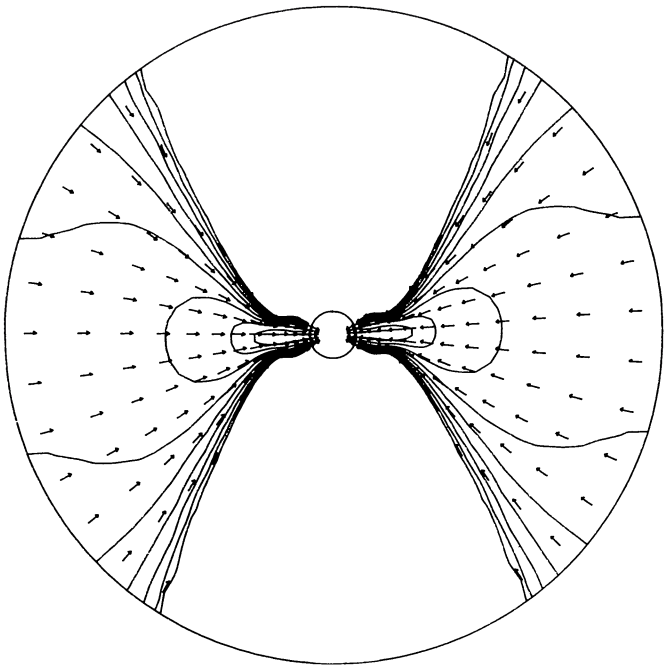


FIG. 28*b*

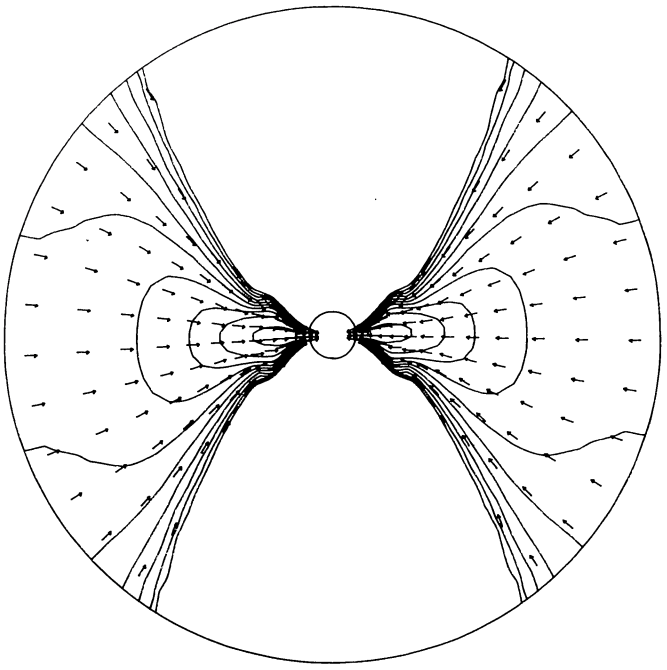


FIG. 28*c*

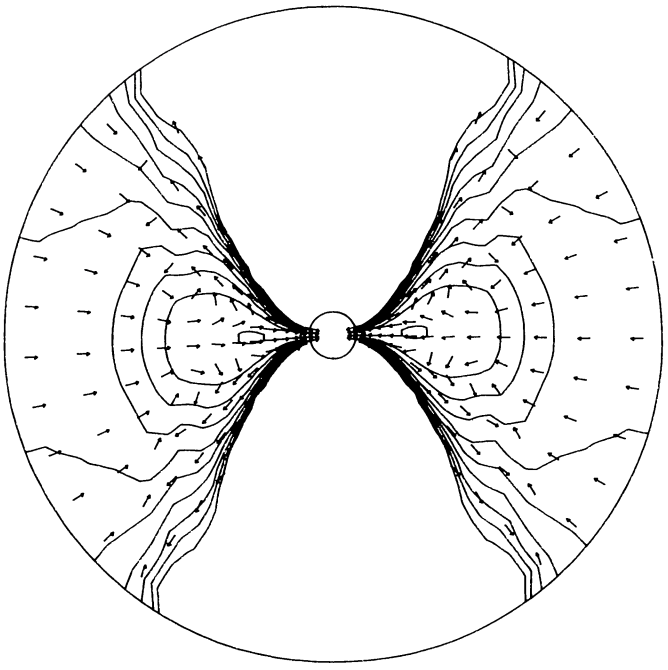


FIG. 28*d*

FIG. 28.—Evolutionary sequence for the infall of fluid with angular momentum $l_{ms} < l = 3.77 < l_{ms}$ at times (*a*) $t = 43M$, (*b*) $t = 130M$, (*c*) $t = 172M$, (*d*) $t = 300M$, (*e*) $t = 430M$. The contours are equally spaced in the log of density, with a minimum of 10^{-6} and an interval of log 2. The vectors depict direction of fluid flow at every other grid point. Note the backflow beginning at $t = 172M$ which results from fluid rebounding at the centrifugal barrier.

© American Astronomical Society • Provided by the NASA Astrophysics Data System

1984ApJS...55..211H

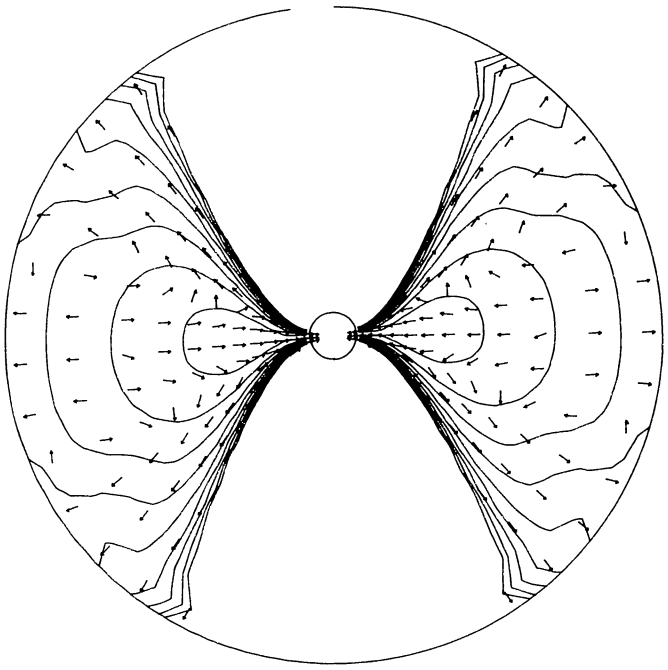


FIG. 28*e*

As a final test problem we set up initial conditions with $l = 3.77$ ($l_{ms} < l < l_{mb}$) fluid in the two outermost radial zones JM and $JM-1$; the initial values in these zones are obtained by essentially cutting away the inner analytic solution for an $l = 3.77$ disk, leaving only the two outer zones. The inflow boundary conditions described above are used, and the initial inflow on the grid begins, driven by pressure and gravitational accelerations. The fluid is expected to fall into the grid and fill up the orbital potential appropriate for a disk with $l = 3.77$. Analytically there is an equatorial orbital turning point at the potential cusp located at $r = 4.72M$ and a pressure and density maximum at the location of the stable circular orbit $r = 8M$ where $E/D = 0.040$.

We display some of the evolutionary sequence in Figure 28. Initially the fluid falls radially onto the grid. By time $t = 130M$ some fluid is down in the near hole region inside the potential cusp. There is sufficient V^θ velocity such that the fluid must be deflected at the equator and redirected toward the hole. By time $t = 172M$ backflow has developed along the surface of the disk accompanied by a shock. Vortices have developed at the leading edge of the backflow. As the evolution continues, it becomes evident that there is a fully developed shock wave moving back through the grid with considerable outflow of fluid along the outer edges of the disk. Inflow continues along the equator. By time $t = 430M$ the shock has gone off the outer boundary, cutting off fluid inflow and ending the evolution.

Comparing the state of the disk at this time with our analytic expectations reveals similarities in overall structure and some differences in details. The pressure maximum does not occur at the same location as in the static disk. In addition, the temperature at the pressure maximum is greater than the static analytic value by 0.8%. Since the specific angular momentum hU_ϕ is conserved (and equal to 3.77), this means that the value of U_ϕ is reduced by the amount that the enthalpy has increased. Since U_ϕ determines the Keplerian orbit and the location of the pressure maximum, we find that as a result of the dynamic heating in the disk the location of the pressure maximum has moved in closer to the hole, from $r = 8.0M$ to $r = 7.6M$. This additional heat is provided in part by the shocks which have occurred and from the fact that the fluid is sent onto the grid with a significant inward velocity. The density along the equatorial slice is compared with analytic values in Figure 29. While the densities observed in the dynamic disk are up to ~ 50% larger than the values predicted for a static disk, the density is similar as is the overall shape of the disk.

In this model, since $l < l_{mb}$, a nozzle remains open onto the hole and fluid is permitted to flow over the potential cusp and into the hole. Thus, this model will remain dynamic; the subsequent evolution of this and similar disks is one of the first uses we have made of the code. We will report results of calculated dynamic disks in our next paper.

IV. CONCLUSIONS

Our accretion tests can now be summarized. As we proceeded through the testing regimes (Fig. 20), we added new physics and new dynamics to the accretion flows through the addition of pressure and angular momentum. This brought into play new sections of the equations of hydrodynamics (eqs. [1]–[3]) for code testing. We began with the geodesic infall of pressureless dust. This tested the transport terms, the velocity renormalization, and the gravitational acceleration in the limit of negligible pressure. As the energy of the infalling fluid is increased, the pressure gradient becomes dynamically

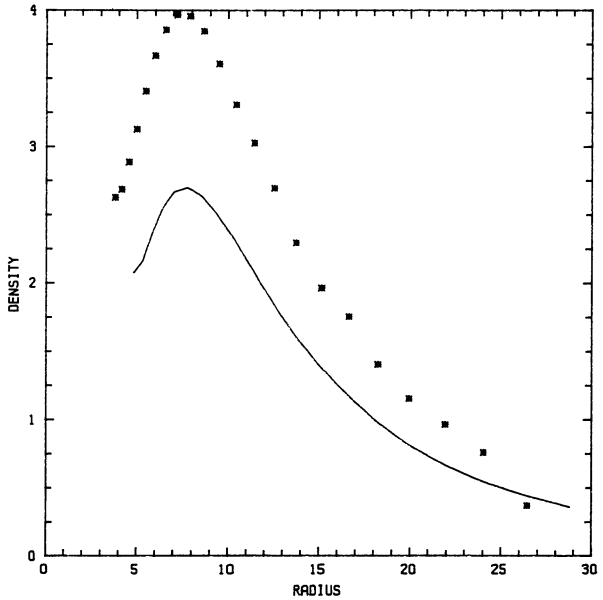


FIG. 29.—Solid curve is the density along the equatorial slice for the *static* $l = 3.77$ disk as predicted analytically. The points are from the dynamic model at $t = 430M$. Good qualitative agreement is obtained despite the fact that in the numerical model V^r and V^θ are nonzero.

© American Astronomical Society • Provided by the NASA Astrophysics Data System

1984ApJS...55..211H

important, and the radial infall velocity drops below the free-fall value. The steady-state radial infall of hot fluid is the transonic Bondi accretion problem. The new term it tests is the pressure gradient acceleration in the momentum equation.

These problems effectively test the one-dimensional hydrodynamic equations, but our goal is to study two-dimensional problems. To test this second dimension, angular momentum is gradually added to the hot fluid, bringing into play the centrifugal acceleration term as well as transport and gradients in the θ-direction. While angular momentum l is small, the flow is not too different from the Bondi case. A smooth accretion flow is established with some amount of poloidal velocity V^{θ}. The nonradial flow is funneled toward the equator and into the hole between the equator and some limiting angle θ_m. As l further increases, this angular opening into the hole narrows. When l reaches the marginally stable value $l_{\rm ms}$, a new phenomenon occurs. Some portion of the fluid encounters a turning point in its orbit, and its inward motion is halted. In a dynamic disk formation such as we used for a test problem, this causes a shock to occur as the infalling fluid "bounces" at the centrifugal barrier. Similar accretion shocks were observed by Wilson (1972) in his study of the infall of cold fluid with nonzero angular momentum. The presence of such shocks emphasizes the need for shock tube problems in the test ensemble.

Our intermediate-l disk can continue to permit matter inflow as it settles down to become a large, subsonic fat disk attached to the hole by a narrow accretion nozzle. Such a model is the most complete test of the hydrodynamic equations since it dynamically involves all the terms. However, as $l \rightarrow l_{\rm mb}$, $\theta_m \rightarrow \pi/2$, and the nozzle shuts off. We are left with a disk in which no further accretion is possible without viscous shear to redistribute the angular momentum. In such a steady-state, pressure-supported disk there need not be any internal motion. Consequently, the high-l model simplifies the hydrodynamic equations to a balance of pressure gradient, centrifugal, and gravitational accelerations.

Thus, the testing procedure has come full circle. In the dust case the pressure gradient and centrifugal accelerations were not important; the radial momentum equation and radial transport determined the dynamics. In the high-l case the opposite is true. Thus, an exploration of the regimes of accretion physics has produced a parallel exploration of the numerical equations and provided a calibration, both separately and jointly, of all their dynamic terms.

In this paper we have described both the numerical techniques we are using and the techniques we have considered to study the equations of general relativistic hydrodynamics for fluid accreting into a Kerr black hole. The purpose has been twofold: (1) to add to the body of literature describing methods and tests of finite differencing of partial differential equations in an astrophysical context, thus assisting other researchers who wish to perform numerical experiments of their own; and (2) to give a detailed description of the methods used and problems encountered in calibrating our particular code. This allows astrophysicists unfamiliar with numerical techniques to gain a better appreciation of the difficulties involved and enables them to make an informed assessment of the results we obtain for astrophysically interesting problems. It is further hoped that this paper and Paper I will serve as a paradigm of the necessary procedure of calibrating the numerical tools to be used in solving partial differential equations numerically in astrophysics.

Partial support for this work was provided by the National Science Foundation through grant PHY80-01496 and by the Department of Energy. The National Center for Atmospheric Research is acknowledged as the source for the graphics software. Computational work was performed on the University of Illinois Cyber 175 and the VAX and Image Processing System, operated jointly by the departments of Astronomy and Atmospheric Science and the Computer Services Office. One of us (J. H.) wishes to thank Martin Rees and Mitch Begelman for enlightening discussions and the Institute of Astronomy, Cambridge, UK, for its hospitality. Finally, we thank Joan Centrella, Mike Norman, and K.-H. Winkler for many illuminating discussions on code differencing and testing.

REFERENCES

Barton, R. 1981, private communication.
Centrella, J., and Wilson, J. R. 1984, *Ap. J. Suppl.*, **54**, 229.
Courant, R., Friedrichs, K., and Lewy, H. 1967, *IBM Journal*, **11**, 215.
Hawley, J. F., Smarr, L. L., and Wilson, J. R. 1984, *Ap. J.*, **277**, 296.
May, M. M., and White, R. H. 1967, in *Methods of Computational Physics*, Vol. **7**, ed. B. Adler, S. Fernbach, and M. Rolenberg (New York: Academic), p. 219.
Norman, M. L. 1982, private communication.
Norman, M. L., Wilson, J. R., and Barton, R. T. 1980, *Ap. J.*, **239**, 968.
Norman, M. L., and Winkler, K.-H. 1983, in *Radiation Hydrodynamics*, ed. M. Norman and K.-H. Winkler (Dordrecht: Reidel), in press.
Richtmyer, R. D., and Morton, K. W. 1967, *Difference Methods for Initial Value Problems* (New York: Wiley).
Roache, P. J. 1972, *Computational Fluid Dynamics* (Albuquerque: Hermosa).
Smarr, L. L. 1978, in *Sources of Gravitational Radiation*, ed. L. Smarr (Cambridge: Cambridge University Press), p. 139.
Sod, G. A. 1978, *J. Comput. Phys.*, **27**, 1.
Strang, G. 1968, *Siam J. Num. Analysis*, **5**, 506.
van Leer, B. 1974, *J. Comput. Phys.*, **14**, 361.
_____. 1977*a*, *J. Comput. Phys.*, **23**, 263.
_____. 1977*b*, *J. Comput. Phys.*, **23**, 276.
_____. 1979, *J. Comput. Phys.*, **32**, 101.
Wilson, J. R. 1972, *Ap. J.*, **173**, 431.
_____. 1978, in *Sources of Gravitational Radiation*, ed. L. Smarr (Cambridge: Cambridge University Press), p. 423.
Winkler, K.-H. 1981, private communication.
Woodward, P. R. 1983, in *Radiation Hydrodynamics*, ed. M. Norman and K.-H. Winkler (Dordrecht: Reidel), in press.
Woodward, P. R., and Colella, P. 1981, in *Lecture Notes in Physics*, Vol. **141**, *Proc. 7th Internat. Conf. on Numerical Fluid Dynamics*, ed. W. C. Reynolds and R. W. MacCormack (New York: Springer-Verlag), p. 434.
_____. 1982*a*, *J. Comput. Phys.*, submitted.
_____. 1982*b*, preprint LBL-14661.

JOHN F. HAWLEY and LARRY L. SMARR: Department of Astronomy, University of Illinois, 341 Astronomy Building, 1011 W. Springfield, Urbana, IL 61801

JAMES R. WILSON: L-35, Lawrence Livermore National Laboratory, P.O. Box 808, Livermore, CA 94550

© American Astronomical Society • Provided by the NASA Astrophysics Data System